A Precision-Controlled Investigation Into The Fundamentals Which Drive The Incredible Superhydrophobic Properties Of Soot

A thesis submitted as a partial fulfilment of the Virginia Commonwealth University requirements for a Masters of Science at Virginia Commonwealth University.

By
Ashton Bressler
Bachelor's of Science from VCU

Director: Dr. Reza Mohammadi
Associate Professor, Department of Mechanical and Nuclear Engineering

Virginia Commonwealth University Richmond, Virginia
March, 2024

Acknowledgment:

I would first and foremost like to thank my advisor Reza Mohammadi. He has always fought for me and been thoughtful in all of our conversations. I also want to extend my thanks to those who have worked with me in the lab; I was lucky to have a group so willing to help and lend time when it mattered. My employer, BGB Technology, gave me ample flexibility and support through my endeavors. Most importantly I need to thank my family and friends, especially Chuck Zalesiak, who put in many hours reviewing my work. His support and that from the rest of my love ones made it possible for me to push for new and greater things.

Table of Contents

List of Tables

List of Figures

Abstract

A PRECISION-CONTROLLED INVESTIGATION INTO THE FUNDAMENTALS WHICH DRIVE THE INCREDIBLE SUPERHYDROPHOBIC PROPERTIES OF SOOT

By Ashton Bressler

A thesis submitted as a partial fulfilment of the Virginia Commonwealth University requirements for a Masters of Science at Virginia Commonwealth University.

Virginia Commonwealth University, 2024.

This thesis investigates a precision controlled superhydrophobic soot surface, composed of semi-rigid linked chains of spheres, with a radii of roughly 14um. These spheres have exceptionally useful hydrophobic properties due to; their large surface area, their large triple phase line length, their low area fraction of solid-liquid interface, their ability to deform, and their strength from both the DLC bond formed in combustion and the ability of the cross linked lattice to support itself under pressure.

A custom system was built to precisely control the flow rate of rapeseed oil through a cutting torch and into a combustion chamber being fed varied amounts of oxygen to support the combustion process. The Methodology section covers the iterations which led to the design of the combustion process. Samples were then analyzed under a SEM and their advancing and receding contact angle measurements were recorded.

This thesis provides an in-depth understanding of surface energy balance and its role in wetting. The major topical areas covered in this thesis as listed below:

* The significance of roughness
* The advantages of the Cassie-Baxter state to anti wetting
* Complications around creating a surface which can stay in this Cassie-Baxter state
* Problems with the fragility of superhydrophobic surfaces
* Hydrophobic properties, as they relate to triple-phase line energies.

VITA

Ashton Bressler was born January 24,1993 in Richmond Va. He graduated James River Highschool in 2011, immediately attended Virginia Commonwealth University (VCU) and graduated with a Bachelor of Science degree in mechanical engineering and minors in mathematics and physics. He then joined the laboratory of Dr. Reza Mohammadi to begin his graduate studies, working as a teaching assistant, helping many other graduate students and faculty conduct experiments. His work in the laboratory has resulted in seven (7) co-authorships on the topic of hydrophobics. During this time he was hired by BGB Technology to head research and development of a number of products as well as to serve as a materials expert to the company.

Chapter 1 Introduction

Our lab has worked with superhydrophobic soot since its establishment, with its first publication on soot in 2016. It started with the simple modification of using a chimney to reduce the air flow and control the direction. This led to surfaces that were surprisingly robust. They were capable of taking droplet impact, streams of water and jets of air while retaining their superhydrophobic properties. It quickly became apparent that these surfaces were exceptional and warranted further investigation.

From studying these surfaces came the realization that they could form chains of spheres which had cross linked structures, allowing them to be supported in multiple directions. Additionally it was found they formed both Sp2 and Sp3 bonds. Sp3 bonds being diamond like carbon (DLC) which is exceptionally strong but still bonds poorly to water.

However it was still apparent the surfaces were not fully understood. The current system being used suffered from a lack of reproducibility. It had a number of uncontrolled variables, and the samples, under many forms of analysis, were not homogenous. Our lab needed a more scientific system which could precisely control the combustion conditions such that an in depth analysis of the surface could be conducted.

This thesis will discuss the fundamentals and theories for developing an exceptionally useful superhydrophobic surface, as illustrated by scanning electron microscope (SEM) and contact angle analyses of a carbon soot surface which is precision-tuned by manipulating the combustion process. This allows us to gain unique insight into the reasons for the soot surfaces remarkable performance.

The term, “superhydrophobics”, has seen a continuous, almost linear 67-fold increase in usage from 2002 to 2019. {google ngram viewer}

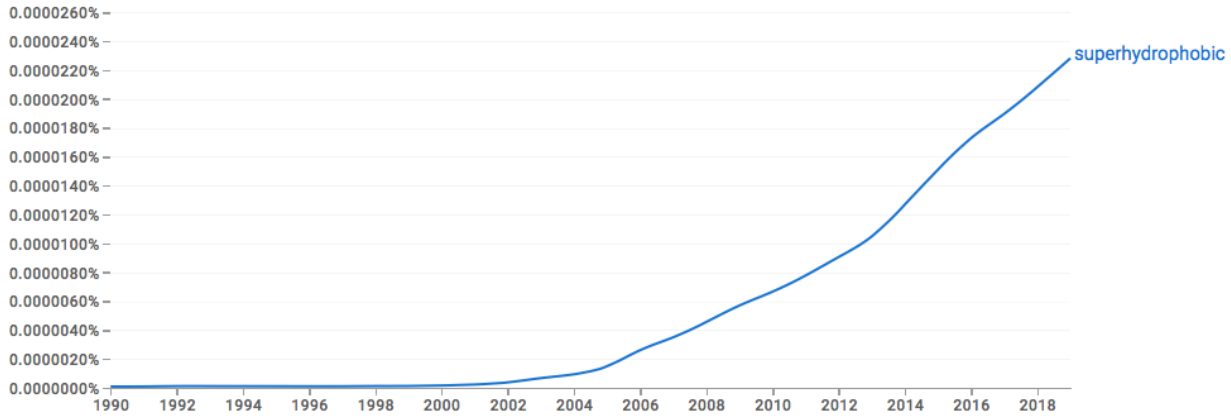

Figure 1.1 google ngram data for superhydrophobics

Typically, superhydrophobic surfaces are characterized by contact angles greater than 150 degrees [1] [2], a low roll off angle [1] [2], self-cleaning properties [2], anti-corrosion [3], fouling resistance [4], anti-icing [5] [6], reduced cell growth [7], and reduced drag [8], [9]. These characteristics have made superhydrophobic surfaces interesting to many fields including medical, micro fluids, aerospace, aquatics, textiles, and manufacturing.

Superhydrophobic materials are fragile and often difficult or costly to manufacture. Manufacturing methods include templating, electrospinning, hydrothermal synthesis, sol-gel, layer-by-layer, chemical vapor deposition, plasma etching, sputtering and using an adhesive to bind particles together [10], [11] [4], [9], [12]–[15].
In previous works our lab has proven that a carbon soot surface under the correct conditions can produce exceptionally robust superhydrophobic surfaces efficiently and cheaply [16], [17].

1.1 Important definitions: Contact angle, wetting, surface interfaces and hysteresis

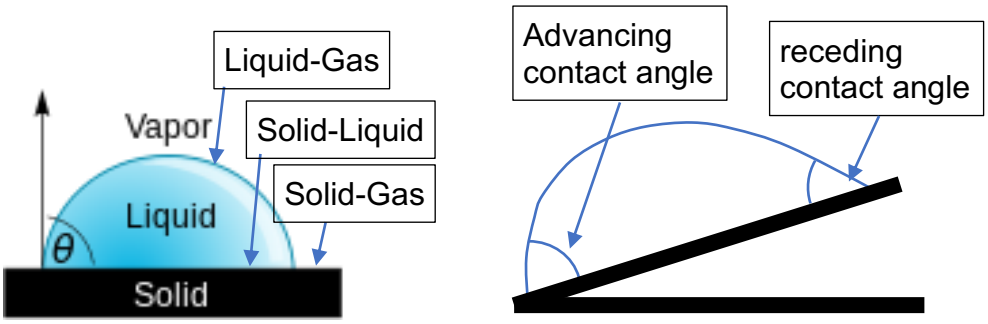

Figure 1.2: a) Droplet contact angle and interfaces *b) advancing and receding contact angle on tilted surface.*

It is common in many fields of science to talk about how surfaces are wetted by a liquid. In the case of hydrophobics our objective is to try and keep the surface dry (i.e., make the surface wet very poorly). There are two (2) major methods to quantify this objective: The first method uses the contact angle to quantify surface wetness. When a small amount of a liquid comes into contact with a solid, the liquid generally forms a droplet on the surface. There are three (3) boundaries to consider as shown in Figure 1.2a; the Solid-Gas, Solid-Liquid and Liquid-Gas interfaces. These surface interfaces will be mentioned throughout this thesis; hence, it is important for the reader to have the correct mental picture each surface interface. The contact angle is the angle created by the surface and the tangent line of the edge of the bubble where it meets the surface. If the liquid forms a hemispheric shape, the contact angle is said to be 90 degrees. If the shape forms more of a sphere, the contact angle increases. A perfect sphere on a surface would have a contact angle of 180 degrees.

The second quantification method involves the important aspect of wetting is hysteresis, which is the difference between the advancing and receding contact angle of a droplet on a surface. The advancing angle is the one which would be measured if a droplet where on a tilted surface and was trying to roll down it. The receding angle is the angle of the trailing edge of the tilted droplet. (See Figure 1.2b) For hydrophobics it is common to measure these angles by injecting and retracting fluid into a droplet and measuring the angle as it advances and recedes on the surface.

1.2 Surface energy:

Superhydrophobic surface wetting is primarily a thermodynamic process driven by the surface energies of Solid-Gas, Solid-Liquid and Liquid-Gas interfaces [18].

The difference in surface energy and the natural drive for a system to reach its lowest energy state is critical to thinking about surface wetting. The following discussion provides a brief explanation to help the reader understand how these terms relate.

Surface energy is a type of potential energy, which is often measured in units of Joules per meter squared (J/m^2). In general, the bulk of a material is at a lower energy than its surface. The energy between adjacent molecules is less than the energy of the exposed molecules. The reason that a liquid forms a sphere in space is because a sphere has the least surface area for a given volume of liquid; hence, exists at the lowest energy state.

In the thought experiment for a solid, consider a 1-inch cube inside a vacuum chamber. This is so it can be cut in half reversibly. (i.e., the 2 halves suffer no deformation from the cutting and would bond back into a 1-in cube with no seam). If making the cut takes 2 mJ of energy and creates two (2) new 1-in square surfaces on each half. Then the material has a surface energy of 1 mJ per square inch. This is not a perfect thought experiment, but it helps to give some idea about how stronger bonded solids would tend to have a higher surface energy. An important concept for wetting is understanding that the free surface has extra energy compared to the bulk,

1.3 Fundamentals of Superhydrophobic surfaces:

There are a few things to consider when thinking about surface wetting. First a system will change until it is balanced and it wants to be at the lowest energy state.

In the spreading case placing water onto a surface results in a Solid-Liquid interface energy, which is lower than the Solid-Gas interface energy. This spreading indicates a release of energy due to the difference in the two (2) interface energies. This released energy is generally in the form of increased thermal energy (heat) to the system and its surroundings. Joules are being released into the system based on the difference of the interface energies and the area which is being wetted. This is part of the system trying to reach its lowest energy state.

Next, the system needs to be balanced. When the spreading gets to the point where the droplet is becoming flatter than a hemisphere (i.e., contact angle less than 90 degrees), spreading can only continue if the liquid-gas interface area increases. For the liquid-gas interface area to increase the droplet must be stretched out. It is easy to understand how stretching out a liquid requires energy [18]. It is the potential energy from the difference in free surface energies which overcomes the intermolecular forces of the droplet and stretches it out.

To think about this iteratively, consider a droplet on a surface. Ask, will the spreading of the droplet lower the energy of the system. In this case, the Solid surface wants a liquid in contact with it to lower its surface energy, and therefore the energy of the system as a whole. The total decrease in system energy is based on how much lower the Solid-Liquid surface energy is than the Solid-Gas surface energy, and how much area is covered as it spreads. However the stretching of the droplet raises the energy of the system by the Liquid-Gas surface energy, multiplied by the increase in Liquid-Gas surface area as it spreads. The spreading will stop when these are balanced, and the whole system will be at a lower energy, which was released thermodynamically. It is the balance of energies which determine the contact angle. This concept is explained in detail below.

1.4 Geometric understanding of area:

Note: All of the following plots and examples are in reference to a droplet of water with a unit volume.

First, while the contact angle of a droplet is close to 90 degrees, the spreading or contracting of the droplet results in very little change to the Liquid-Gas surface area. Second, the Liquid-Gas surface area is minimal for a droplet of hemispheric shape. This can be seen plotted below in Figure 1.4. The surface area is calculated using the following equation for a spherical cap. Where the surface area of the cap is the external area on the sphere which has a height "h" with respect to its circular radius "a", this is shown as the translucent area seen in Figure 1.3.

$$SurfaceArea = \pi(a^2 + h^2)$$

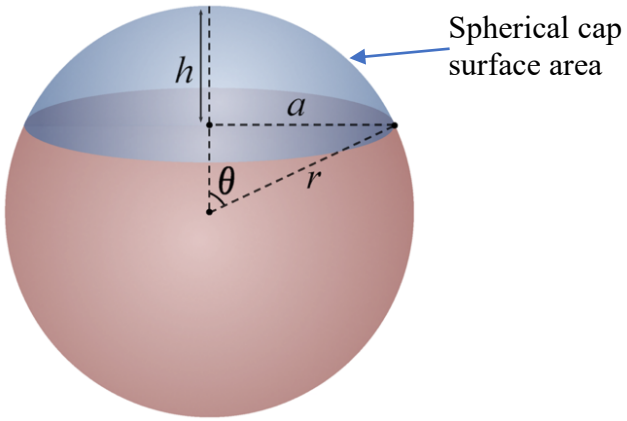

Figure 1.3:Diagram of Spherical Cap

For a constant unit volume the surface area changes with respect to the contact angle. This is plotted in Figure 1.4 below, which shows that the Liquid/Gas surface area of a spherical cap is clearly lowest at 90 degrees with a unit Liquid-Gas surface area of about 3.84. Also, the slope of the curve for the plot of the Liquid-Gas surface area at 90 degrees is almost zero, with the area remaining very close to 3.84 from 85 degrees to

95 degrees. Hence, a small change in contact angle, when close to 90 degrees, corresponds to almost no change in the Liquid-Gas surface area.

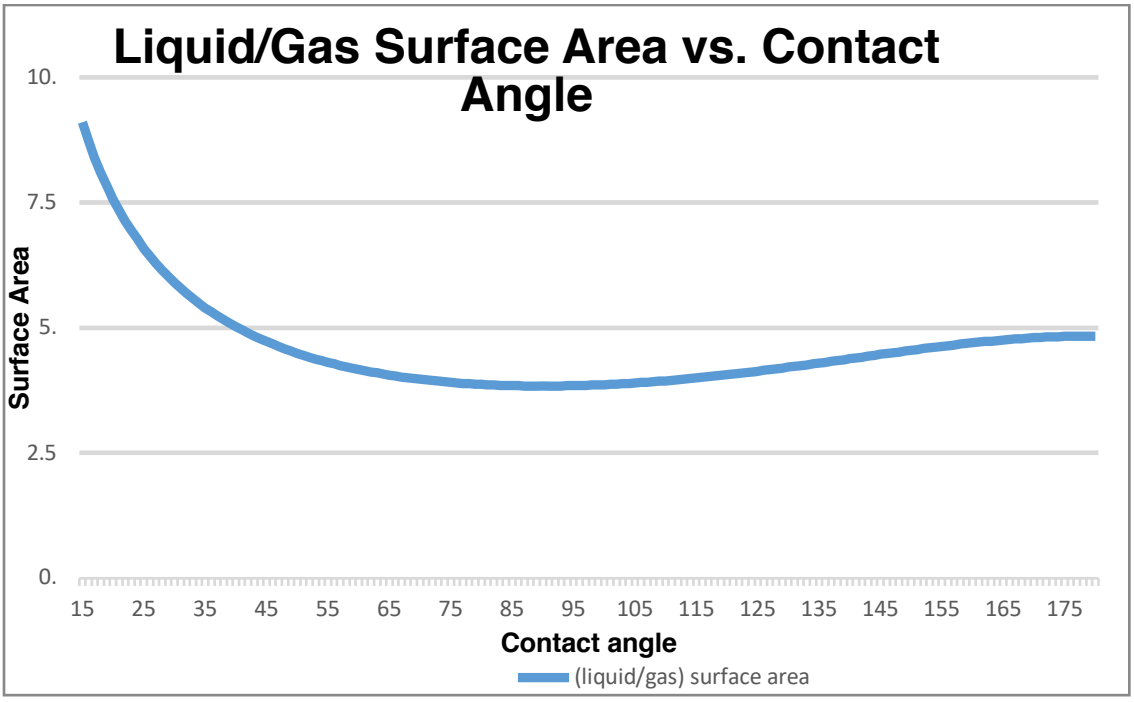

Figure 1.4: Surface area of Gas-Liquid interface vs Contact angle. Note: theoretical area is infinite at 0 degree contact angle

The above discussion shows that for a droplet, which creates a hemispheric shape (i.e., 90-degree contact angle), the Liquid-Gas surface creates no driving force to change the shape of the droplet and has no impact on the contact angle. Therefore, a droplet at a 90-degree contact angle must have equal Solid-Gas and Solid-Liquid surface energies. If the Solid-Gas and Solid-Liquid surface energies were different, then the droplet would change shape to balance the Solid-Gas and Solid-Liquid surface energies and minimize the total energy of the system. As such, a 90-degree contact angle can generally be thought of as a tipping point indicating if a system is more likely to be hydrophobic or hydrophilic.

This concept is important because all superhydrophobics rely on surface roughness, which exacerbates the impact of any surface energy differences. A surface cannot be superhydrophobic if it is smooth. So, a surface which can be made superhydrophobic, by adding roughness, will typically be made from a material which, when smooth, will form a droplet with a contact angle greater than 90 degrees. In most cases, if a droplet

forms a contact angle less than 90 degrees on a smooth surface then when roughness is added it will become hydrophilic.

To talk about roughness, the term, “projected area” needs to be introduced, which is the theoretical area of the Solid-Liquid interface if the surface was perfectly smooth. This projected area can be seen in Figure 1.3 above, as the circular surface area that is the bottom of the translucent hemispherical cap, which in this case would be $A = \pi \cdot a^2$. Projected area assumes that the surface is perfectly smooth. One can imagine how a liquid could be touching more surface area than the projected area as that surface becomes increasingly rougher. For now, continue considering smooth surfaces, in which the projected area of the droplet is the same as the area of the Solid-Liquid surface. To gain further understanding of how surface energies impact wetting we will start with the easier to conceptualize hydrophilic surfaces, where the droplet spreads out more (i.e., contact angles less than 90 degrees), then apply these concepts to hydrophobics.

Return to the example of a hemispherical droplet which is spreading over a surface. See the following plot (Figure 1.5) of the Liquid-Gas and Solid-Liquid contact areas; plotted against its contact angle. Moving from left to right represents a droplet which is spreading or flattening out on a surface.

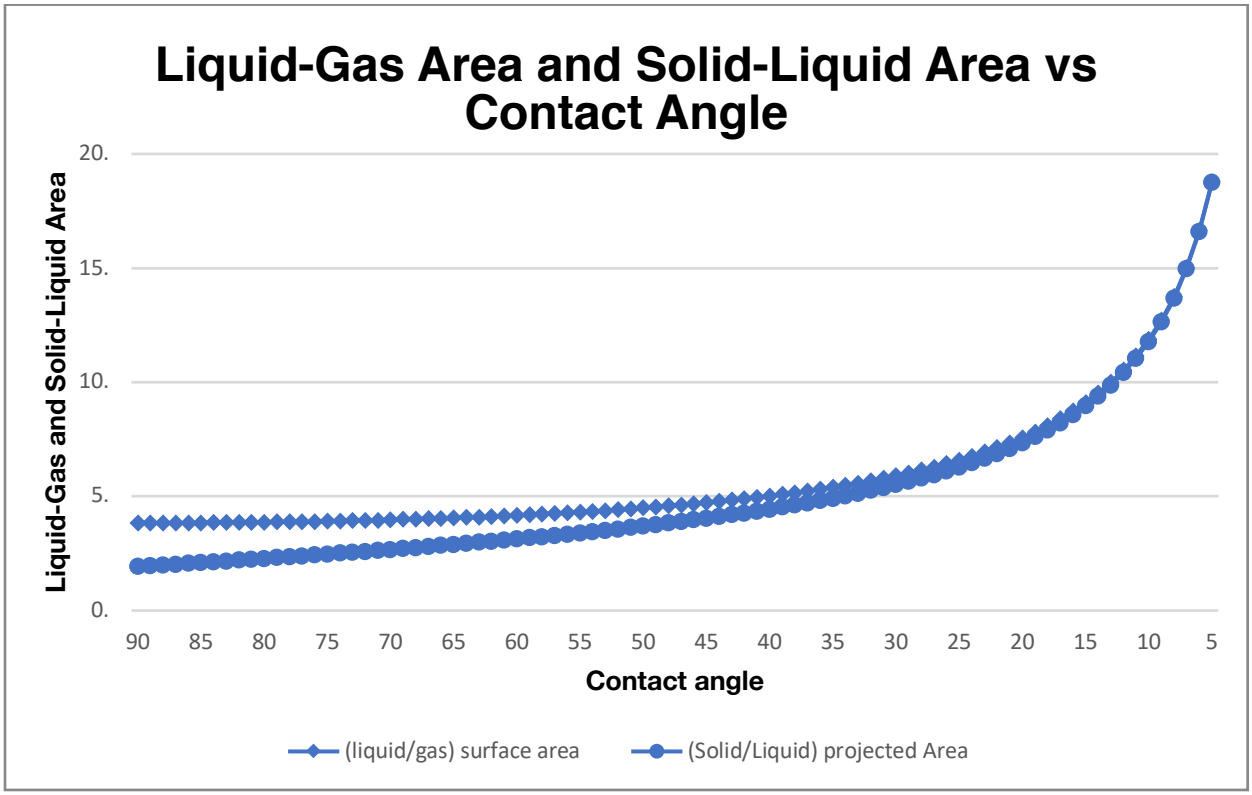

Figure 1.5: Liquid to gas and Solid to liquid surface area of a unit volume sphere as it spreads outward from being hemispherical shaped to flat on the surface

As can be seen starting at the left of Figure 1.5 above, when the contact angle is 90 degrees the Liquid-Gas surface area is twice the Solid-Liquid projected area. As the droplet spreads out the Solid-Liquid projected area increases more quickly than the Liquid-Gas surface area. To help visualize this droplet behavior, two (2) additional plots are shown in Figure 1.6, below:

1. Change in Surface Areas for Liquid-Gas and Solid-Liquid vs. Contact Angle
2. Ratio of Rate of Change in Surface Areas for Liquid-Gas and Solid-Liquid vs. Contact Angle.

These plots are for a droplet that wants to spread and starts at a 90-degree contact angle. Initially, the system has a notably higher amount of energy being released versus consumed due to a significantly larger change in the Solid-Liquid area per degree of change in contact angle. Remember, for contact angles close to 90-degrees, the Liquid-Gas surface area changes very little. However, as the contact angle of the droplet drops

below 90-degrees, the change in Liquid-Gas surface area quickly becomes significant. The stretching of the Liquid-Gas surface requires creating additional free surface of the liquid, in a similar way to that of cutting a bulk solid to make more surface. When the energy released from spreading, due to the difference in solid surface energies, equals the energy required by Liquid-Gas surface area stretching, an equilibrium point is reached. At this point, spreading stops and a static contact angle is achieved.

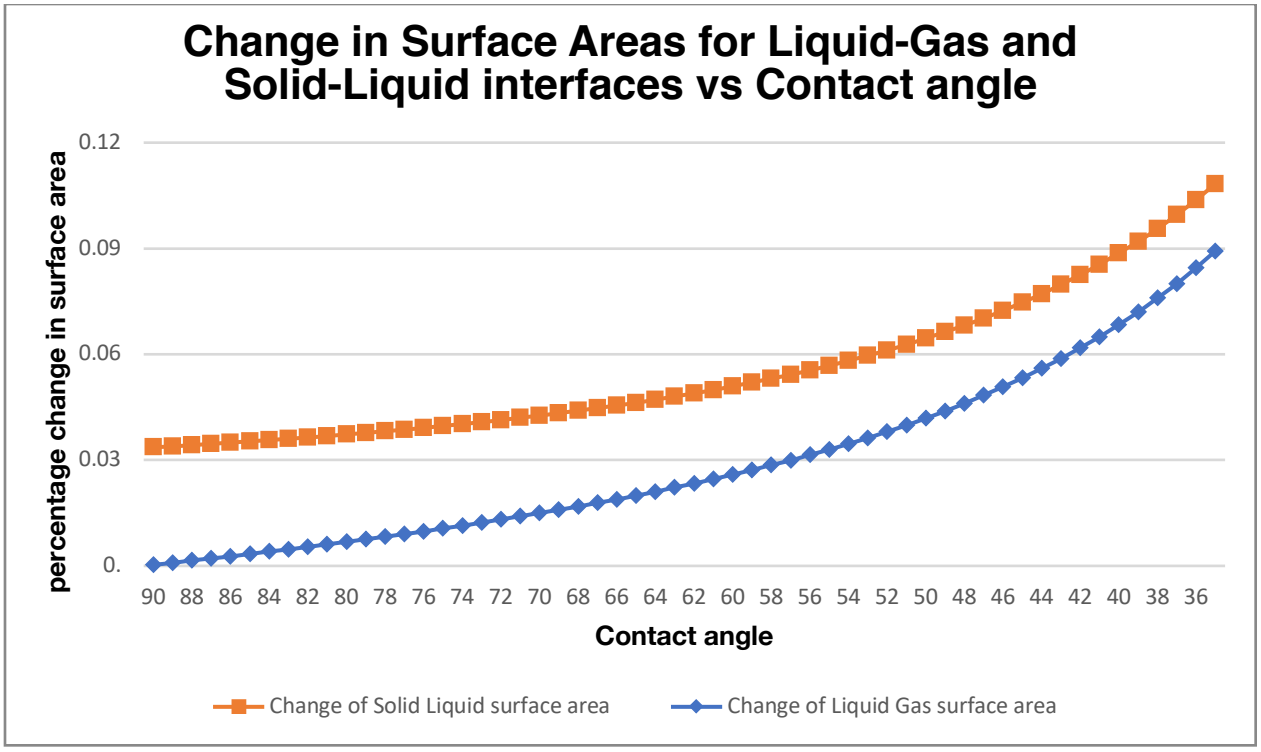

Figure 1.6: Change in Area of Liquid-Gas vs Solid-Liquid vs Contact Angle

Above, Figure 1.6 shows that near a contact angle of 90 degrees, the Liquid-Gas surface area changes very little for each degree change in contact angle. For example, at 88 degrees the Liquid Gas surface area only increases by 0.15% for a one-degree change in contact angle; however, at the same point the solid liquid contact area changes by 3.5%. The rates of change are somewhat similar with the Liquid Gas slope being somewhat steeper than the Solid Liquid slope, resulting in the surface areas converging as the contact angle approaches zero. Note: this plot only goes to a 36-

degree contact angle; however, at a contact angle of zero, the surface areas would converge and be identical.

Below, Figure 1.7 shows just how the system changes with respect to contact angle, highlighting that a 90-degree contact angle is a clear tipping point for the system.

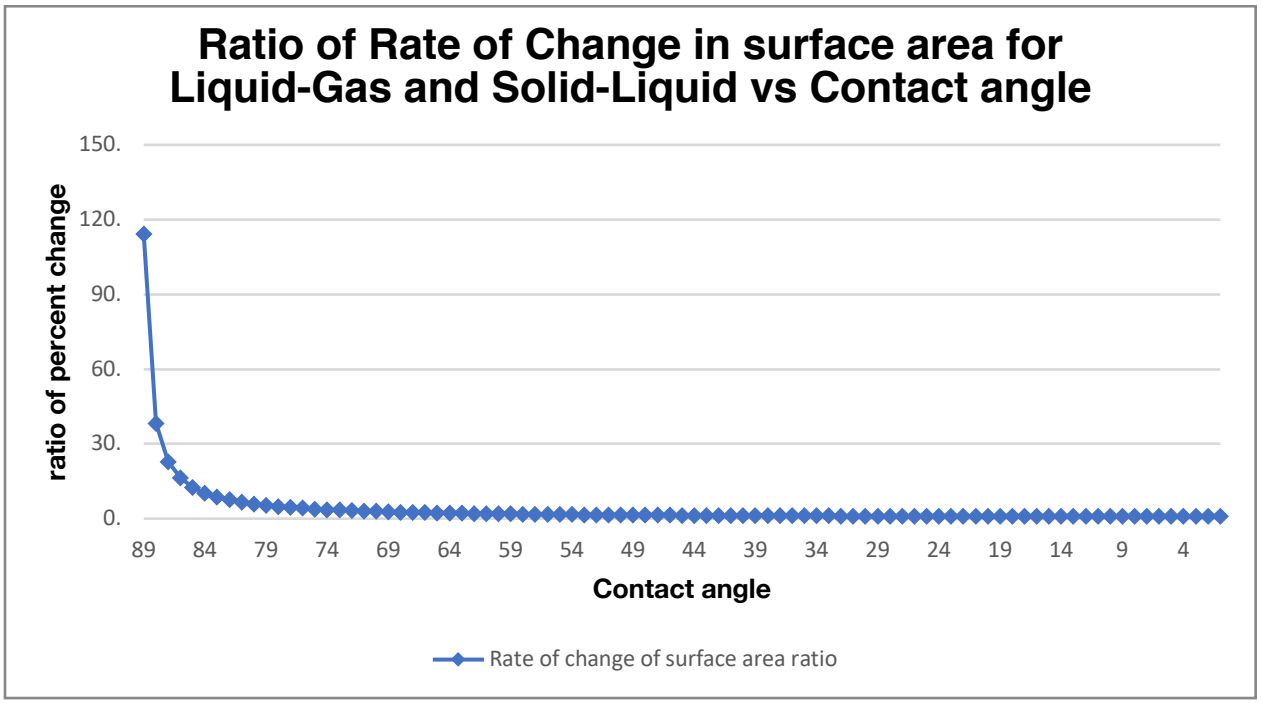

Figure 1.7: Ratio of change in area of Solid-Liquid area vs Liquid-Gas area for each degree change in contact angle

So far all these fundamentals have been applied to a droplet spreading; however, the same concepts can be applied to a droplet that is receding or one that is becoming more spherical. If a droplet is placed on a surface and this causes an interface energy which is higher than the Solid-Gas interface energy, then the droplet Solid-Liquid contact area will start to recede from a hemispheric shape to become more spherical. As was true for the spreading droplet, because the Solid-Liquid surface energy is higher than the Solid-Gas surface energy, excess energy will be released as the droplet regresses and less liquid remains in contact with the surface. As was shown in Figure 1.4, for a droplet to change from hemispherical to spherical there is still an increase in the Liquid-Gas surface area though less drastic as can be seen from the curve in the plot as contact angle increases towards 180 degrees. Again, just as it was true for

spreading, an equilibrium point will be reached where the energy released from the droplet receding is no longer enough to stretch the droplet's surface area as is required to make it more spherical. This becomes increasingly difficult because as the droplet contact angle approaches 180 degrees there becomes almost no remaining Solid-Liquid area to cause the driving force to stretch out the Liquid-Gas area. The lack of a driving force makes it very difficult to achieve a spherical shape. Again, during the energy balance process, there is an equilibrium point reached, in which the small change in Solid-Liquid area does not release enough energy to counter the energy consumed by creating new surface area when making the droplet more spherical.

1.5 Mathematical relation for a smooth surface:

It was Thomas Young who first published these energy correlations as to the spreading of a droplet on a surface and developed the mathematics to represent them. These equations apply to smooth surfaces and because of his work the contact angle on a smooth surface is often referred to as the Young's contact angle. The balance of these energies is found as follows:

$$cos\,\theta = \frac{\gamma_{sg} - \gamma_{sl}}{\gamma_{lg}} \quad (1)$$

Where γ_{sg} γ_{sl} , and γ_{lg} are the Interfacial energy between solid-gas, solid-liquid and liquid-gas respectively. The interface energy is the surface energy minus any bonding that happens. The Youngs equation shows that if the solid gas interface energy (γ_{sg}) is less than the solid liquid energy (γ_{sl}) the numerator will be negative and therefore the contact angle, θ, must be greater than 90 degrees. For this to be the case the bonding between the solid and the liquid need to be minimal. Additionally one can see that if the solid has a high surface energy then this will lower the delta between γ_{sg} and γ_{sl} and therefore keep the contact angle closer to 90 degree.

Chapter 2 Literature Review

2.1 Wenzel state:

A superhydrophobic surface is primarily achieved by taking a surface, which when smooth, has a contact angle greater than 90 degrees, known as being hydrophobic (i.e., $\gamma_{sg} < \gamma_{sl}$), and adding some amount of surface roughness. So far only smooth surfaces have been considered, but if the surfaces are rough, then as the droplet spreads or recedes, and its projected area changes, the actual contact area will change more than the projected area. Therefore, if a hydrophobic surface has twice the free area due to roughness it would act the same as a smooth surface with twice the Solid-Gas interface energy and twice the Solid-Liquid interface energy, doubling the delta energy released [18].

Mathematically *r* is defined as the roughness factor; equivalent to $\frac{3D\ Surface\ Area}{2D\ Surface\ Area}$

To calculate the resultant contact angle take the roughness factor and multiply it by the interface energies that come into contact with a solid surface.

$$cos\,\theta_{Rough} = \frac{r \cdot \gamma_{sg} - r \cdot \gamma_{sl}}{\gamma_{lg}} = r \cdot \frac{\gamma_{sg} - \gamma_{sl}}{\gamma_{lg}} \quad (2)$$

It was Wenzel [18] who first discovered and published this relationship, and the equation below is commonly referenced for the contact angle of a rough surface, which states that the cosine of the contact angle in the Wenzel state is equal to the roughness multiplied by the Young's contact angle. (i.e., what the contact angle would be for a smooth surface)

$$cos\,\theta_{Wenzel} = r \cdot cos\,\theta_{young} \quad (3)$$

Represented as follow:

$$cos\,\theta_{W} = r \cdot cos\,\theta_{e} \quad (4)$$

The above relationship applies to both spreading and receding of a droplet, but moving forward this thesis will focus on receding, as this is what applies to hydrophobics. However, this useful insight into the effect of roughness on the wetting of surfaces by Wenzel did not cover an important and very relevant case found in super hydrophobics.

2.2 Cassie-Baxter state:

If a surface is discontinuous or very rough, the liquid ends up suspended and therefore also has a liquid-gas interface on the surface side (i.e., the bottom of the droplet). This has an interesting effect on the system. The Solid-Gas and Solid-Liquid energy differences act on smaller areas because there is less area for the droplet surface to contact. However, retraction of the droplet across the surface also corresponds with a release of energy, which is equal to the now destroyed Liquid-Gas interface [19]. This is known as the Cassie-Baxter state (Figure 2.1b) as compared to the Wenzel state (Figure 2.1a). Figure 2.1a (left) also serves as a good visualization of how the Solid-Liquid area is greater than the projected area in the Wenzel state.

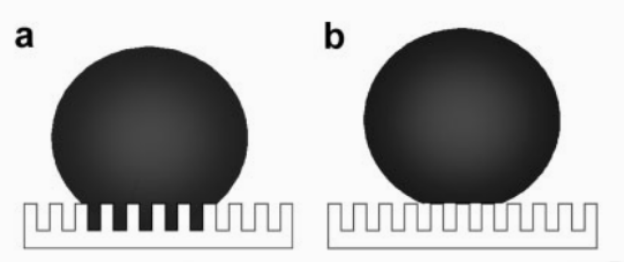

Figure 2.1: Surface Wetting a) Wenzel state b) Cassie-Baxter state

By Wang [1].

As is implied by the name it was Cassie and Baxter [19] who calculated the contact angle when the surface contact is discontinuous, which can be represented as follows:

$$cos\,\theta_{Cassie-Baxter} = r \cdot A_{SL}(cos\,\theta_e) - A_{LG} \quad (5)$$

Where A_{SL} is the solid area fraction that is a Solid-Liquid contact, r is again the roughness of the area represented by A_{SL} (if it is rough) and A_{LG} is the solid area fraction that is a Liquid-Gas contact surface. An interesting example is to imagine a droplet floating in space; it would have no solid liquid interface, resulting in an A_{SL} of zero and a A_{LG} of 1, giving $cos\theta_{Cassie-Baxter} = -1$; and therefore a contact angle of 180 degrees. This thought experiment helps understand the advantage of being in the Cassie-Baxter state. A droplet in contact with nothing wants to be a sphere, and it being less in contact with the surface takes advantage of this natural phenomenon.

From here on out φ_s will be used to represent A_{SL} and therefore, A_{LG} as $(1 - \varphi_s)$ because the sum of the solid area fractions must be one (1).
The equation is as follows:

$$cos\,\theta_{Cassie-Baxter} = r \cdot \varphi_s(cos\,\theta_e) - (1 - \varphi_s) \quad (6)$$

The reason this wetting situation is so important is because it typically has a lower hysteresis. The droplet has discontinuities and the Liquid-Gas interface on the bottom

side of the droplet does not resist the droplet from rolling. It is almost a requirement that a droplet be in the Cassie-Baxter state to be superhydrophobic.

2.3 Comparison of droplet states:

The more important question becomes, “When will a droplet sit on a surface as in the Cassie-Baxter case and when will a droplet penetrate into the roughness as in the Wenzel case?” It has been shown mathematically by Patankar that the lower the contact angle, the lower number of degrees, corresponds to a lower energy state [20]. This leads to two important considerations:

1. When does one state have a contact angle lower than the other?
2. What is the energy barrier required to move between these two states?

First consider, "Which state has the lower contact angle?” This is based on both the surface roughness and the surface energy of the material, which will be based on the smooth or Young’s contact angle. This is nicely visualized on a few plots by Patankar, which are presented on the following pages.

Wenzel’s theory predicts that if the absolute value of Cosine of the Young’s contact angle is greater than or equal to the absolute value of -1 divided by the roughness ratio (r), $|\cos\theta_e| \geq |-1/r|$, then the contact angle would be 180 degrees. From this expression it can also be concluded that the contact angle will be 180 degrees when $\theta_e > cos^{-1}\left(\frac{-1}{r}\right)$. This mathematical prediction by the Wenzel theory, plotted in Figure 2.2, was tested in a number of papers and shows good agreement experimentally [20]–[22]. This plot is for a surface with a given roughness (r), the y axis is $\cos(\theta_r^w)$ where θ_r^w is the “realized contact angle” (also called the apparent contact angle) and the X axis is $\cos(\theta_e)$ where (θ_e) is the Young’s or smooth contact angle which is a property of the material. This plot serves to give the reader a better conceptual understanding of the theory. For a surface with a given Young’s contact angle (θ_e), the roughness at

which it would form a 180-degree apparent contact angle, while in the Wenzel state, is when the roughness ratio is the same as cos(θ_e).

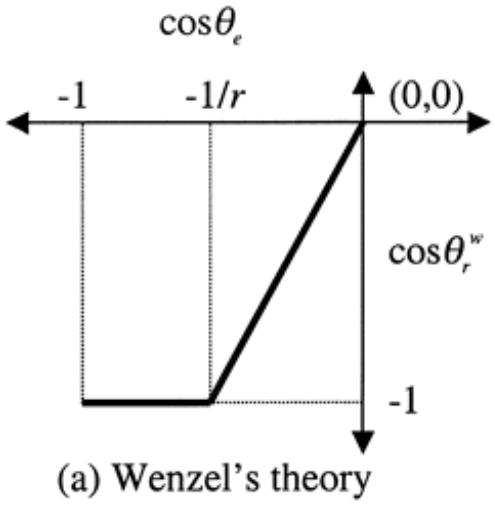

Figure 2.2: Plot of Wenzel contact angle vs roughness of a surface with a given young's contact angle. [20]

Consider an example with a Young's contact angle of 100 degrees. Plugging in cos(100) is roughly (-0.174). Thus to achieve a contact angle of 180 degrees by adding roughness we need (-0.174) to be slightly to the left (more negative) than -1/r. Consider a roughness ratio (r) = ~5.8 gives -1 / 5.8 = -0.172. This is roughly the roughness to make cos(100) a larger absolute value than -1/roughness ratio.

Now consider the Cassie-Baxter equation, for this the area fraction of Solid-Liquid interface (φ_s) must be considered. This is shown below, assuming flat top pillars because the geometry of the surface also impacts this plot, which is covered in more detail later on. In the Cassie-Baxter representation the contact angle only reaches 180 degrees for a surface with a Young's contact angle of 180 degrees, and the minimum contact angle for a lower Young's contact angle increases for a greater area fraction of Solid-Liquid interface (Figure 2.3).

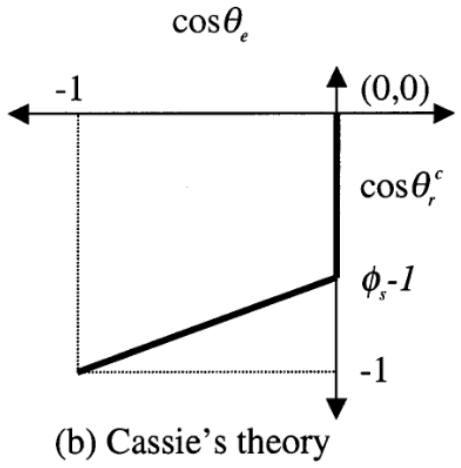

Figure 2.3: : Plot of Wenzel contact angle vs roughness of a surface with a given Young's contact angle [20]

Next, consider for a moment the comparison of the Wenzel and Cassie-Baxter case for a rough surface with given *r* and φ_s (area fraction of Solid-Liquid interface) giving the following plot, Figure 2.4. Moving from right to left, represented by a larger negative value of $cos\ \theta_e$, represents a surface with an increasing Young's contact angle. That is $cos\ \theta_e$ of zero (0) would have a contact angle of 90 degrees and at negative one (-1) would have a contact angle of 180 degrees. These plots only refer to surfaces which are hydrophobic and have a Young's contact greater than 90 degrees; these mathematics again reiterate the significance of a 90-degree Young's contact angle as a tipping point. For a slightly Young's hydrophobic surface, the lowest energy state is the Wenzel state and for a more Young's hydrophobic surface it's the Cassie-Baxter state [20]. Meaning, for a $cos\ \theta_e$ closer to zero (0) the lowest contact angle is for the Wenzel state and for a $cos\ \theta_e$ closer to negative one (-1) the lowest contact angle is for the Cassie-Baxter state. Recall that the lower contact angle correlates to the lower energy state, again this was shown mathematically by Patankar [20].

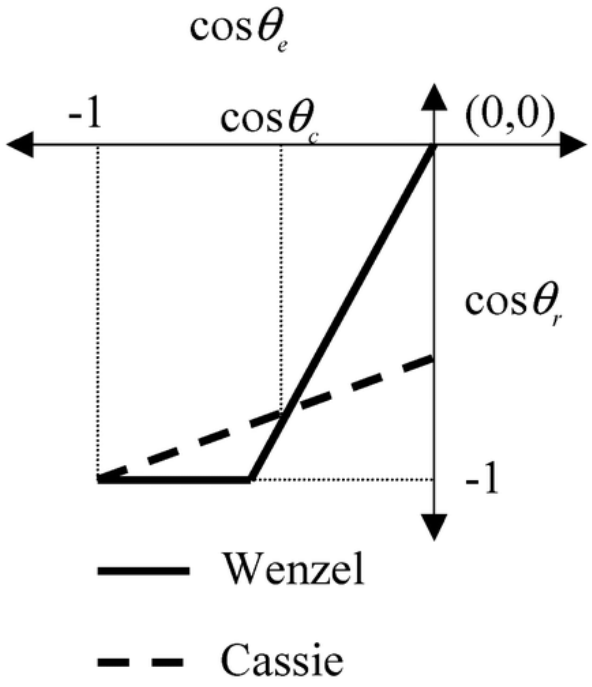

Figure 2.4: Comparison of the theoretical realized contact angle for both Wenzel and Cassie equations as surface condition change in hydrophobicity [20].

θ_c is the contact angle of the crossing point from Wenzel to Cassie. For $\theta_e > \theta_c$, the Wenzel state wetting contact gives a lower realized contact angle, and for $\theta_e < \theta_c$, the Cassie-Baxter contact gives a lower realized contact angle. This infers that, there is some roughness and base surface energy which results in a contact angle of θ_c which represents the turning point between the two wetted states. If the surface has a contact angle greater than θ_c the lower energy state would be the Cassie Baxter state. Recall that the lower contact angle, the lower the energy state [20]. Here a value of $\cos(\theta_r)$ which is closer to zero (0) represents a lower contact angle. For example if the angle of $\cos(\theta_e)$ is large the corresponding location on the graph would be to the left of θ_c. If a line were drawn vertically down, the dotted Cassie-Baxter line is the one intersected first. The Cassie-Baxter line has a smaller absolute value for $\cos(\theta_r)$ therefore has a lower energy state, and a lower contact angle.

An understanding of this droplet behavior is critical when designing hydrophobic surfaces and introduces an important new point. For many superhydrophobic surfaces the material will have a smaller Young's contact angle (less than $cos\ \theta_c$) and will get its

hydrophobics from roughness. However, it is often that the Cassie-Baxter state is the situation first encountered by the droplet when it is placed on a surface. The question becomes when and how would the droplet transition to the Wenzel state which has a lower contact angle, and a lower energy state.

The study by Patankar was expanded on by Bico *et al* [21] in Figure 2.5. This plot more typically represents real world conditions. The left side represents a hydrophobic surface and shows the theoretical Cassie-Baxter relation for the two (2) geometries shown below; the dashed parabolic line representing the hemispherical bumps and the solid line the flat top pillar. The hemispherical bumps show a noticeable increase in contact angle because they have a higher roughness for the same area fraction of Solid-Liquid contact. The right side is the Wenzel equation's impact on the hydrophilic surface. A roughness of 1/r gives a zero (0) degree contact angle, which conceptually corresponds to a wicking surface [21], like a sponge or frosted glass.
It is important to remember that the lower the contact angle the lower the energy state. This also points out an important concept, the Cassie-Baxter state will be the first state encountered by a droplet being placed on a surface and it will have to transition.

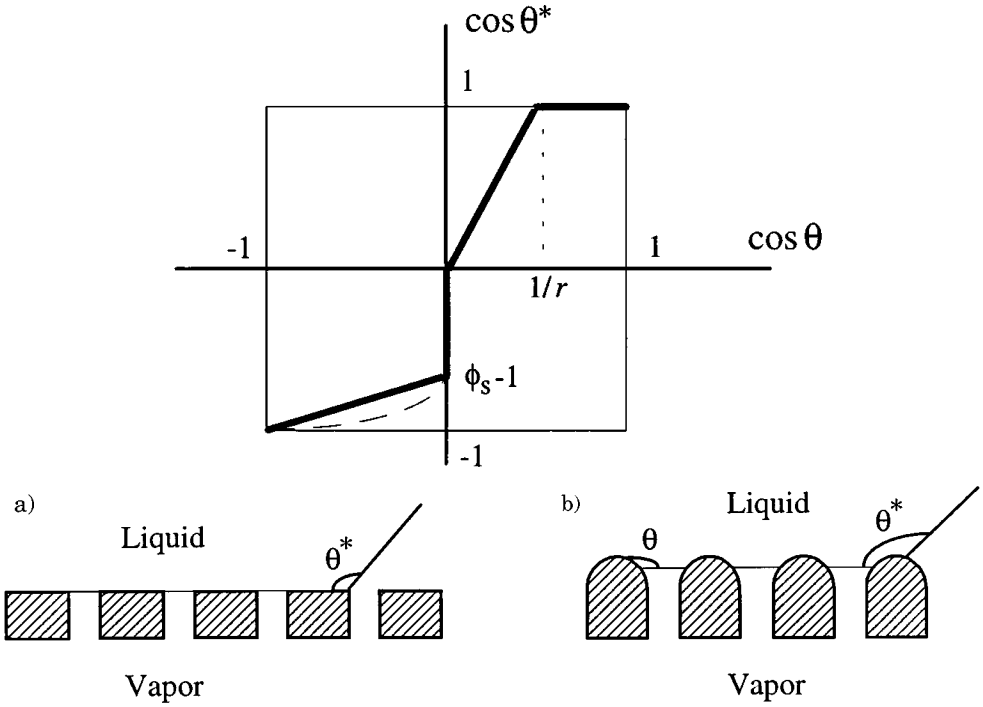

Figure 2.5: Liquid deposited on a model surface with holes (a) crenellated surface; b) hemispherical bumps): for contact angles larger than π/2, air is trapped below the liquid, inducing a composite interface between the solid and the droplet, and therefor is represented mathematically, by Cassie-Baxter [20].

2.4 Droplet penetration into a surface:

For a transitioning droplet a great example given by Patankar [20], a droplet is slowly making its way down pillars to wet the bottom of a rough surface. See Figure 2.6 below.

Initially the contact angle is represented by the Cassie-Baxter equation (6)

$$-\cos\,\theta_{\mathrm{r}}^{\mathrm{c}} = -\varphi_{\mathrm{s}}\cos\,\theta_{\mathrm{e}} + (1 - \varphi_{\mathrm{s}})$$

And in the Wenzel state would be represented by Equation (4),

$$-\cos\,\theta_{\mathrm{r}}^{\mathrm{w}} = -r\cos\,\theta_{\mathrm{e}}$$

but in the intermediate area, the behavior would be represented by the following Equation (7):

$$-\cos\theta_r^{int} = -(r - 1 + \varphi_s)\cos\theta_e + (1 - \varphi_s) \quad (7)$$

The difference being that the term leading the cos in the Cassie-Baxter equation is now $-(r - 1 + \varphi_s)$ instead of just the solid liquid area fraction (φ_s). Recall "r" is the roughness factor defined as $\frac{3D\ Surface\ Area}{2D\ Surface\ Area}$ and therefore must always be greater than or equal to one, and in many cases much larger than one. As such, for a droplet to transition from Cassie-Baxter to the Wenzel state the system would require some input of energy to drive the transition [20].

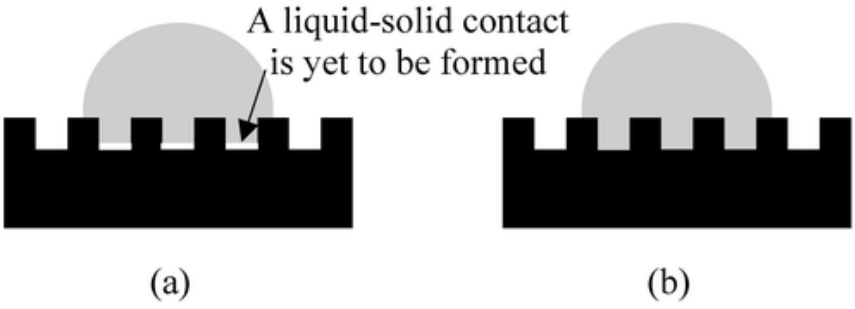

Figure 2.6: Visualization of droplet transition from Cassie-Baxter to Wenzel state [20].

This transition has been studied in depth on manufactured pillar structures [23]–[26]. Droplet impacts, pressure from submersion, pressure from a solid outside object, or the force created as trapped water dissolves into the air, could all cause this transition. [20], [27] Pillar structures are commonly manufactured, but these surfaces often fail from the buckling of pillars under pressure or impact [24].

This leads to some interesting considerations. Most importantly is that fundamentally, surfaces with high Young's contact angles (i.e., and therefore low surface energies) are also very weak mechanically. And so, a functional superhydrophobic surface will likely be made of a material with a mild Young's contact angle, close to but more than 90

degrees; and with a higher surface energy, but less mechanically weak. The superhydrophobic properties will be driven by the geometry of its surface more than its surface energy.

One potential surface geometry would be a closed cell porous surface with a mild Young's contact and with a high roughness. However, upon impact, a droplet might penetrate into the surface and fill some voids. With a void filled it would take significant energy to create the needed Liquid-Gas interface in order to free itself from the surface; or it must leave the trapped liquid behind. As such, it would be pinned to the surface and would not prove to be a robust hydrophobic surface.

Alternatively, a similar surface might have an open cell lattice. Typically, pinning would still be an issue as the droplet reaches the substrate; however, if the surface geometry is deep, relative to feature length of the structure, an open cell surface could become an enormous barrier to transition.

Take the hypothetical 2D Case below for a pillar surface with a Young's contact angle of 100 degrees and an initial Solid-Liquid area (φ_s) of 0.5 and no surface roughness. See Figure 2.7 below:

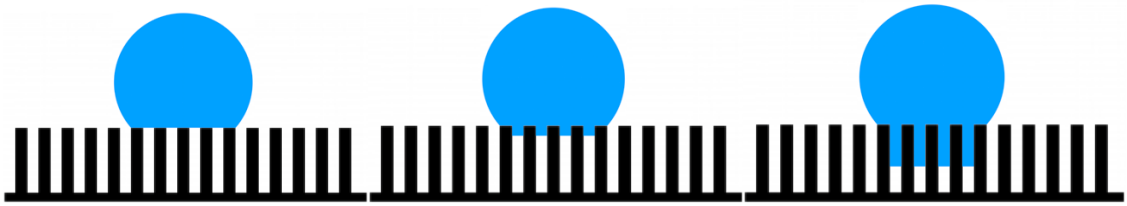

Figure 2.7: Visualization of example problem of droplet trying to transition from Cassie-Baxter to Wenzel states

Initially: $-\cos(\theta_r^{int}) = -(1 - 1 + 0.5) \cdot \cos(100) + (1 - 0.5) \rightarrow \theta_r^{int}$ 125.9-degree

As the droplet penetrates into the surface, the effect of air gaps from the area fraction of Solid-Liquid contact still affects the Cassie-Baxter portion of the equation, but now there also is a roughness. The projected area of the Solid-Liquid interface has not changed

but the actual Solid-Liquid interface area has increased; therefore, increasing the roughness. This is similar to the effect of the hemispherical bumps in Figure 2.5. Let us assume the droplet has penetrated the surface by a distance of exactly the width of one pillar. For the example in Figure 2.7 the projected Solid-Liquid interface area is five (5) units, but the Actual Solid-Liquid interface area is (13) units, giving a roughness of (13 / 5).

Updating the equation from before with these values gives a new theoretical contact angle:

$$-\cos(\theta_r^{int}) = -(13/5 - 1 + 0.5) \cdot \cos(100) + (1 - 0.5) \rightarrow \theta_r^{int} = 149.8\text{-degree}$$

Below is a plot of this example from the initial state of resting on top of the pillars, to a state where the droplet reaches a theoretical contact angle of 180 degrees.

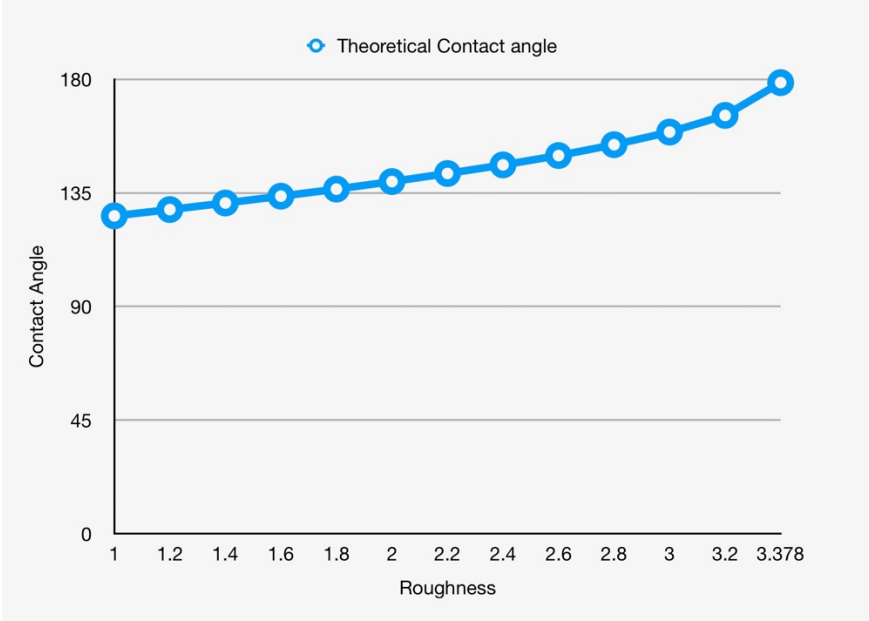

Figure 2.8: Theoretical contact angle vs surface roughness for a material with a Young's contact angle of 100 degree and a pillar structure. See Figure 2.7

As shown in Figure 2.8, above, there is a substantial increase in theoretical contact angle as the droplet is pressed into the surface. This is because roughness is defined by the amount of actual Solid-Liquid contact area vs the projected surface area. Pressing a droplet into a rough surface is essentially generating the condition of a

rougher surface. This results in a large energy barrier against penetration into a surface and the droplet will aggressively try to return to the Cassie-Baxter state of approximately a 125.9-degree contact angle. This plot shows the theoretical limit of this equation; however, with an external pressure, the droplet may try and penetrate even deeper, still consuming energy, but with ever increasing difficulty. This is an important consideration for surfaces that may be subject to impact or submersion. This concept was investigated in detail by Zheng et al. who provide further insight into this transition. They particularly look into stability vs pillar height and show pillars need to be tall and slender to have more stability against penetration [25 - 26].

2.5 Carbon soot surfaces:

At this point enough concepts have been covered to start focusing specifically on tuned carbon soot surfaces. Their first key attribute comes from their layout, something previously overlooked in our investigations. Compared to the pillar structures commonly used for superhydrophobics, the tuned carbon soot surfaces produced at the Virginia Commonwealth University (VCU) functional materials lab are comprised of an interwoven lattice, figure 2.9 [16], [29]. The carbon nanoparticle surface is structurally sound in multiple directions and would exhibit the conceptual similarities of an increase in roughness due to penetration as that of a pillar. A simple pillar surface with large height-to-width ratios presents a large barrier to penetration but are also some of the most fragile structures. They often buckle, get knocked over from side loading or bundle together from capillary forces [24], [28]. The linked chains from VCU's soot surfaces are only semirigid with longer structures being observed swaying slightly under SEM. This allows the soot surfaces to deform slightly under load. As the linked chains become compacted together due to the load of the droplet, more points come into contact with the liquid. Therefore, the compacting of the lattice technically lowers the surface area fraction of Liquid-Gas interface, which would result in a lower contact angle compared to a droplet just touching on fewer points. While this does lower area fraction, it also is valuable for a functional surface. The top linked chains deformation is dependent upon

the amount of applied force, allowing the droplet more points of contact and distributing the load. This protects the surface from damage, allowing it to resist impact or submersion, but also retains a large gas boundary below the droplet preventing it from penetrating to the substrate.
Being able to tune the stiffness of the surface would be quite valuable, with the ideal scenario being that under low load the droplet rolls on as few points as possible, without causing damage. However, under higher load the surface compacts, having more points of contact and a lower contact angle, but retraining its structural integrity. This allows for reasonable anti-wetting properties under all loads and the ability to return to its undeformed, mostly superhydrophobic, state. This deformable surface behavior could theoretically be quite valuable for droplet impact. For example, as a droplet impacts a surface, the energy is redirected from normal to perpendicular, as the droplet spreads out across the surface. As the downward forces lessen, particularly as the droplet finishes spreading, then the semi-ridged surface can return to its less compacted state and the droplet rides on fewer points, exhibiting exceptional anti-wetting properties. This same concept can extend to roll-off in general, where the receding edge of the droplet is experiencing less load and therefore will deform to a state of even fewer points of contact and exhibit more hydrophobic properties.

It was reported by Esmeryan et al that by varying the air flow in the combustion, the bonding, hydrophobicity and stability of the soot changed [16], [17], [29]. Under the correct, lower oxygen conditions, the soot formed diamond like carbon bonding (DLC) [29]. These DLC bonds are very strong, leading to a surface with surprising structural properties. However, we did not fully understand why some of the surfaces manufactured in our lab were much more robust and superhydrophobic than others. First, it had been found that DLC has a relatively low contact angle, often around or slightly below 90 degrees [30]. In our previously conducted experiments there were multiple uncontrolled variables and it was clear more was at play than had been uncovered [16], [17], [29]. The fine-tuned system highlighted that not only is there a critical transition to the ideal chained sphere surface, but the size of the spheres in the chain correlated strongly to the hydrophobics of the surface. In the following figure of

previous samples made in the VCU lab by Esmeryan et alia (Figure 2.9) Clearly the chain sphere diameter is impacted by the combustion conditions, but for these samples is not uniform, with multiple sizes apparent in each sample. The updated design, used for the samples in this thesis, was able to overcome these inconsistencies and created uniform spheres of varying size; allowing for an investigation into the impact of sphere size on our superhydrophobic surfaces.

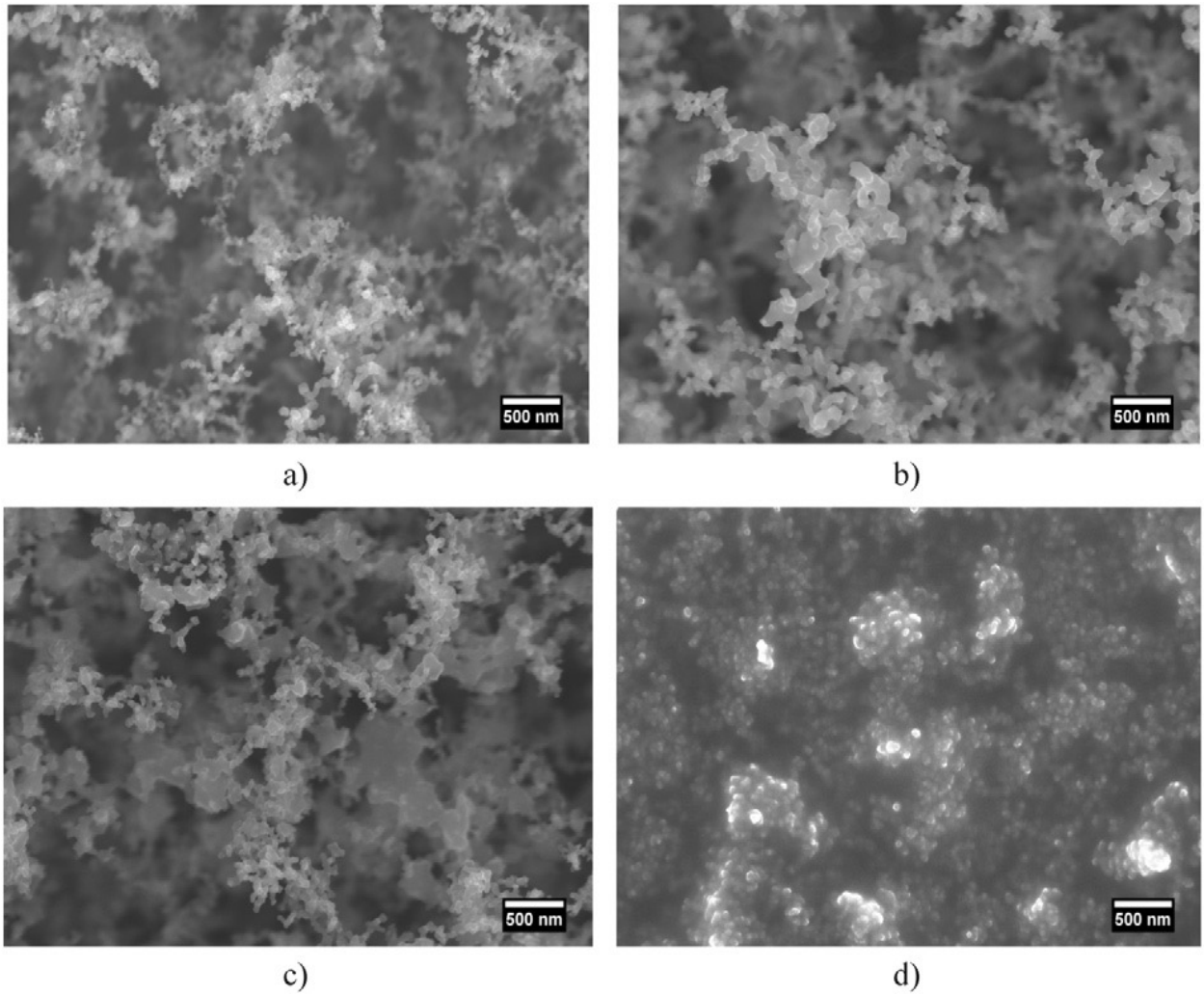

Figure 2.9: Scanning electron micrographs of carbon nanostructures deposited at wick dimensions of 1.2 × 2.5 cm and L ~ 3 cm via a) an open flame and b) upon controllable combustion at an air flow of 0.0042 m3/min, c) 0.0033 m3/min and d) 0.0024 m3/min [29]

Chapter 3 Methodology

This journey into understanding superhydrophobic soot began when I learned the current common method for creating hydrophobic soot surfaces was to hold a sample, often glass or metal, over an open flame. This created a very fragile surface. A droplet placed on the surface would become black, as it became coated with soot. As the droplet rolled it would peel the soot off the surface, and running water would simply wash the soot away. It was completely uncontrolled, with the fuel source being the only controlled variable.

3.1 A simple chimney:

It seemed an intuitive first step to add a chimney to minimize the impact of air movement and to direct the exhaust upwards (see Figure 3.1). The first chimneys were made by twisting and cutting a sheet of thin gauge stainless steel foil and cutting an opening for air to enter at the bottom. Initially the chimneys were made with different sized openings followed by the addition of a sleeve which allowed the door size to be adjusted by partly covering the opening, see Figure 3.1 [17]. Paper towel was folded and rolled into a cylindrical wick and was placed into a glass dish filled roughly with half an inch deep of rape seed oil. A glass slide was then held over the chimney and the soot sample was collected [17].

Changing the inlet size changed the oxygen-to-fuel ratio which changed the soot composition [17].

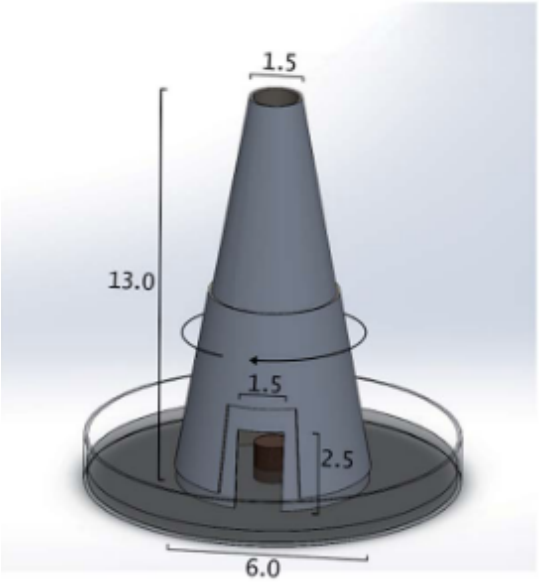

Figure 3.1: Stainless Steel cone with adjustable flow rate opening [17]

The largest impact was that some of the soot formed sp3 bonds, which is a diamond-like carbon (DLC). This structure is substantially more robust than the predominantly sp2 bonded carbon, typically found in the non-modified soot sample and resulted in a more stable surface. This discovery resulted in 2 publications [17] and [6].

The ideal anti-wetting surface is superhydrophobic, having a contact angle over 150 degrees, with a low hysteresis and a low roll-off angle. Finally, surface adhesion and robustness must allow the surface to maintain its shape and a thickness which provides a sufficient barrier against water penetration to the substrate.

3.2 Air flow controlled combustion:

In search for such a robust hydrophobic surface, precise control over the oil combustion would be necessary. The next improvement was to get rid of the simple cut-out opening used for inlet air adjustment and replace it with a forced air system with an adjustable flow rate meter. An Intex 12v dc air pump was fed through a flow rate controllable meter (McMaster Carr 5079K25)

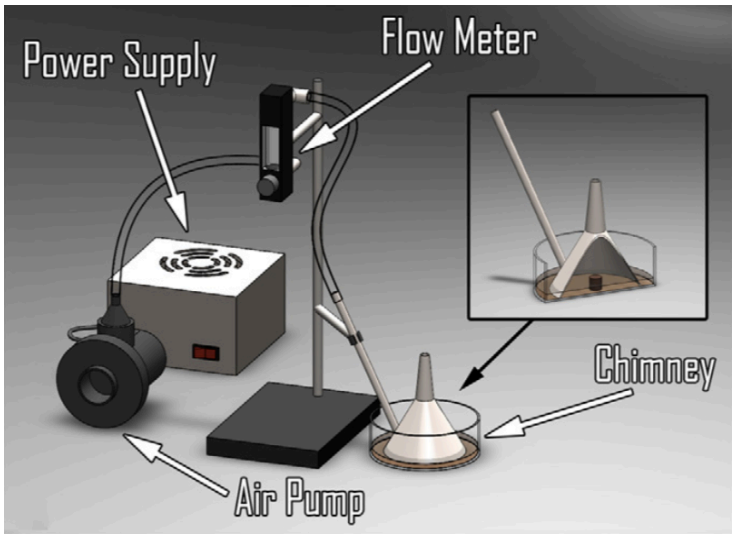

Figure 3.2: Updated design of soot system. Forced air, flow rate meter with flow control knob [29]

and then directed into the base of a new funnel. See Figure 3.2 [29].
This gave substantially better control and repeatability to what turns out to be a fairly sensitive system. Again, the wick was placed in a glass dish filled with half an inch of rapeseed oil. Next, the air pump was turned on and the flow set to roughly 2,500 CCM. The wick would then be lit and the chimney placed over top of the wick. The flow would be adjusted and tuned between 1400 and 5200 CCM for sample collection. Samples were coated from the exhaust out the top. This led to a number of publications including [16], and [29].

Still more control was needed, ideally the system would no longer have a paper wick, and would have control over flowrate of fuel, oxygen and inert gas for the combustion process. This trial-and-error process led to some serendipitous discoveries and valuable insights, which are chronicled below.

3.3 A better wick:

The first attempt was to replace the paper wick, used previously in VCU's lab, with a ceramic one. Several ceramic materials were tested, from porous alumina to glass fibers. See Figure 3.3.

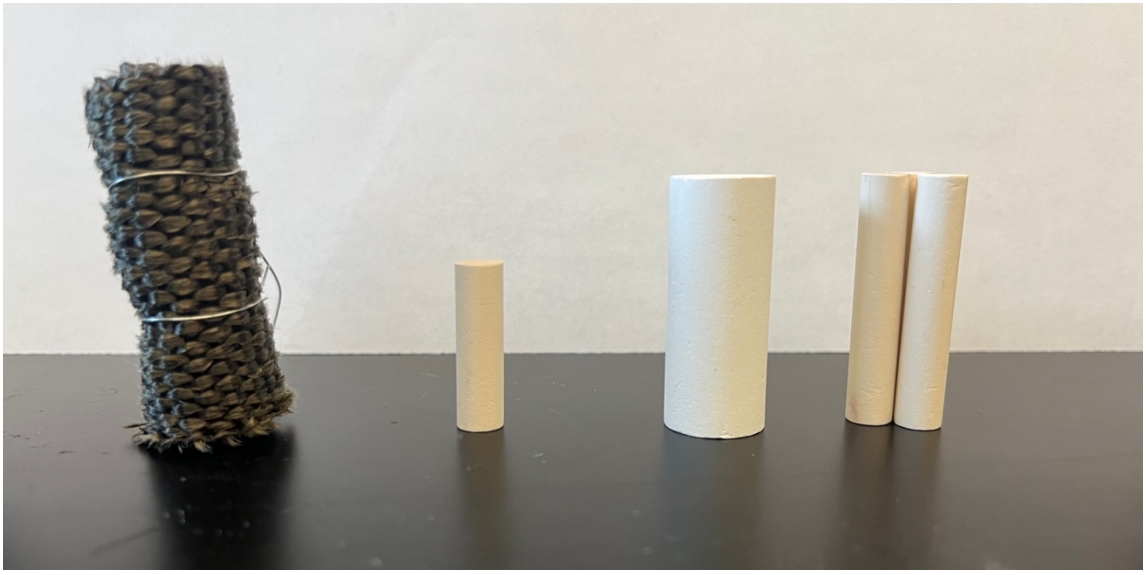

Figure 3.3: From (Left to Right) fiberglass wick, small ceramic wick, large ceramic wick, group of small ceramic wicks

Finding an ideal wicking material was difficult, and I discovered a new-found appreciation for candles, as they are inherently good at maintaining a constant burn rate while keeping their wick wet. It seemed a ceramic wick could not produce a large enough stable flame. The ceramics did not have the capillary force to move the oil to the center of the wick unless the wicks were very small in diameter. A small wick proved to be problematic with our relatively large system and the chimney did not have much effect on such a small flame. A more technical method for creating and modifying carbon soot coatings needed to be developed.

3.4 Removal of the wick from the system:

3.4.1 Hot wire coil:

The next attempt was to remove the wick all together and replace it with a very low flow rate fogging nozzle (Figure 3.5) to spray the oil through a hot wire coil (Figure 3.4). A few problems arose here, the first of which being that very low flow rate nozzles are hard to source. The second problem was that while the flame might sustain itself, it takes a lot of energy and a high temperature to vaporize and ignite the oil mist. Lastly, if these conditions were met, the additional energy put in the system from the combustions was instantly enough to melt the coil used for ignition. For this to work a much thicker wire and a lot more energy would be needed. Such a system began to become unsafe and was abandon.

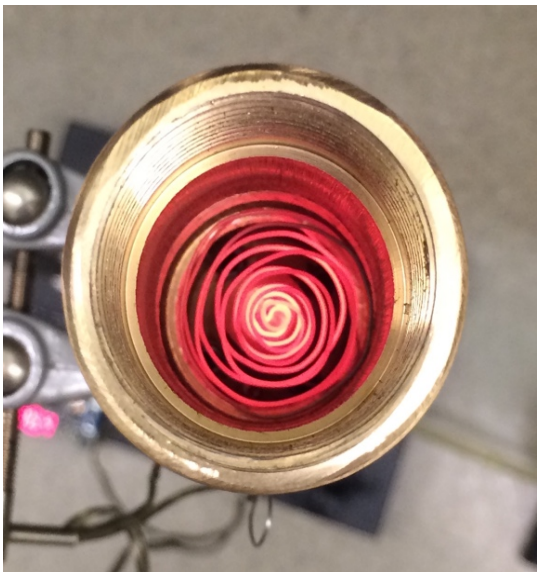

Figure 3.4: Combustion chamber with glowing ignition coil

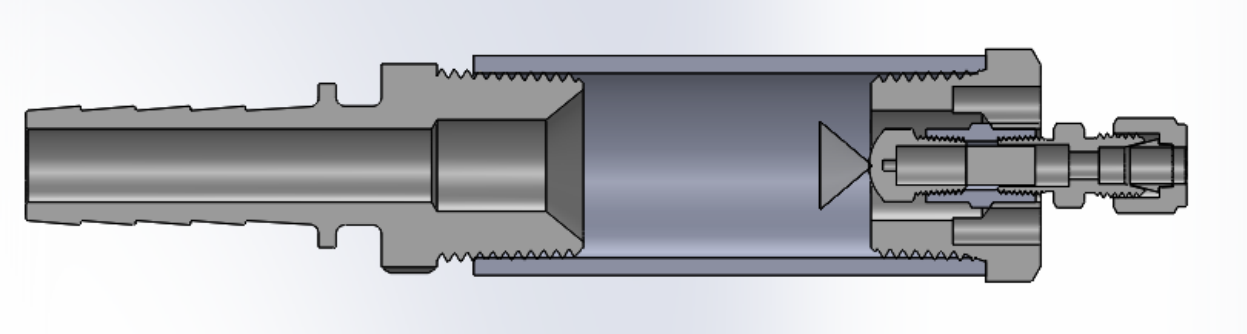

Figure 3.5: CAD Model of fog nozzle soot system

3.4.2 Electronic cigarette:

Direct vapor ignition with no wick still seemed to be an ideal option. Inspiration came from trying to find a system that could produce a fine mist or fog, but at a much lower flow rate. During this period of time, electronic cigarettes were a topic of conversation and they seemed to work well with liquid of similar material properties. A Nautilus Prime brand electronic cigarette head (machined tip, glass vile tank, and coil) as well an Evolv DNA 250 controller were purchased to build this system (Figure 3.6). The Evolv DNA 250 controller was a bare PCB for controlling a coil, specifically designed for research and data acquisition. The Escribe suite software, supplied with the Evolv DNA board allowed for ample fine tuning and datalogging of the Nautilus Prime and its coil.

Figure 3.6: Evolv DNA 250 controller and 2 cotton coils. Note: they are wrapped in heat shrink, (Left) and in high temperature tape (right) and then had smaller holes added as an attempt to reduce the flow rate.

The results from the revised chimney were greatly improved and a small controlled flame could be created sitting atop a vaporizer tank full of rapeseed oil. The samples started off very promising. Unfortunately, the capillary properties of the wick where not strong enough to counter the large drop in viscosity when the oil heated. Eventually, the oil was thin enough to flow through the wick faster than it was vaporized. The oil's surface tension would result in closing off the air passage to the flame. The system was flow controlled by the metered valve used for the original flow-controlled system. It would build up pressure and break through the film of oil that now blocked its passage. The oil would then flow back down and reform, again closing off the air passage, causing harmonic chugging of the system. This gave a very unstable burn, unsuitable for a fine tuned and controlled experiment.

3.4.3 Miniature oil boiler:

This system seemed close to a breakthrough but needed to overcome the previously identified problem with the coil and oil viscosity. Next a small sealed enclosure with a

stainless steel pipe at the top was manufactured. A small high temperature heater was placed in the base with some oil in it (see Figure 3.7). The oil was brought to a simmer and the fumes that came out of the stainless pipe were lit.

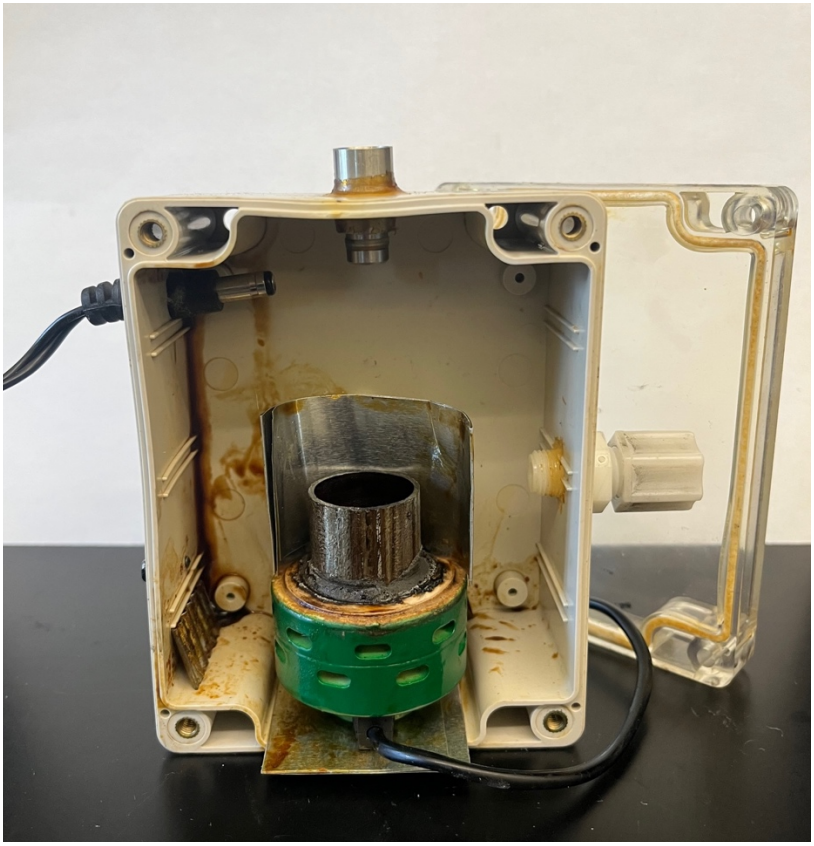

Figure 3.7: Small oil boiling vapor system. Electric charcoal with attached oil holding chamber.

This produced a small flame, which seemed suitable for testing, but the system did not hold much oil and did not last long. The next issue was that the system would sputter and spit oil. It was messy and introduced turbulence into the air which resulted in an inconsistent flame.

3.4.4 Oil boiled on hot plate:

The next approach was to use a beaker on a hot plate and light the fumes as they came out of the top. Argon was fed into the beaker using the same flow rate system used previously and oxygen was added into the system at the neck. This was to avoid the

chance that the flame would burn down inside the beaker and ignite the oil vapor all at once. This new, improved system seemed to have overcome most of the issues up to this point (see Figure 3.8).

However, in the end it suffered a new issue with a similar outcome previously experienced with the e-cigarette vaporizer system. Oil would condense on the walls of the pipe, and once enough had built up it would flow to the bottom of the pipe and periodically disrupt the flow of air out of the system.

After these experiences, it was apparent that the oil consumption had to be a controlled variable and not just a measured one. If not the system would become unstable.

To address this the oil flow rate was to be controlled with a motorized syringe with the additional goal of vaporizing and ignited the oil in very close proximity.

Figure 3.8: Large oil boiling system. Beaker with flow- controlled nitrogen into main chamber and oxygen at the neck.

3.5 Final design, Cutting torch with oil fed through core:

To accomplish these goals, a cutting torch was used as a starting point. These have a flame for heating and a center bore, which feeds oxygen to the system for the cutting process. This center oxygen core was replaced with a small stainless steel line,

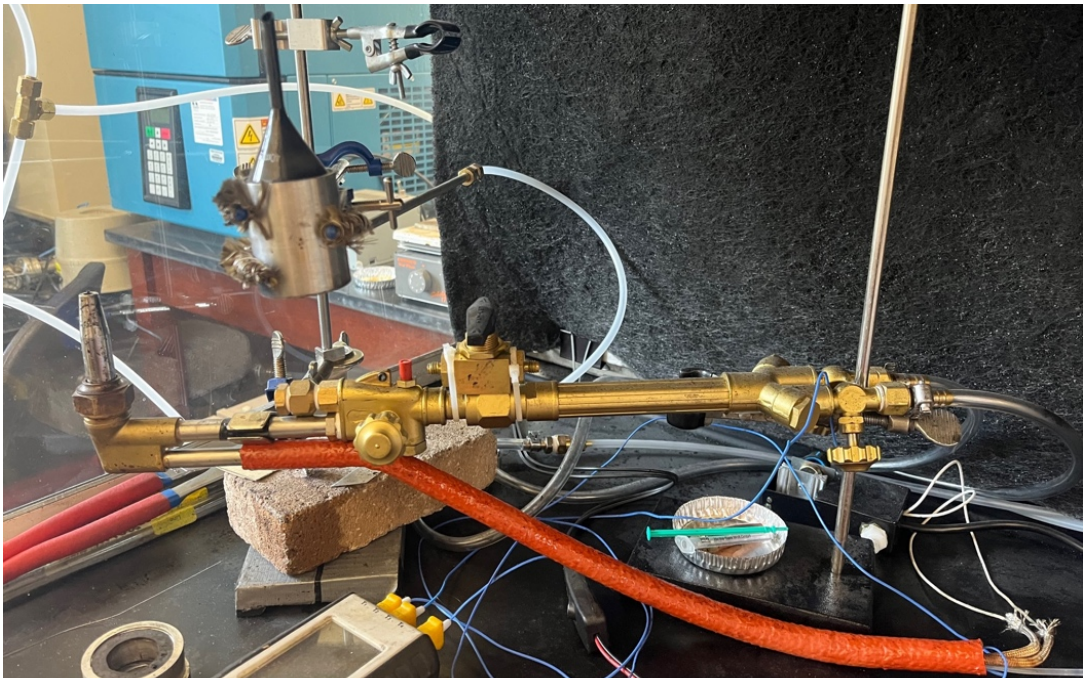

Figure 3.9: Modified cutting torch system. oil preheater inside fiberglass (orange). Controllable oxygen and argon for torch and combustion chamber.

connected by stiff plastic tubing, which was connected to the motorized syringe (see

Figures 3.9, 3.10, and 3.11). The plastic tubing was run inside an insulating fiberglass sleeve and was heated to keep the viscosity of the oil low and constant.

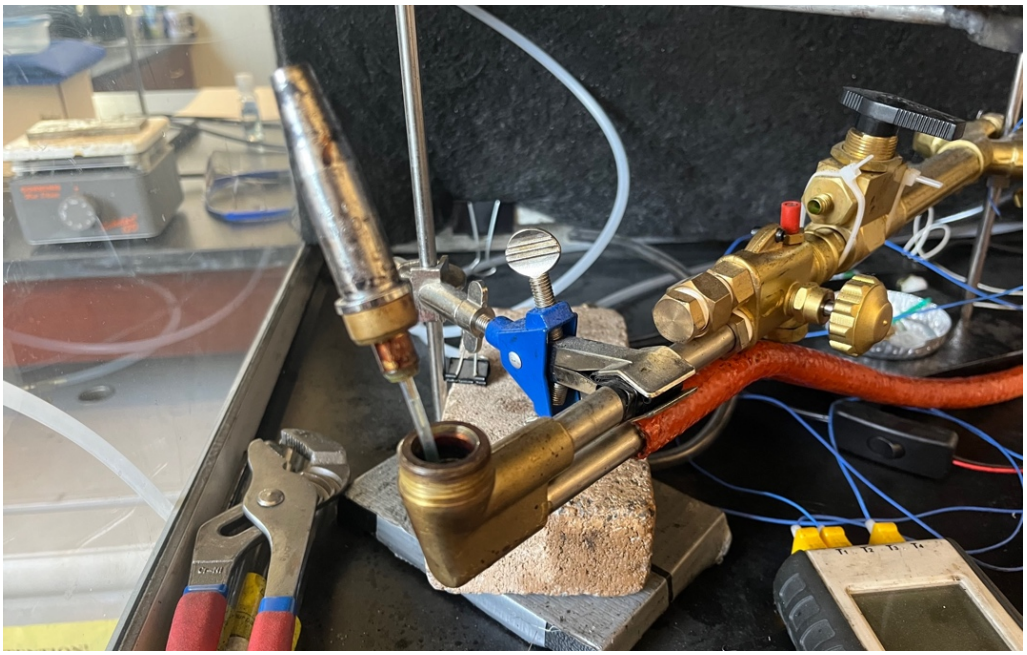

Figure 3.10: Oil line plumbed to center cutting hole of torch tip

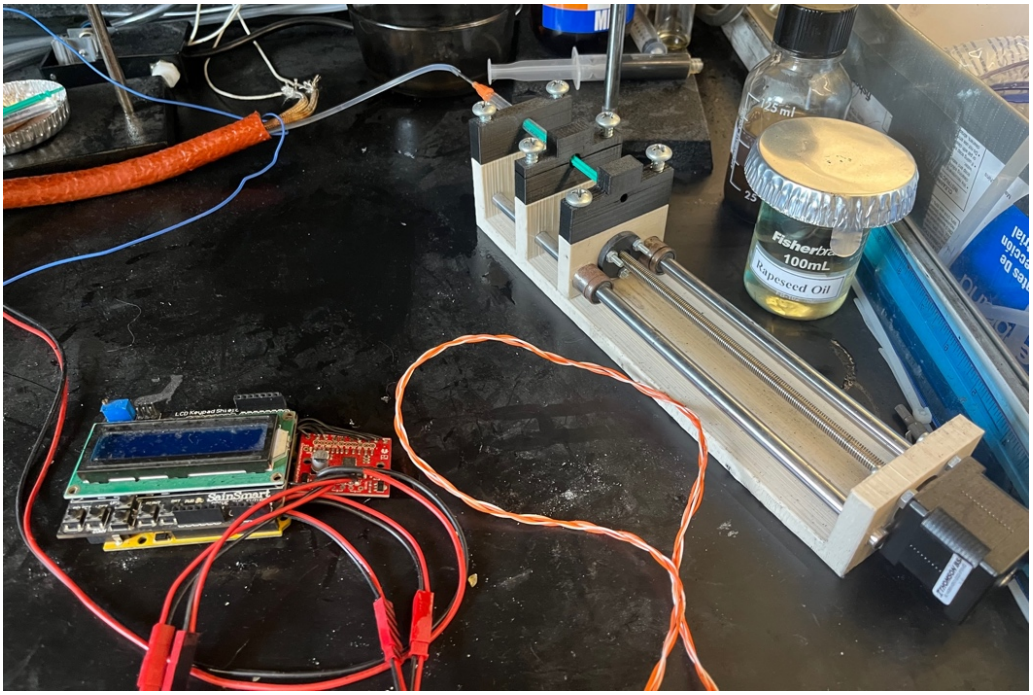

Figure 3.11: motorized syringe system for oil flow

First, the heating flame was turned on and adjusted. Oxygen and propane were turned on and the flowrates were set on the adjustable flow rate meters. It was found that these flowrate readings alone were not sufficiently repeatable. As the ratio of oxygen-to-propane increased, burning leaner, the system would start to emit an audible whine as it approached resonance with the flow out of the cutting torch. The flow rate meters were adjusted until it produced an E sharp sound, as measured by an electronic tuning device. Any note higher than E sharp was not stable; the gasses would reach a lean enough ratio and the flame would burn inside the torch tip and be extinguished. At this E sharp setting, the heating flame produced a very clean burn, which when checked for soot production left no residue on a glass slide. This is important as the heating flame combustion should not contribute to the soot on the sample, as this is an investigation of soot from rapeseed oil combustion.

After getting the propane-oxygen combustion to a stable and clean burn, it was allowed to thermally equalize for roughly five (5) minutes. This was enough time that the thermocouple, located throughout the system, saw less than 1-degree increase in 1 minute. The next step was to carefully set the flow rates of the argon and oxygen gasses, which were fed into a custom-made combustion chamber, which was placed over the cutting torch. This chamber consisted of a machined aluminum tube with a center bore that sealed on the torch tip and a lip that fit a glass funnel and was sealed with a sheet of high temp rubber (see Figure 3.12 and 3.13). The chamber was placed over the flame and allowed four (4) minutes to reach equilibrium. Its temperature was checked for equilibrium with an infrared (IR) laser thermometer.

Figure 3.12: Flame inside of the control chamber

Finally, it was time to make samples. The heated combustion chamber was lifted and the motorized syringe was set to feed oil at a constant volumetric flow rate. After a few seconds the oil would make it to the tip of the stainless steel tube and a small flame would be produced. (See Figure 3.13).

Figure 3.13: Oil vaporized and burned as it comes out of the center stainless steel tube. Note: preheated and ignited by flame from torch.

The chamber would then be lowered back over top of the torch tip and a stream of soot would start to emit from the top of the funnel. Samples could then be collected (see Figure 3.14).

Figure 3.14: System in use making a sample (i.e. glass slide cut to a 1-in length)

3.6 Data from collected samples:

The table below shows the conditions used for collecting samples. Duplicate samples were collected for each setting.

Table 3.1: Conditions of system for sample collection

Tuner reading	E-hi -18	
Coating height above funnel exit	5	mm
Propane	26.5	CCM
Oxygen Combustion	70	CCM
Oil Flow	0.003223727	ml/sec
Argon flow	1400	CCM
Oxygen environment	160 to 210	CCM

Table 3.2: Oxygen flow rates used to produce each sample

Sample	Flow	Units
1	159.6	CCM
2	161.31	CCM
3	165.3	CCM
4	166.44	CCM
5	171	CCM
6	176.7	CCM
7	182.4	CCM
8	188.1	CCM
9	193.8	CCM
10	199.5	CCM
11	205.2	CCM
12	210.9	CCM

3.7 Sample analysis, contact angle:

The samples were analyzed in two (2) ways. First, each was imaged under a Hitachi SU-70 FE-SEM taken at VCU's Nanomaterials Core Characterization Facility. It was found that a magnification of 50 thousand times was ideal to show the structure of the surfaces. Capturing images of some of the samples was quite difficult as the long chain linked structures would often move slightly during the exposure, causing them to blur. The surfaces also have a large degree of surface roughness, as expected, and it was difficult to focus on the entire field of view, as such a middle focal point was chosen. The images were captured with the samples 7 mm from the lens of the SEM, with a voltage of 15 kv. After the images were captured the sphere size of the chained soot was measured and averaged. To remove biases from these measurements the samples were shuffled and given random names. Eight (8) to ten (10) spheres were chosen on each image and the diameter of each sphere was measured by counting the number of pixels across its diameter. This was then correlated with the number of pixels in the scale of the SEM image.

The next major investigation was of the advancing/receding contact angle and hysteresis measurements using a Kruss DSA25E surface analyzer. The KRUSS software automatically sets a base line and finds the contour of the droplet (Figure 3.15) it uses these to calculate the tangent angle at the point of contact with the surface. However the software setting significantly impacted its ability to read a contact angle and it was critical to get the setting to a point which correctly represented a droplet on the surface. For our surface, the Kruss system had the following measurement specs:
Brightness: 30
Contrast: 85
Dynamic measurement using (Tangent/Ellipse)

See Figure. 3.15 below:

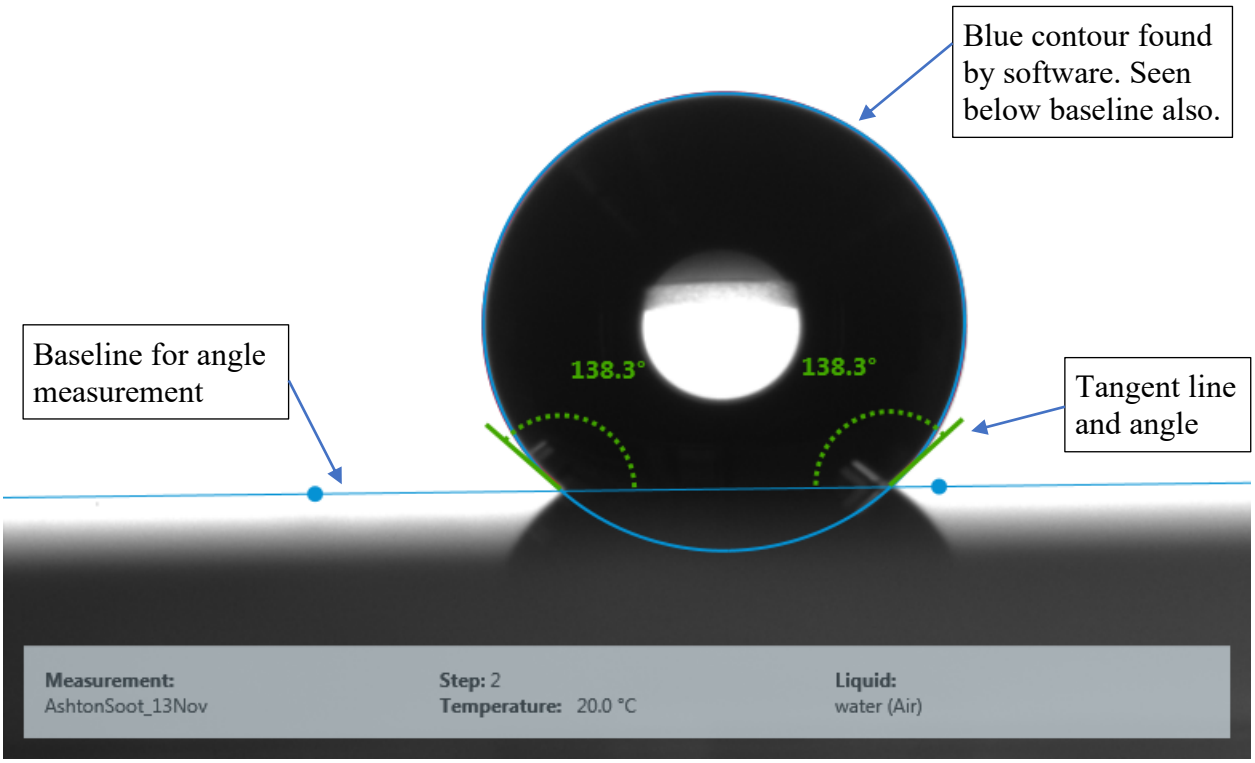

Figure 3.15: : Image of contact angle measurement screen. (Sample 2)

See Figure. 3.16 below:

Figure 3.16: KRUSS DSA25E drop shape measurement system

The syringe height was held constant for all samples at roughly 1.5 mm above the surface. Between sample collection the droplets were wicked away using a KIMTECH brand Kimwipe. Water was manually, and very slowly, dispensed until the first signs of water showed at the tip of the needle, when viewed through the KRUSS camera using its software. This was done because the Kimwipe could wick some fluid out of the

syringe tip, and it was important this did not impact the volume of the following sample. The KRUSS contact angle measurement software includes a profile creation section, which allows the user to create an automated dispensing and data collection profile. All samples were collected using a profile which automated the following steps. First, 7 uL of water was dispensed, just enough for the droplet to come into contact with the surface. Next, the software started to log the contact angle measurements while a loop ran; first dispensing then retracting 13.3 uL of water. This was enough volume of water such that a plateau could be seen in the measurements for both advancing and receding contact angles. The dispensing and retracting were done at a rate of 0.02 uL/min and a total of 200 sample measurements were collected. These recorded measurements include still images which are analyzed by the software as shown in Figure 3.15 and the resultant contact angle stored in a spreadsheet. This process was repeated for three (3) locations on the sample in roughly the shape of a triangle. Even with careful settings the KRUSS software often makes errors in its predictions. Therefore the frames were individually analyzed to set the baseline and check that the contours were correct.

When measuring the droplet profile, the contact angle is slightly higher when the droplet is small and slightly lower when the droplet is at its maximum size. This was due to the fact that measurements with larger droplets typically show slightly lower contact angles and the surface energy of the needle has a notable upward capillary force on the small droplet. Because of this, the droplet contact angles were calculated from an average of the measurements from 17-27 seconds (advancing) and in the same way from 55-65 seconds (receding). This gave enough time for the droplet to become fully developed as advancing or receding and not transitioning. Data points in these areas generally showed less than 1-degree of variation.

As was listed in Table 3.2, the contact angle data collected was for ambient oxygen flow rates ranging from 160 CCM to 210 CCM. Below a 160 CCM flowrate, the droplet always resulted in pinning and low contact angle. It was found that the oil would vaporize, but without sufficient oxygen to burn and with lower heat from lack of

combustion, the oil vapor would condense on the surface. These surfaces looked shiny and the oil would smear when being cleaned. Above 210 CCM, the surface coating became unstable, in which case the droplet would peel the soot off of the glass. Previously in the VCU lab we found that open flame carbon soot had these same poor properties.

3.8 Combustion Equation:

When investigating the combustion process it was found that the combustion was very rich. Assuming that all of the propane is consumed then it needs to react at roughly 5:1 oxygen to propane.

$$C_3H_8 + 5O_2 \rightarrow 3CO_2 + 4H_2O$$

At a flow rate of 26.5 CCM it would need to consume 132.5 CCM of oxygen. Of this 70 CCM is provided by the flow to the cutting torch and 62.5 CCM consumed from the environmental oxygen flow.

Take for example an oxygen flow rate of 176.7 CCM (sample 6). This would leave 114.2 CCM environmental oxygen remaining to combust the vaporized rapeseed oil. The oil flow rate is 0.003224 ml/sec or 0.1934 ml/min. Rapeseed oil is primarily oleic acid ($C_{18}H_{34}O_2$) and linoleic acid ($C_{18}H_{32}O_2$). For simplicity rapeseed oil was calculated as if it were all oleic acid.

For oleic acid the combustion equation is as follows

$$C_{18}H_{34} + 26O_2 \rightarrow 18CO_2 + 17H_2O$$

Meaning for a stochiometric burn 26 : 1 moles of oxygen to moles of oleic acid were needed.

Our lab is at 22-degree Celsius and an ideal gas will have 24200 cc/mol. Our available oxygen flow rate of 114.2 CCM equates to 0.00472 mol/min of Oxygen.

Oleic acid has a density of 0.895 g/mL at 0.1934 ml/min is 0.1731g/min.

A molar mass of 282.468 g/mol gives a rate of 0.000613 mol/min.

$$\frac{0.00472 \text{ mol/min of oxygen}}{0.000613 \text{ mol/min of oleic acid}}$$

gives a molar ratio of roughly 7.7 : 1 oxygen to oleic acid.
This is only 30% of the stochiometric combustion ratio of 26 : 1.

It is impossible to know just how much combustion was being completed without a proper combustion analyzer but at such a rich ratio it is likely most of the oxygen is consumed.
At our lowest flow rate there is 97.1 CCM of environmental oxygen remining, giving an oxygen fuel ratio of 6.55 : 1.
For our highest flowrate 148.4 CCM of environmental oxygen remining giving an oxygen fuel ratio of 10:1

Chapter 4 Results and Discussion

There are two (2) important factors when considering the results from a contact angle measurement test. The first is the values of the contact angles themselves and the second is the hysteresis, which is the difference between the advancing and receding contact angle.

4.1 SEM Images:

Figure 4.13 shows a plot of the advancing and receding contact angle as well as the average sphere size for each sample. Next please look over Figures 4.1- 4.12. These are the SEM images of the samples in order of increasing oxygen. First, looking at Figures 4.1- 4.4, there is a clear transition from rough shaped pillars to spherical connected chains of soot. Looking over Figures 4.4 - 4.12, there is a general decrease in sphere diameter with an increase in oxygen flow.

The peak of the advancing contact angle was at a flow rate of 171.0 CCM, a peak of the receding contact angle in the next sample was at 176.7 CCM and a minimum hysteresis

was in the following sample at 182.4 CCM. In general, there was a decrease in advancing angle following further increase in flow above 171.0 CCM; however, there is a notable dip in advancing contact angle at 182.4 CCM. Lending to its lower hysteresis. Above 176.7 CCM there is an overall decrease in receding contact angle, but the downward trend is slightly noisy (i.e., data points showing more scatter).
There also is a continuous decreasing trend in sphere diameter with an increase in oxygen flow, including the feature size seen at the transition from pillar like structures to a chain of spheres.

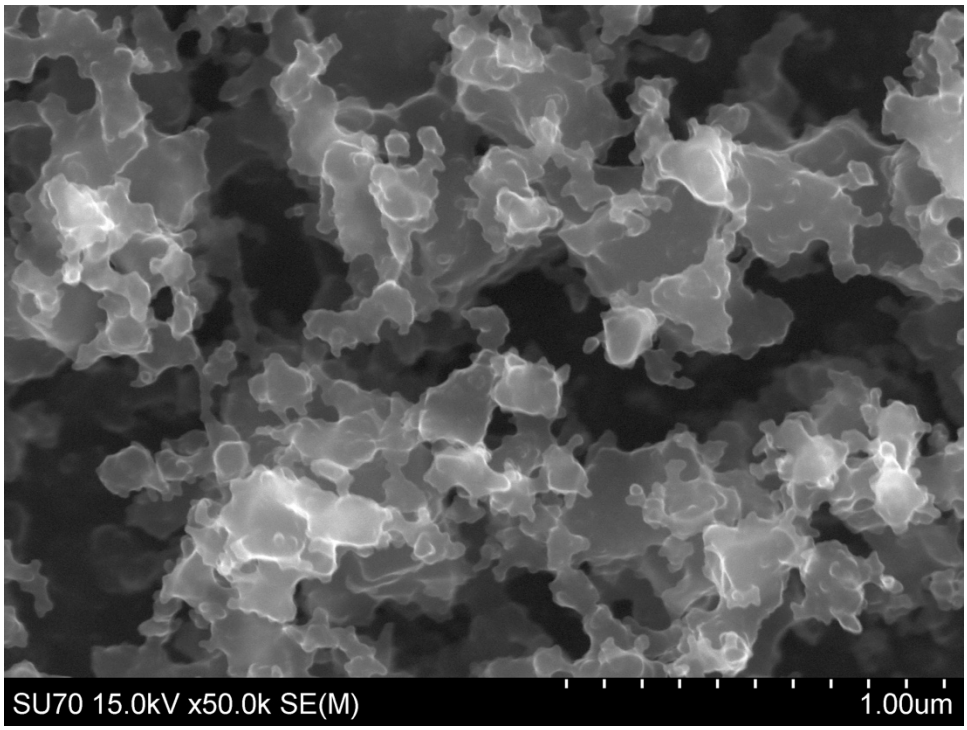

Figure 4.1: Oxygen Flow Rate: 159.6 CCM; Advancing: 162.5 degree, Receding: NA, Hysteresis: NA

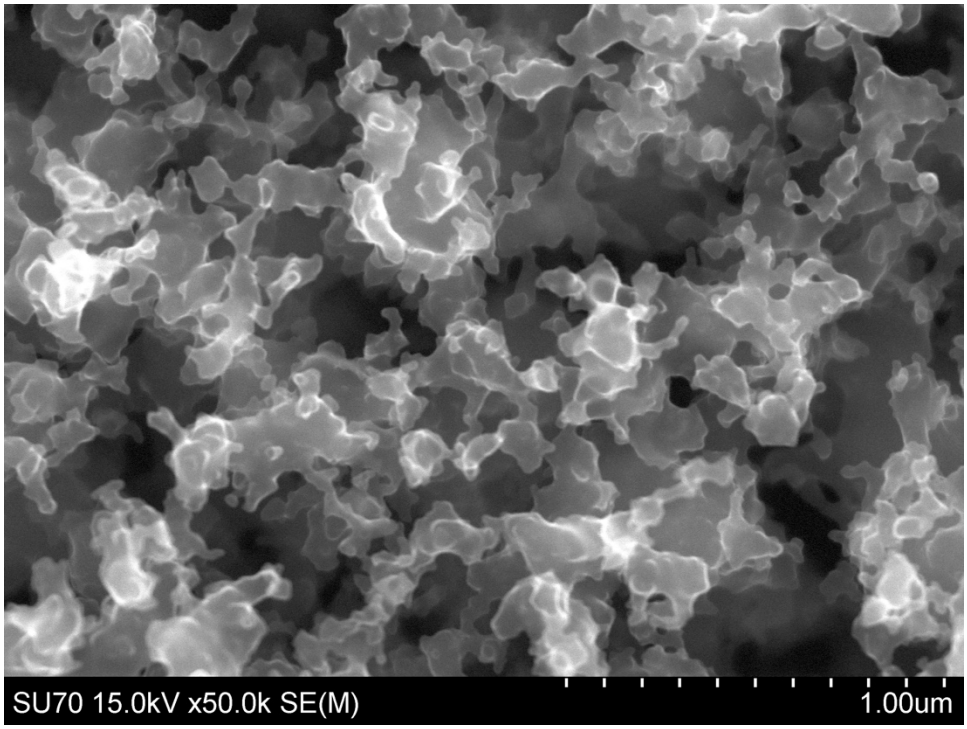

Figure 4.2:Oxygen Flow Rate: 161.3 CCM; Advancing: 154.1 degree, Receding: NA, Hysteresis: NA

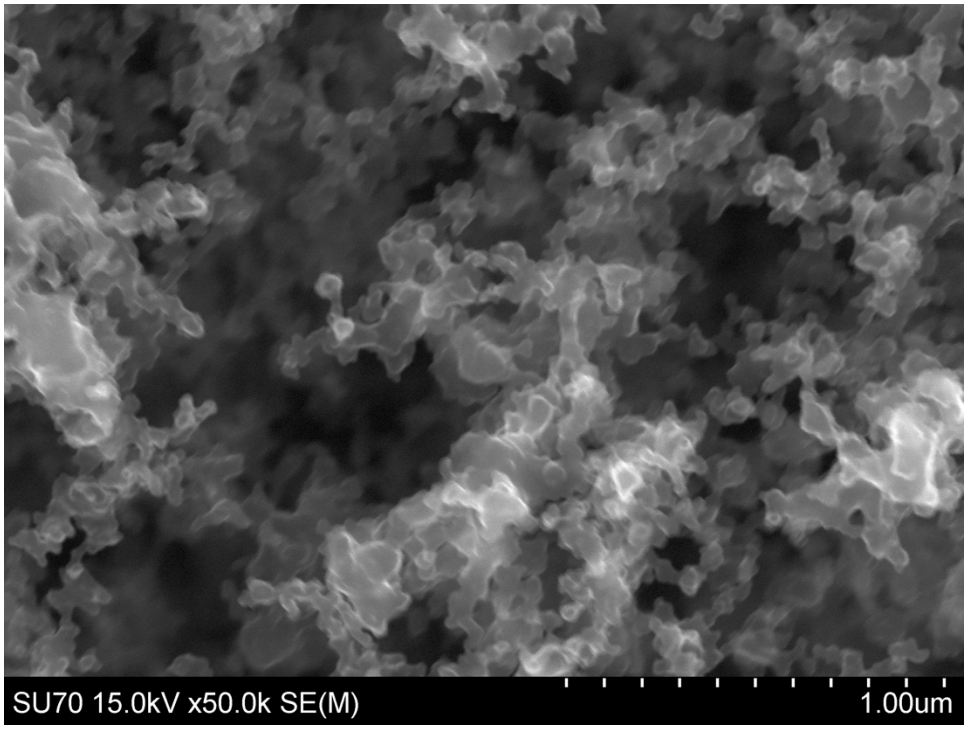

Figure 4.3: Oxygen Flow Rate: 165.3 CCM; Advancing: 158.4 degree, Receding: 126.7, Hysteresis: 31.6

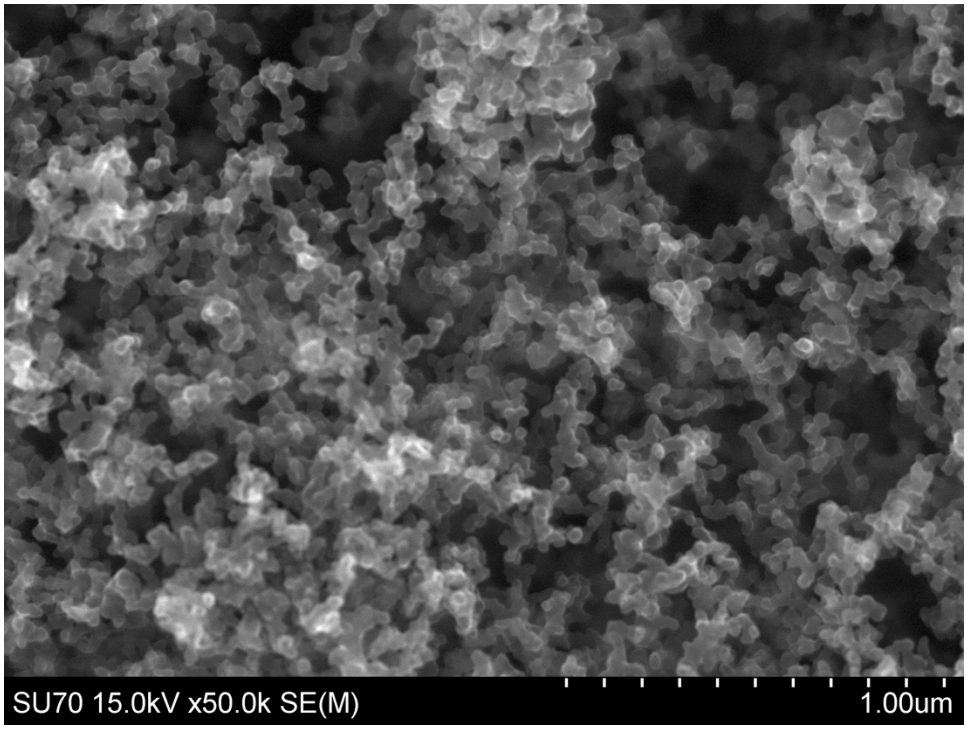

Figure 4.4:Oxygen Flow Rate: 166.4 CCM; Advancing: 167.9 degree, Receding: 157.1, Hysteresis: 10.8

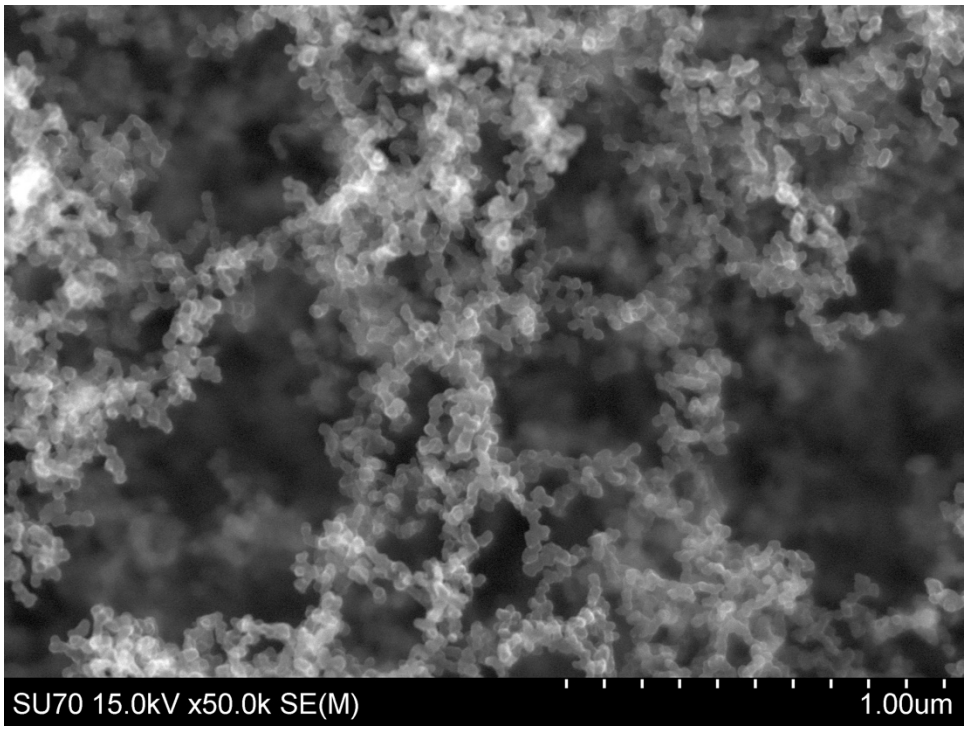

Figure 4.5: Oxygen Flow Rate: 171.0 CCM; Advancing: 170.0 degree, Receding: 156.5, Hysteresis: 13.6

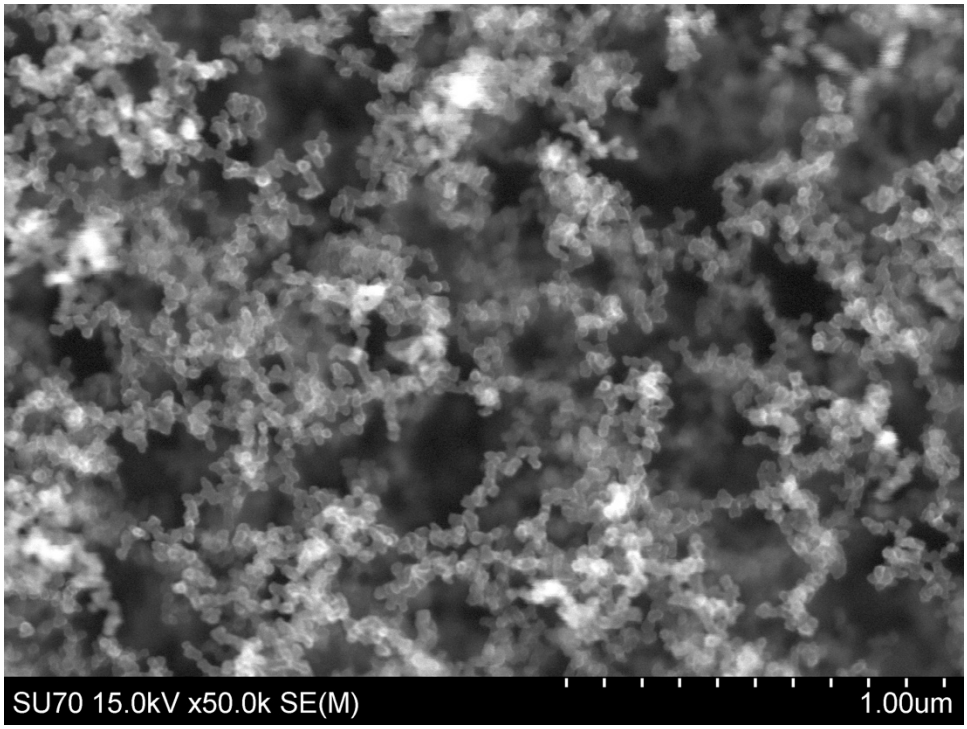

Figure 4.6: Oxygen Flow Rate: 176.7 CCM; Advancing: 169.2 degree, Receding: 159.9, Hysteresis: 9.3

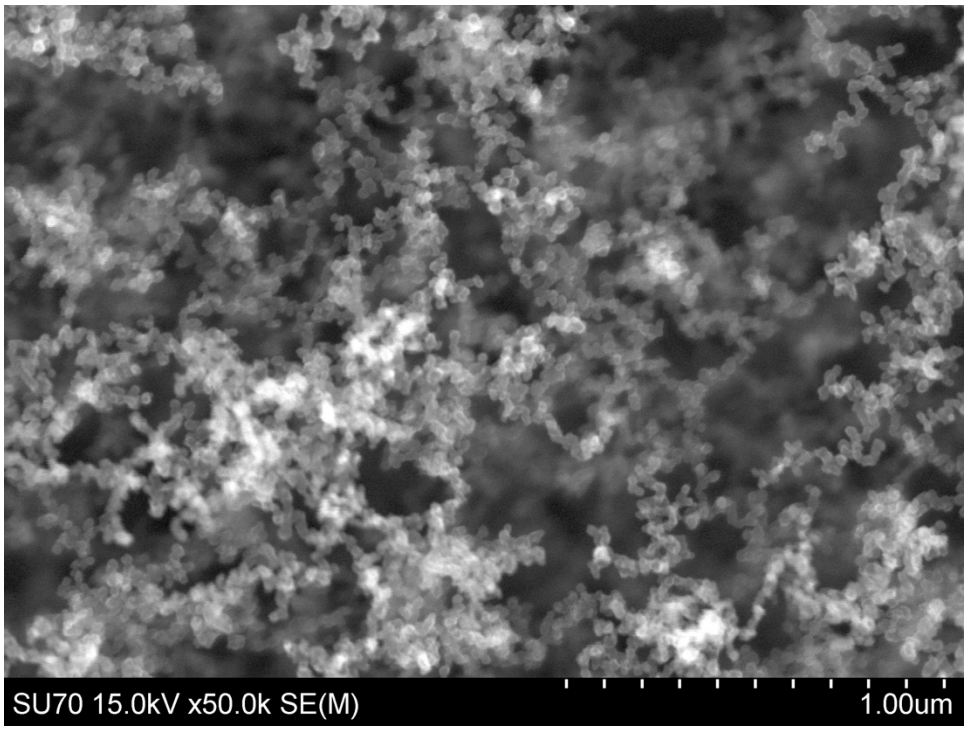

Figure 4.7: Oxygen Flow Rate: 182.4 CCM; Advancing: 158.7 degree, Receding: 152.9, Hysteresis: 5.85

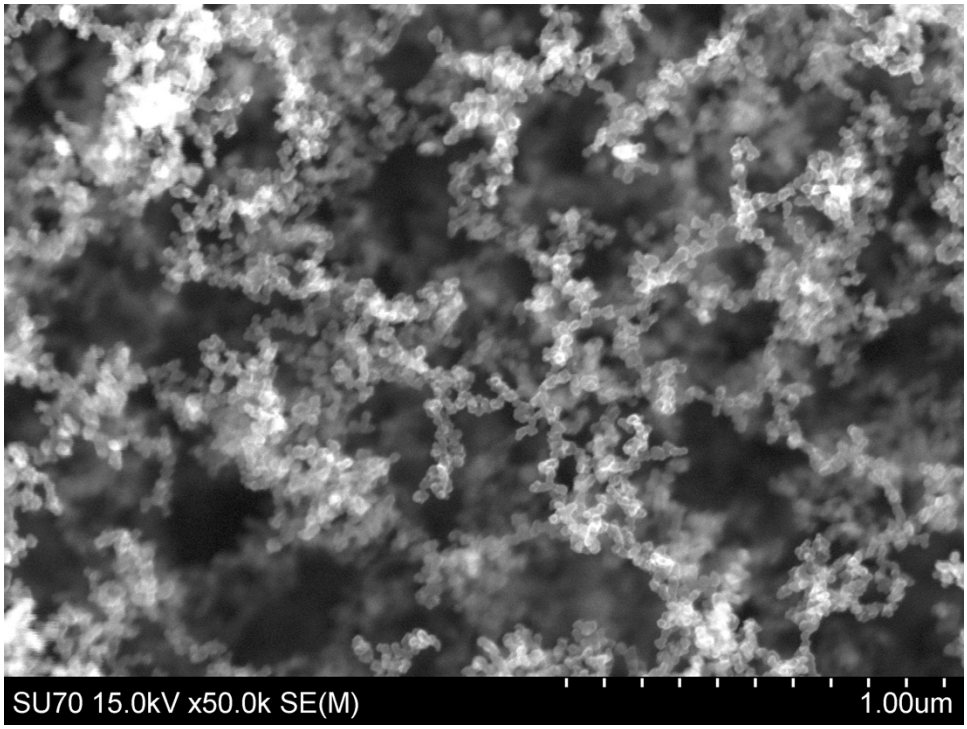

Figure 4.8: Oxygen Flow Rate: 188.1 CCM; Advancing: 167.4 degree, Receding: 156.9, Hysteresis: 10.4

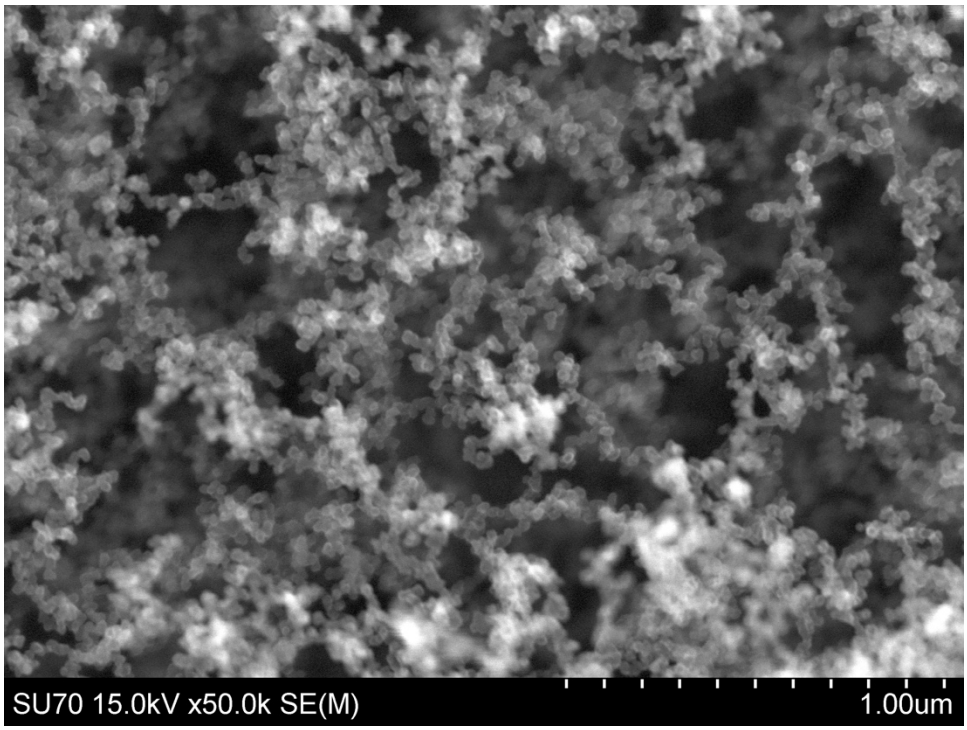

Figure 4.9: Oxygen Flow Rate: 193.8 CCM; Advancing: 166.4 degree, Receding: 149.0, Hysteresis: 17.3

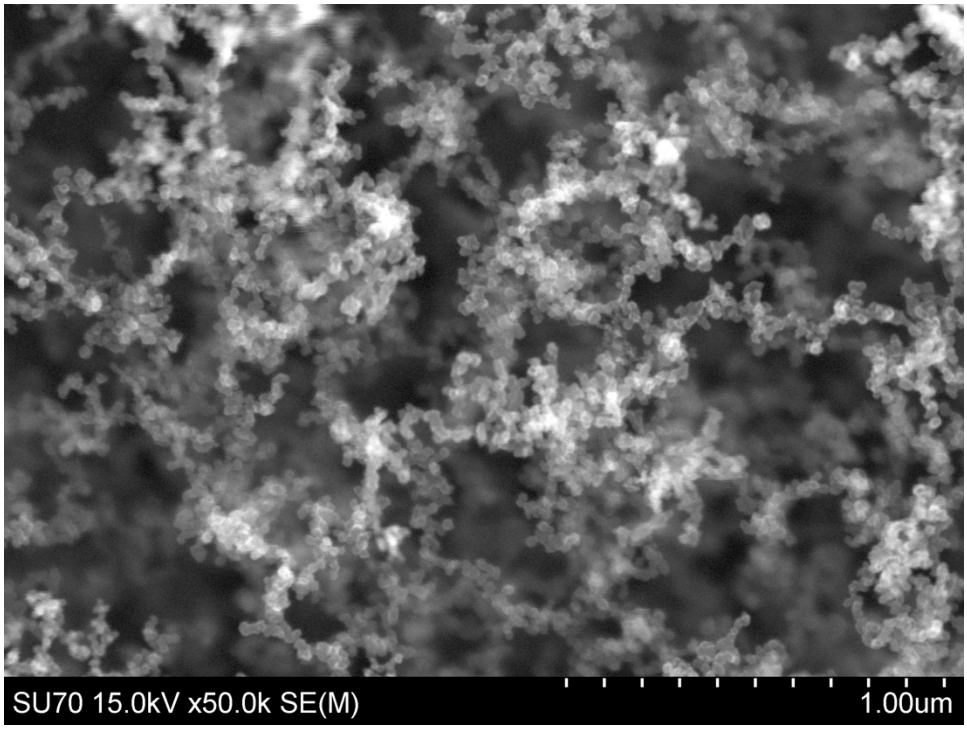

Figure 4.10: Oxygen Flow Rate: 199.5 CCM; Advancing: 162.3 degree, Receding: 150.4, Hysteresis: 11.9

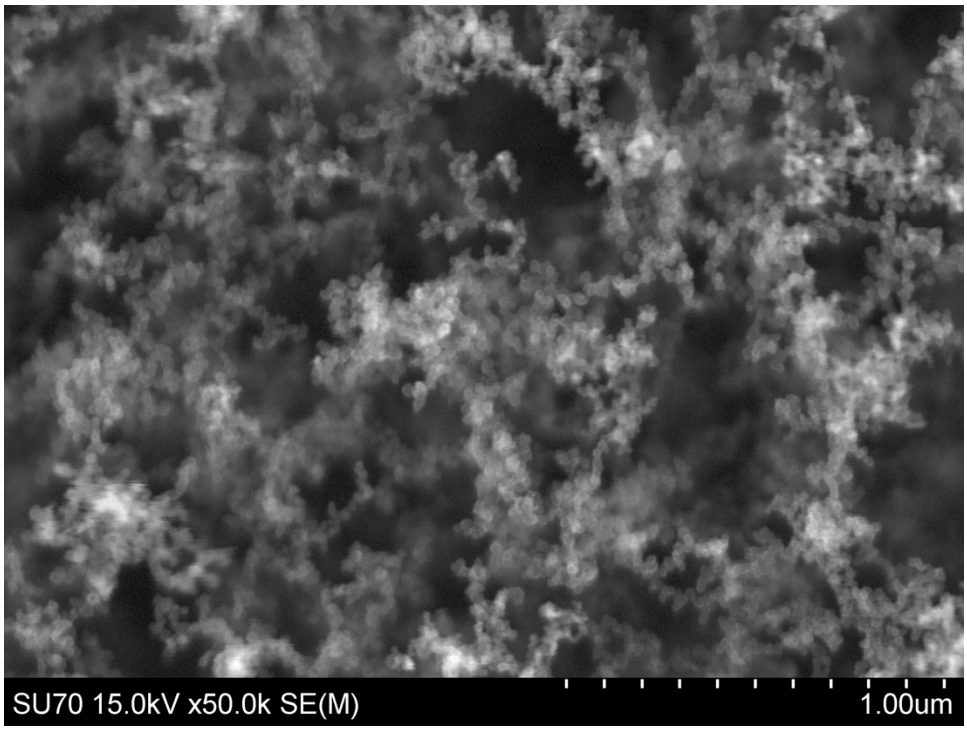

Figure 4.11: Oxygen Flow Rate: 205.2 CCM; Advancing: 161.1 degree, Receding: NA, Hysteresis: NA

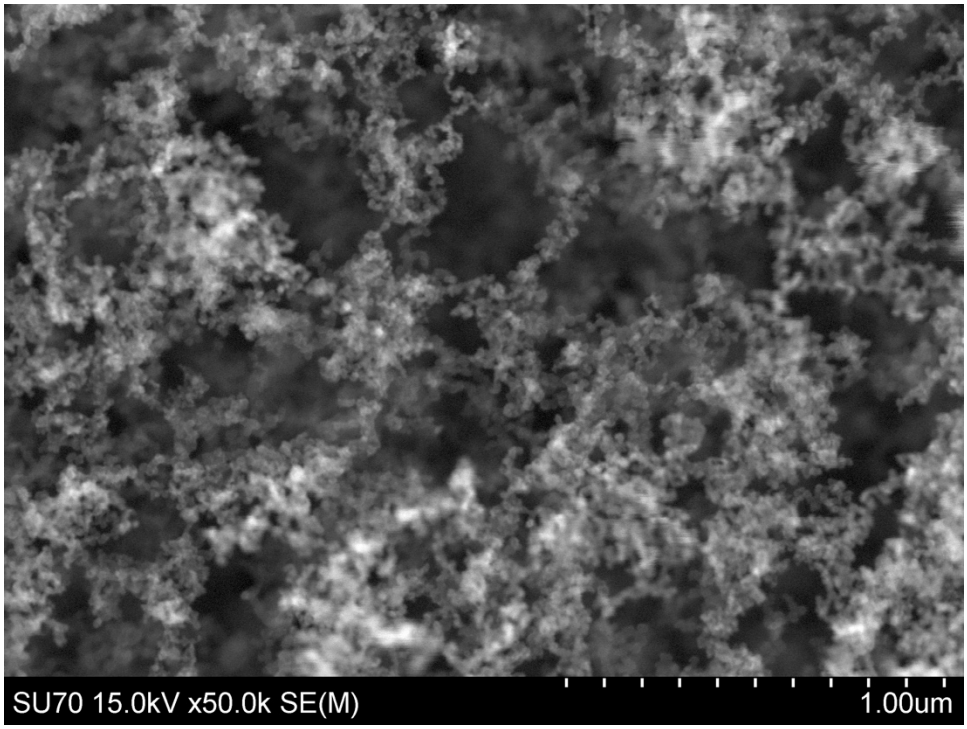

Figure 4.12: Oxygen Flow Rate: 210.9 CCM; Advancing: 152.6 degree, Receding: NA, Hysteresis: NA

4.2 Comparison of combustion, contact angle and sphere size:

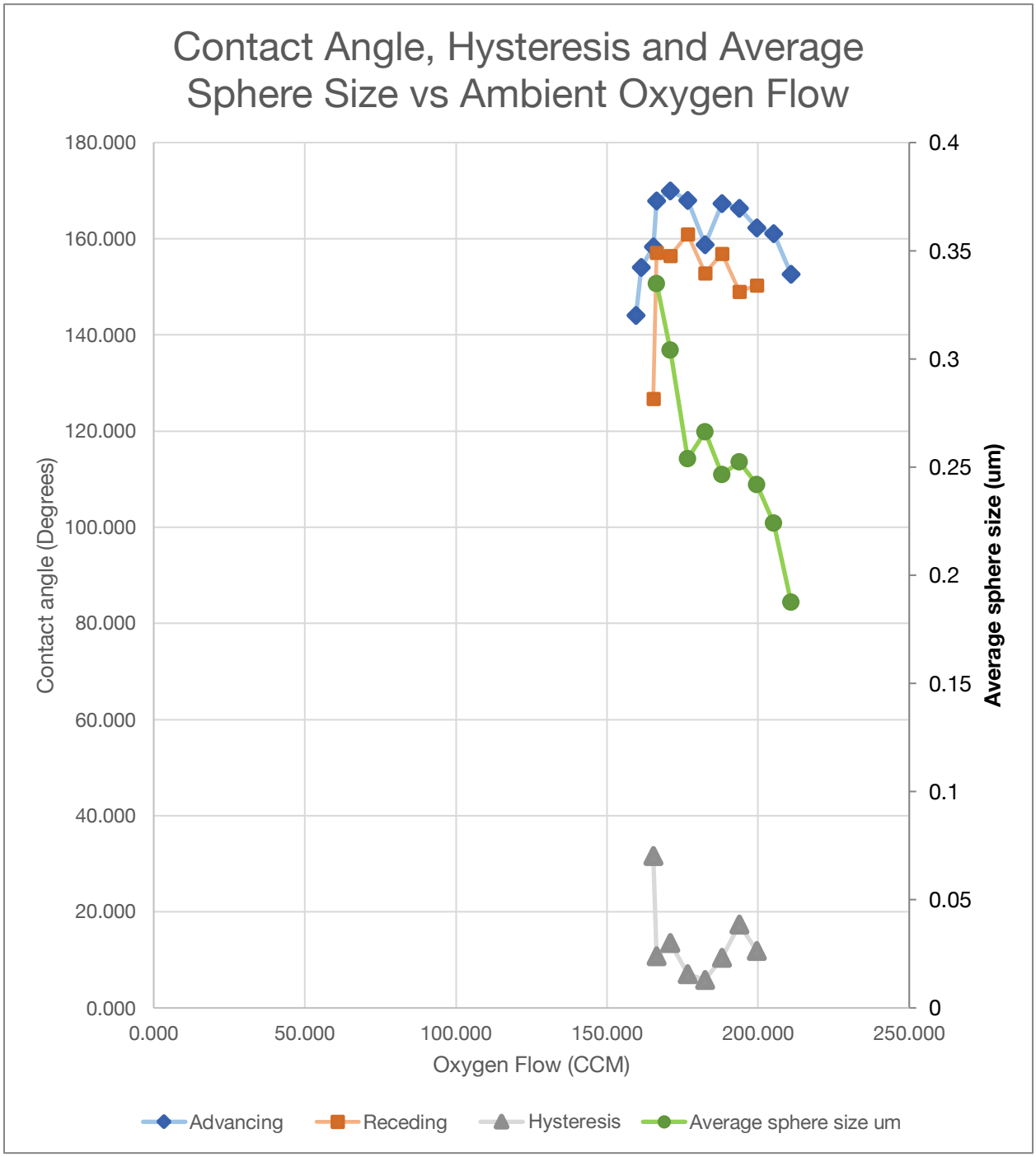

Figure 4.13: Hysteresis, Advancing contact angle, Receding contact angle and average sphere size vs. Oxygen flow rate

This decrease in sphere size gets into an important part of surface science, not only the degree of roughness but the size of the roughness can have a significant impact on contact angle, because of the triple-phase (solid-liquid-gas) intersection lines that exist in the Cassie-Baxter state [22], [31], [32]. Typically, the triple-phase intersection lines would have little impact on the hydrophobics but when the surface features are on the micro or smaller scale the triple-phase line length can be extremely long. For example, given a square top pillar grid pattern, with side length and spacing of 1 μm, there is a triple-phase line length 3 orders of magnitude greater than the contact area.

It was found by ZHENG that for a given material, there was a critical length (l_{cr}), which was easy to observe experimentally; with the reduction in surface feature size (i.e. roughness scale), the contact angle increases as in surface feature size approached l_{cr}. [26] Having features closer to this critical length resulted in an increase in contact angle. In the case of ZHENG they had a silicon wafer etched using photolithography and grafted with a self-assembled monolayer of octadecyl trichlorosilane (OTS, C18H37Cl3Si, 95%). The critical length was found to be 0.29 μm. For a given pillar its shape-dependent roughness scale (S) was found as the cross-sectional area (A), divided by the perimeter length (L). Written as S = A/L. From the relationship below, as S approaches l_{cr}, $cos\theta^*$ approaches -1, which correlates with a contact angle of 180 degrees.". Mathematically, ZHENG discovered the following relationship:

$$cos\theta^* = -1 + (1 + cos\theta) * \left(1 - \frac{l_{cr}}{S}\right) f \tag{8}$$

Consider a chain of spheres and imagine the theoretical situation where the Liquid-Gas boundary has made it halfway around the sphere (i.e. the sphere chain is halfway submerged into the surface of the water). Then the cross-sectional area (A) for a sphere is $2\pi r^2$ and the perimeter (L) is $2\pi r$. Plugging in for A and L into S=A/L gives S = r. Our experiments showed a radius of about 0.14 μm was the most hydrophobic. Theoretically, if S is smaller than l_{cr} this would corollate with negative energy released from placing a droplet on the surface. Values of S that go below l_{cr} would always result

in a contact angle of 180 degrees. However, experimentally, when S is less than l_{cr}, the contact angle decreases.
One leading theory is that at such small length scales there is a very small gap between the surface features and the droplet [33-35]. With only hundreds of nanometers separating the droplet and surface feature, long range interaction forces could pull the droplet to the nearby surface.

An increase in oxygen flow rate leads to a smaller particle sizes with less structural integrity. It seems likely that the long-range interaction forces at play lead to the decrease in contact angle observed in our samples. Further work could be done to try and simulate the structural properties of our chained sphere surface and the dynamics of the system as a droplet is placed on the surface.

Chapter 5 Conclusions

Our tuned soot is able to utilize all the important fundamental aspects of surface science for creating functional superhydrophobic surfaces:

1) The surface is made from a relatively strong material. Carbon bonding, especially the DLC bonds found in our modified soot, are very strong. This is critically important because the required surface geometry would fail without this strength.
2) A submicron feature size that benefits from the triple-phase line energy. This aspect of is critical because is counters the higher surface energy of stronger material. Amazingly, utilizing the triple line energy can give superhydrophoibic properties to a surface even when it has a Young's contact angle slightly below 90 degrees.
3) Roughness: This was the first aspect covered in this thesis. It is well documented that when it comes to superhydrophobics the surface must stay in the Cassie-Baxter state and, as mentioned, the features must be the right size to utilize the

triple-phase line energy. This means that roughness applies to increasing the amount of wetted surface at each point that is in contact with the liquid. This is easily accomplished by having features which are convexly shaped instead of being flat. A chain of linked spheres does this well.

4) The surface needs to have as few points as possible in contact with the droplet. The anti-wetting properties are best when the droplet is suspended. The soot surface does this beautifully. The surface grows with an inter-laced structure of sub-micron sphere chains. It also has an ever-changing height to the surface, with lows and highs, peaks and valleys. The chains can deform allowing for additional load distribution while minimizing contact from a receding surface.
5) The surface is also thick relative to the surface structure. Many superhydrophobic surfaces that are published have features which are very close to the substrate or are tall and slender, which results in them being weak and likely to fail under many conditions. The thickness of our surface prevents the droplet from reaching the substrate and therefore stays in the Cassie-Baxter state but also is very strong compared to pillars.

A functional superhydrophobic surface will be made from a strong material and have a geometry which allows for enough depth to resist penetration and is mechanically strong and tough. Counterintuitively, an ideal material would have a relatively low contact angle when smooth. It will get its superhydrophobic properties from features mentioned above. Having only a few small points of contact often correlates with a surface which is structurally weak or will easily pierce the water. This can be countered by having interconnected surface features that support each other, as well as a surface with slight flexibility and increasing points of contact with depth into the surface. Slight flexibility can have functional advantages because it distributes the load, decreases the pressure at each point preventing penetration, but allowing the surface to return to a state where a droplet would have fewer points of contact. This is conceptually advantageous for droplet impact where the pressure spikes initially and then decreases.

This can also apply to roll-off, where there is slightly less pressure on the receding edge.

Continuing this discussion of an ideal material, the surface needs to be thick and inherently open cell, so that fluid can move easily without filling voids which can result in pinning. The surface thickness compared to the feature size must be enough to prevent penetration to the substrate which could result from impact or pressure. It requires a lot of energy to force a droplet into our surface. As such, the surface acts like a reverse sponge; a valuable feature to a functional surface. This keeps the system in the Cassie-Baxter state, which is ideal for roll-off and has many energetic advantages to reducing contact angle. Another critical attribute for an ideal superhydrophobic material, is that the surface has a decreasing roughness from penetration, meaning that as the droplet makes its way into the surface it contacts more and more points, distributing the load, and increasing the resistance to more penetration. This helps with stability from impact, submersion or other external forces.

The tuned soot surfaces created in the VCU lab were capable of meeting a number of these criteria at an impressively low cost. By creating a highly controlled combustion and precisely varying the flow of oxygen to the combustion chamber the sphere size could be controlled. The very best surfaces have a sphere size around 0.25 μm to 0.30 μm. Decreasing oxygen flow rates resulted in larger sphere sizes, which had shorter and more rigid connections. Increasing oxygen flow rates resulted in very long chains of smaller spheres sizes, which could be observed to move easily under SEM.

There are logical reasons to believe the long-range interaction forces resulted in the reduced hydrophobicity from the smaller sphere size. The surface created in the VCU lab is made up of chains. If the long-range interaction forces in these chains are strong enough to attract one sphere, then the next sphere down the line will get pulled closer to the water. In addition, the long, thin chains were less rigid and less able to resist these forces. These factors would compound, resulting in a larger increase in surface contact, reducing the contact angle and increasing the hysteresis.

However, the reduced rigidity sometimes proved helpful. When a droplet is placed on the surface, the soot chains deform. This deformation technically increases the number

of contact points. However, more contact points mean less pressure at each point and therefore less penetration around each point of contact. With each point being spherical, less penetration means less contact area, thereby counteracting the increased number of points with less area per point. With a sphere radius of 0.15 μm our surface had the most functional balance between, reduced hydrophobicity due to deformation from long-range interaction forces, but an increase in hydrophobicity from the increased triple-phase line length from more and smaller surface features. This line length is increased under pressure, as the surface deforms more and more of the spheres come into contact with the water's surface and the total length of the triple-phase line increases.

The investigation of these impressive properties of tuned soot surfaces at the VCU lab gives great insight into the fundamentals and ideals for designing a superhydrophobic surface. They take advantage of every aspect of energy balance which makes a surface fear water and they do it extremely well over a wide range of conditions. The sphere chains result in a great degree of roughness as a droplet penetrates into the surface, more so than pillars. The chains can deform slightly allowing for a huge number of very small contact points with a very long triple-phase length, making it extremely energetically favorable for the droplet not to contact the surface. And the surface has a very small area fraction of Solid-Liquid contact under a wide range of conditions. With such an energetic desire not to touch the surface and the structural ability to deform and return in shape, a minimal area fraction of contact is maintained for the given condition. With penetration into the surface being extremely unfavorable due to the compounded energy consumed due to the roughness and an increase in triple line length from additional contact points.

This is particularly advantageous in dynamic systems where any change in force or pressure will be minimized for the current state of the system. These are an incredible group of properties to have from a surface and further understanding and investigation could lead to the manufacturing of much more functional surfaces. The surfaces developed at the VCU lab accomplishes many of these attributes, while being strong due to the DLC bounding and the interconnected geometry which supports against forces in all directions.

Chapter 6 Potential Further Research

There are many more experiments which could be done to better understand all elements at play with superhydrophobic surfaces. More controlled experiments could look into surfaces of different geometries and different levels of rigidity. Experiments could also be performed that control the rate of change of contact points as a function of surface depth.

Another interesting thought experiment comes from thinking about how as pressure increases and more of the droplet is engulfed in water the shape-dependent roughness scale (S) becomes larger relative to the initial particle size. This implies that a small spherical surface structure may handle higher pressure better than the surface structure size tuned for just a droplet resting on the surface.

Additionally, creating smooth surfaces made of soot to get a base line Young's contact could prove insightful or characterizing these surfaces well enough to compare them to existing published data. Furthermore, experiments could be conducted for a number of known surface energies to find how surface energies impact the critical length based on triple-phase line energy.

Additionally, many of these investigations seem well suited for further study via computer simulation, in which ideal surface attributes could be determined for a wide range of subjected wetting conditions.

I found this research extremely insightful with respect to the science of surface wetting, nano structures and combustion, giving me new wisdom and a more open mind to all that should be considered when problem solving a wetting situation.

Thank you,
Ashton Bressler.

Chapter 7 References

[1] S. Wang and L. Jiang, “Definition of Superhydrophobic States,” in *Advanced materials*, Nov. 2007, pp. 3423–3424. doi: 10.1002/adma.200700934.

[2] B. Bhushan, Y. C. Jung, and K. Koch, “Self-Cleaning Efficiency of Artificial Superhydrophobic Surfaces,” *Langmuir*, vol. 25, no. 5, pp. 3240–3248, Mar. 2009, doi: 10.1021/la803860d.

[3] Y. Hu, S. Huang, S. Liu, and W. Pan, “A corrosion-resistance superhydrophobic TiO2 film,” *Appl. Surf. Sci.*, vol. 258, no. 19, pp. 7460–7464, Jul. 2012, doi: 10.1016/j.apsusc.2012.04.061.

[4] L. Hui, M. Liu, Y. Cai, and Y. Lv, “Fouling Resistance on Chemically Etched Hydrophobic Surfaces in Nucleate Pool Boiling,” *Chem. Eng. Technol.*, vol. 38, no. 3, pp. 416–422, 2015, doi: 10.1002/ceat.201400194.

[5] M. Nosonovsky and V. Hejazi, “Why Superhydrophobic Surfaces Are Not Always Icephobic,” *ACS Nano*, vol. 6, no. 10, pp. 8488–8491, Oct. 2012, doi: 10.1021/nn302138r.

[6] K. D. Esmeryan, A. H. Bressler, C. E. Castano, C. P. Fergusson, and R. Mohammadi, “Rational strategy for the atmospheric icing prevention based on chemically functionalized carbon soot coatings,” *Appl. Surf. Sci.*, vol. 390, pp. 452–460, Dec. 2016, doi: 10.1016/j.apsusc.2016.08.101.

[7] E. C. Stancu, M. D. Ionita, S. Vizireanu, A. M. Stanciuc, L. Moldovan, and G. Dinescu, “Wettability properties of carbon nanowalls layers deposited by a radiofrequency plasma beam discharge,” *Mater. Sci. Eng. B*, vol. 169, no. 1, pp. 119–122, May 2010, doi: 10.1016/j.mseb.2010.01.062.

[8] S. Zhang *et al.*, “Underwater Drag-Reducing Effect of Superhydrophobic Submarine Model,” *Langmuir*, vol. 31, no. 1, pp. 587–593, Jan. 2015, doi: 10.1021/la504451k.

[9] C. Cai *et al.*, “Superhydrophobic surface fabricated by spraying hydrophobic R974 nanoparticles and the drag reduction in water,” *Surf. Coat. Technol.*, vol. 307, pp. 366–373, Dec. 2016, doi: 10.1016/j.surfcoat.2016.09.009.

[10] J. Huang, S. Lyu, F. Fu, H. Chang, and S. Wang, “Preparation of superhydrophobic coating with excellent abrasion resistance and durability using nanofibrillated cellulose,” *RSC Adv.*, vol. 6, no. 108, pp. 106194–106200, 2016, doi: 10.1039/C6RA23447J.

[11] R. Karmouch and G. G. Ross, “Superhydrophobic wind turbine blade surfaces obtained by a simple deposition of silica nanoparticles embedded in epoxy,” *Appl. Surf. Sci.*, vol. 257, no. 3, pp. 665–669, Nov. 2010, doi: 10.1016/j.apsusc.2010.07.041.

[12] H.-M. Kim, S. Sohn, and J. S. Ahn, “Transparent and super-hydrophobic properties of PTFE films coated on glass substrate using RF-magnetron sputtering and Cat-CVD methods,” *Surf. Coat. Technol.*, vol. 228, pp. S389–S392, Aug. 2013, doi: 10.1016/j.surfcoat.2012.05.085.

[13] H. Puliyalil, G. Filipič, and U. Cvelbar, “Recent Advances in the Methods for Designing Superhydrophobic Surfaces,” *Surf. Energy*, Dec. 2015, doi: 10.5772/60852.
[14] A. Tuteja, W. Choi, J. M. Mabry, G. H. McKinley, and R. E. Cohen, “Robust omniphobic surfaces,” *Proc. Natl. Acad. Sci.*, vol. 105, no. 47, pp. 18200–18205, Nov. 2008, doi: 10.1073/pnas.0804872105.
[15] E. Khalili and M. Sarafbidabad, “Combination of laser patterning and nano PTFE sputtering for the creation a super-hydrophobic surface on 304 stainless steel in medical applications,” *Surf. Interfaces*, vol. 8, pp. 219–224, Sep. 2017, doi: 10.1016/j.surfin.2017.06.008.
[16] K. D. Esmeryan, C. E. Castano, A. H. Bressler, M. Abolghasemibizaki, and R. Mohammadi, “Rapid synthesis of inherently robust and stable superhydrophobic carbon soot coatings,” *Appl. Surf. Sci.*, vol. 369, pp. 341–347, Apr. 2016, doi: 10.1016/j.apsusc.2016.02.089.
[17] K. D. Esmeryan, C. E. Castano, A. H. Bressler, C. P. Fergusson, and R. Mohammadi, “Single-step flame synthesis of carbon nanoparticles with tunable structure and chemical reactivity,” *RSC Adv.*, vol. 6, no. 66, pp. 61620–61629, 2016, doi: 10.1039/C6RA06436A.
[18] R. N. Wenzel, “RESISTANCE OF SOLID SURFACES TO WETTING BY WATER,” *Ind. Eng. Chem.*, vol. 28, no. 8, pp. 988–994, Aug. 1936, doi: 10.1021/ie50320a024.
[19] A. B. D. Cassie and S. Baxter, “Wettability of porous surfaces,” *Trans. Faraday Soc.*, vol. 40, no. 0, pp. 546–551, Jan. 1944, doi: 10.1039/TF9444000546.
[20] N. A. Patankar, “On the Modeling of Hydrophobic Contact Angles on Rough Surfaces,” *Langmuir*, vol. 19, no. 4, pp. 1249–1253, Feb. 2003, doi: 10.1021/la026612+.
[21] J. Bico, C. Marzolin, and D. Quéré, “Pearl drops,” *EPL Europhys. Lett.*, vol. 47, no. 2, p. 220, Jul. 1999, doi: 10.1209/epl/i1999-00548-y.
[22] T. Onda, S. Shibuichi, N. Satoh, and K. Tsujii, “Super-Water-Repellent Fractal Surfaces,” *Langmuir*, vol. 12, no. 9, pp. 2125–2127, Jan. 1996, doi: 10.1021/la950418o.
[23] A. Lafuma and D. Quéré, “Superhydrophobic states,” *Nat. Mater.*, vol. 2, no. 7, pp. 457–460, Jul. 2003, doi: 10.1038/nmat924.
[24] Y. Yu, Z.-H. Zhao, and Q.-S. Zheng, “Mechanical and Superhydrophobic Stabilities of Two-Scale Surfacial Structure of Lotus Leaves,” *Langmuir*, vol. 23, no. 15, pp. 8212–8216, Jul. 2007, doi: 10.1021/la7003485.
[25] Q.-S. Zheng, Y. Yu, and Z.-H. Zhao, “Effects of Hydraulic Pressure on the Stability and Transition of Wetting Modes of Superhydrophobic Surfaces,” *Langmuir*, vol. 21, no. 26, pp. 12207–12212, Dec. 2005, doi: 10.1021/la052054y.
[26] Q. Zheng, C. Lv, P. Hao, and J. Sheridan, “Small is beautiful, and dry,” *Sci. China Phys. Mech. Astron.*, vol. 53, no. 12, pp. 2245–2259, Dec. 2010, doi: 10.1007/s11433-010-4172-1.
[27] C. Shi *et al.*, “Interaction between Air Bubbles and Superhydrophobic Surfaces in Aqueous Solutions,” *Langmuir*, vol. 31, no. 26, pp. 7317–7327, Jul. 2015, doi: 10.1021/acs.langmuir.5b01157.

[28] K. K. S. Lau *et al.*, “Superhydrophobic Carbon Nanotube Forests,” *Nano Lett.*, vol. 3, no. 12, pp. 1701–1705, Dec. 2003, doi: 10.1021/nl034704t.
[29] K. D. Esmeryan *et al.*, “Kinetically driven graphite-like to diamond-like carbon transformation in low temperature laminar diffusion flames,” *Diam. Relat. Mater.*, vol. 75, pp. 58–68, May 2017, doi: 10.1016/j.diamond.2017.01.014.
[30] N. Ohtake *et al.*, “Properties and Classification of Diamond-Like Carbon Films,” *Materials*, vol. 14, no. 2, p. 315, Jan. 2021, doi: 10.3390/ma14020315.
[31] D. Öner and T. J. McCarthy, “Ultrahydrophobic Surfaces. Effects of Topography Length Scales on Wettability,” *Langmuir*, vol. 16, no. 20, pp. 7777–7782, Oct. 2000, doi: 10.1021/la000598o.
[32] J. P. Youngblood and T. J. McCarthy, “Ultrahydrophobic Polymer Surfaces Prepared by Simultaneous Ablation of Polypropylene and Sputtering of Poly(tetrafluoroethylene) Using Radio Frequency Plasma,” *Macromolecules*, vol. 32, no. 20, pp. 6800–6806, Oct. 1999, doi: 10.1021/ma9903456.
[33] J. L. Parker, “Surface Force Measurement Techniques and Their Application to the Interaction Between Surfactant Coated Surfaces,” in *Studying Cell Adhesion*, P. Bongrand, P. M. Claesson, and A. S. G. Curtis, Eds., Berlin, Heidelberg: Springer, 1994, pp. 65–79. doi: 10.1007/978-3-662-03008-0_5.
[34] H. K. Christenson and P. M. Claesson, “Cavitation and the interaction between macroscopic hydrophobic surfaces,” *Science*, vol. 239, no. 4838, pp. 390–392, Jan. 1988, doi: 10.1126/science.239.4838.390.
[35] A. Carambassis, L. C. Jonker, P. Attard, and M. W. Rutland, “Forces Measured between Hydrophobic Surfaces due to a Submicroscopic Bridging Bubble,” *Phys. Rev. Lett.*, vol. 80, no. 24, pp. 5357–5360, Jun. 1998, doi: 10.1103/PhysRevLett.80.5357.

Chapter 8 Appendices

Co-authorships by Ashton Bressler on the topic of superhydrophobic.

Publication 8.1

K. D. Esmeryan *et al.*, “Kinetically driven graphite-like to diamond-like carbon transformation in low temperature laminar diffusion flames,” *Diam. Relat. Mater.*, vol. 75, pp. 58–68, May 2017, doi: 10.1016/j.diamond.2017.01.014.

Publication 8.2

K. D. Esmeryan, A. H. Bressler, C. E. Castano, C. P. Fergusson, and R. Mohammadi, “Rational strategy for the atmospheric icing prevention based on chemically functionalized carbon soot coatings,” *Appl. Surf. Sci.*, vol. 390, pp. 452–460, Dec. 2016, doi: 10.1016/j.apsusc.2016.08.101.

Publication 8.3

K. D. Esmeryan, C. E. Castano, A. H. Bressler, M. Abolghasemibizaki, and R. Mohammadi, “Rapid synthesis of inherently robust and stable superhydrophobic carbon soot coatings,” *Appl. Surf. Sci.*, vol. 369, pp. 341–347, Apr. 2016, doi: 10.1016/j.apsusc.2016.02.089.

Publication 8.4

K. D. Esmeryan, C. E. Castano, A. H. Bressler, C. P. Fergusson, and R. Mohammadi, “Single-step flame synthesis of carbon nanoparticles with tunable structure and chemical reactivity,” *RSC Adv.*, vol. 6, no. 66, pp. 61620–61629, 2016, doi: 10.1039/C6RA06436A.

Diamond & Related Materials 75 (2017) 58–68

Contents lists available at ScienceDirect

Diamond & Related Materials

journal homepage: www.elsevier.com/locate/diamond

Kinetically driven graphite-like to diamond-like carbon transformation in low temperature laminar diffusion flames

Karekin D. Esmeryan [a,b], Carlos E. Castano [c], Ashton H. Bressler [a], Mehran Abolghasemibizaki [a], Christian P. Fergusson [a], Allan Roberts [a], Reza Mohammadi [a,*]

[a] Department of Mechanical and Nuclear Engineering, Virginia Commonwealth University, Richmond, VA 23284, USA
[b] Georgi Nadjakov Institute of Solid State Physics, 72, Tzarigradsko Chaussee Blvd., 1784 Sofia, Bulgaria
[c] Nanomaterials Core Characterization Facility, Department of Chemical and Life Science Engineering, Virginia Commonwealth University, Richmond, VA 23284, USA

ARTICLE INFO

Article history:
Received 7 November 2016
Received in revised form 18 January 2017
Accepted 20 January 2017
Available online 21 January 2017

Keywords:
Carbon nanoparticles
Diamond-like carbon
Laminar diffusion flames
Rapeseed oil
Reaction kinetics
Soot

ABSTRACT

Historically, the synthesis of diamond and graphite via combustion flames stands out as a simplified, scalable and inexpensive approach. Unfortunately, this method is not beneficial for industrial applications in coatings due to limitations related with the high flame and substrate temperatures. Here, we report novel findings about the formation mechanism of graphite-like and diamond-like supported nanostructures in low temperature laminar diffusion flames. Both materials are formed upon controllable combustion at atmospheric pressure of a cylindrical paper wick immersed in rapeseed oil. An accurate adjustment of the incident air flow and the amount of available fuel allow deposition of carbon soot or diamond-like carbon (DLC). The DLC formation is favorable in a narrow stoichiometric range at flame temperatures within ~210–260 °C and beyond this range the particles precipitate as soot. The comparative structural analysis using scanning electron microscopy, Raman spectroscopy, X-ray photoelectron spectroscopy and transmission electron microscopy, along with the full thermal and stoichiometric profiles for the chosen combustion conditions, suggest a kinetically driven graphite-to-diamond transformation rather than a thermodynamically induced phase transition. Our results reveal a new direction in the principles of graphite and diamond formation in flames that could be applied to surmount the existing shortcomings in flame synthesis.

1. Introduction

The life in its present form would be impossible without the participation of carbon, as it is a common chemical element that provides the building blocks of various drugs, pesticides and dyes [1]. The structural diversity of carbon is unrivaled in the periodic table, but regardless of the tremendous research activities on the other allotropic forms, including fullerenes and carbon nanotubes, so far, diamond and graphite remain the most industrially exploited carbon allotropes [2].

Among the well known methods for synthesis of diamond and graphite, such as detonation of carbon-based explosives [3], plasma-enhanced chemical vapor deposition [4], pulsed laser deposition [5,6], ion beam/magnetron sputtering [7–9], etc., the combustion flame synthesis at atmospheric pressure offers overwhelming simplicity and several advantages [10–14]. For instance, the chemically reactive environment of the flame ensures high deposition rates of over 0.028 μm/s and ~1.5–2 μm/s for diamond-like and graphite-like nanostructures, respectively, within a single-step process [15,16]. Also, the method is scalable and has a potential for a large-volume continuous production at low cost [13]. Furthermore, in terms of the diamond deposition, the combustion method can produce high-quality diamond, since the atmospheric oxygen etches the graphitic impurities very efficiently [15]. In addition, the combustion systems are highly convective and any changes in the oxygen-fuel ratio, fuel composition and/or the deposition conditions allow an accurate and fast adjustment of the physical properties of diamond coatings [15,17].

Although the combustion flame technique is a versatile tool, its applicability is more laboratory than industrially oriented. One of the important technological constraints is related to the high flame temperature (~600 °C up to ~3000 °C, depending on the material burned and flame type [18]) that hinders the practical usability of substrates with low thermal sustainability. Another disadvantage is that the flame, either laminar or turbulent, could induce large radial inhomogeneity in the growth rate, surface morphology or the quality of the layers [19]. Also, the formation mechanism of carbon nanoparticles and their

* Corresponding author.
E-mail address: rmohammadi@vcu.edu (R. Mohammadi).

http://dx.doi.org/10.1016/j.diamond.2017.01.014
0925-9635/

dynamics during the fuel combustion are not completely clarified [20], which also impedes the successful industrial adoption of the flame method.

Substantial progress in regard to the fundamentals of carbonaceous nanoparticles formation in various flames has been achieved in the past two decades [21–28]. Theoretical models based on the chemical kinetics of the incipient particles have been used to determine the particles size distribution in laminar premixed flames, as well as the onset of the transition from coalescent to aggregate particle growth [21–23]. Thereby, important insights about the internal structure and dynamics of the incipient carbon particles, along with their clustering at high temperatures have been provided [24–26]. It has been designated that the gas-phase chemistry, flame temperature, and the burner-to-substrate distance are critical for the morphology and structure of diamond and graphite nanomaterials [21, 23,27,28]. Thus, many features of the gas-phase dynamics seem quite well understood, although it is still relatively hard to define the exact reaction mechanisms [28]. Further progress towards the enrichment of the state-of-the-art in flame synthesis has recently been achieved by our research group. We have developed a novel chimney-based combustion method that overcomes the technological constraints of the high flame temperature and promotes the deposition of carbon nanostructures with an adjustable fraction of graphitic-like and diamond-like phases [29]. Surprisingly, in the conditions of low temperatures (T_{flame} ~ 270 °C) we have observed graphite-to-diamond transformation triggered without additional catalysts or reagents (only rapeseed oil has been used as a hydrocarbon precursor). Also, relatively uniform carbon films have been deposited across the substrate, especially for the graphite-like coatings (soot), with slight ±7.5% film thickness deviations [29].

However, in the absence of a catalyst, the direct graphite-to-diamond transformation is associated with high pressures and/or temperatures due to the separation of two phases by a high energy barrier (~0.4 eV per atom), despite of their comparable free energies (~0.02 eV difference per atom) [30,31]. Furthermore, since graphite is the stable form of carbon at ambient pressures, the formation of diamond from carbon-rich fuels requires high flame and substrate temperatures that will provide the thermal energy needed for activation of the gas species [10–12,15,17]. Therefore, the observed phase transition at low flame temperatures is questionable and highly unlikely from a thermodynamic point-of-view [30,31]. In contrary to that concept, recent experiments have shown the presence of four well known allotropic forms of carbon in a candle flame, namely diamond, graphite, fullerenes and amorphous carbon [32,33]. Moreover, in an odd research, the incomplete combustion of naphthalene has lead to local alteration of the interlayer spacing between the concentric shells of carbon onions from 0.34 nm (graphite-like) to 0.29 nm (diamond-like) [34]. Similar result has also been reported for carbon nanoparticles generated from the flame of paraffin oil, where some of the lattice spacings are ascribed to diamond-like carbon [35]. These findings, along with the recently proposed non-equilibrium route to diamond formation [36], suggest that the catalyst-free graphite-to-diamond transition at low flame temperatures might not be an artifact. Unfortunately, there is a profound lack of follow-up research articles that at least can partially enlighten on the mechanism of diamond formation in the case of low temperature combustion flames.

The primary objective of this paper is to provide new insights about the nature of nascency of diamond in low temperature laminar diffusion flames. Based on an enhanced combustion system with an accurate air flow control, we demonstrate that the diamond deposition from the incomplete combustion of rapeseed oil is favorable in a narrow stoichiometric range at flame temperatures within ~210–260 °C. These observations suggest a kinetically driven graphite-to-diamond transformation rather than a thermodynamically induced phase transition.

2. Experimental

2.1. Detailed description of the combustion system

The most recent model of our combustion system with a precise air flow control is depicted in Fig. 1. An Intex Quick-Fill 12v-DC electric air pump is powered by an Antec BP550 PLUS modular power supply and used to provide the atmospheric oxygen required for the combustion process. The air pushed by the pump flows through ~70 cm long tubing with an internal diameter (ID) of ~1 cm before reaching a controllable gas flow meter (McMaster Carr 5079K25). The latter ensures an adjustable air flow within 0.0014–0.0052 m^3/min that reaches an inverted tin funnel (McMaster Carr 8996T12) connected to the flow meter via an additional ~20 cm long aluminum pipe with an ID ~1.1 cm and ~50 cm of tubing. The metal pipe is sealed to the funnel by using high temperature stove cement (McMaster Carr 7573A31, RUTLAND brand) and a ring stand supports that configuration by clamping to the aluminum tube.

During the experiments, a cylindrical-shaped paper wick was immersed in a Pyrex dish containing rapeseed oil, which was used as a hydrocarbon precursor. After ignition of the wick and subsequent stabilization of its flame, the air pump was switched on and the funnel was gently pulled above the wick. Then, the air flow was accurately set via the flow meter and finally the funnel was lowered over the inflamed wick. According to this setup, several combustion scenarios were simulated at three distinct wick dimensions (diameter and height $d \times h = 0.9 \times 2.5$ cm; 1.2×2.5 cm and 2.4×2.5 cm) and air flow ranging within 0.0014–0.0052 m^3/min with a step of ~0.0005–0.0009 m^3/min. The choice of these parameters was related to tuning of the oxygen-fuel ratio, which is critical for the physical properties of the deposited carbon nanostructures [16,21,29]. Thus, by manipulating *in-situ* the combustion of rapeseed oil and observing the corresponding morphological and structural changes in the nanomaterials, we were capable of determining the probable mechanism of graphite-to-diamond transformation.

2.2. Flame characteristics

An inverted tin funnel was utilized to generate a laminar diffusion flame, whose characteristics are illustrated in Fig. 2.

In the absence of a funnel, the flame flow of the ignited wick was turbulent and the atmospheric oxygen diffused into the vaporized fuel (rapeseed oil), creating three visible flame regions, namely outer, inner and center. After applying the funnel, the combustion was still maintained by diffusion, but the gas flow converted from turbulent to laminar due to the narrow exhaust vent. At that stage, four distinct regions with specific flame/flow characteristics were observed. The first

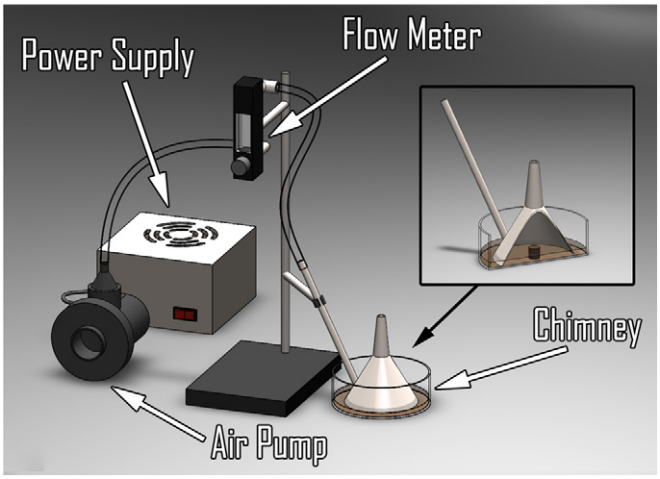

Fig. 1. General view of the combustion system.

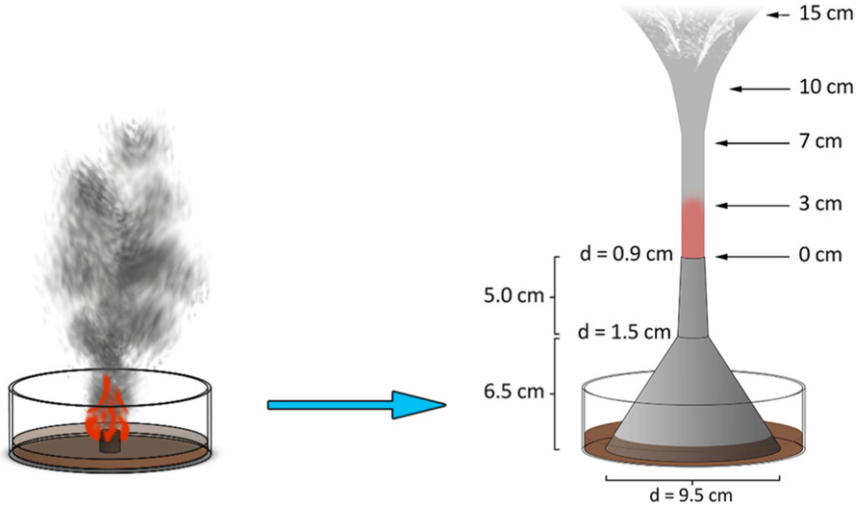

Fig. 2. Schematic representation of the flame characteristics.

one was located within 0–3 cm above the funnel's tip and associated with a laminar flame flow possessing orange-red color, caused by the incandescence of very fine soot particles produced in the flame. The second region was situated within 3–7 cm above the funnel and referred to as post-flame (thermal plume) region, where the flame completely vanished [18]. For our particular case, however, the flow in that region was still laminar, while at the third and fourth fume domains (7–10 cm; 10–15 cm), also assigned to the thermal plume region, the gas-flow reconverted to turbulent.

The flame temperature in an open atmosphere and upon controlled combustion in the funnel was measured using a Signstek 3 1/2 6802 II dual channel digital thermometer with a WRNK- 187 K-type thermocouple probe sensor, allowing thermal readings within 0–1100 °C with a measurement accuracy of ±0.1–0.4 °C. Initially, the probe of digital thermometer was placed in the flame of the burning wick and its temperature was recorded after reaching stable value within ±0.5 °C. Subsequently, the same procedure was applied upon setting the funnel and the flame temperature was determined above the funnel's tip at a specific distance associated with each flame/fume region (see Fig. 2). According to that setup, a certain amount of solid carbonaceous particles with a very low apparent density of ~0.04–0.59 g/cm^3 may accumulate on the sensor probe [29]. However, this would adversely affect the readings only upon precipitation of sufficiently thick carbon films (e.g. tenth of a mm) causing shielding of the temperature effect.

2.3. Determination of the oxygen-fuel ratio and deposition conditions

The oxygen-fuel ratio is defined as the mass ratio of oxygen to fuel vapor available in the combustion process [10–12,15,17,19]. However, due to the presence of a liquid phase in the combustion reactor and since a cylindrical wick with a certain surface area was used to provide the oil vapor; we determined the oxygen-fuel ratio in relative molar units. The exact oxygen content was deduced as one fifth of the total air flow reaching the reactor, as the air contains ~20% oxygen and ~80% nitrogen. The mole fraction of oxygen was then calculated by knowing that at standard temperature and pressure 1 mol of air occupies 22.4 l. The fuel content was estimated by measuring the amount of liquid rapeseed oil consumed for 20 min continuous combustion at each particular air flow and wick dimensions (see Section 2.1). Then, the molar mass of the evaporated liquid was determined by taking into account the molecular weight of rapeseed oil (992 g/mol) and its mass density (0.9186 g/cm^3) [37].

The deposition of carbon nanostructures was performed on 2.5 × 2.5 cm microscope glass slides (Fisher Scientific, USA) at burner-to-substrate distance L ~ 3–15 cm, corresponding to each flame/flow region, for a variety of oxygen-fuel ratios determined by the chosen air flow and wick's dimensions. The deposition time t was varied within 20–60 s in order to produce ~10–40 μm thick carbon coatings [29].

2.4. Surface characterization

Circumstantial characterization data of the synthesized carbonaceous nanoparticles are provided in our previous investigation [29]. Here, we utilized scanning electron microscopy (SEM), Raman spectroscopy, X-ray photoelectron spectroscopy (XPS), transmission electron microscopy (TEM) and X-ray diffraction (XRD) ensuring the data required for comparative analysis and establishment of the probable formation mechanism. The SEM experiments were performed using a Hitachi SU-70 field emission scanning electron microscope and images were taken at magnifications up to 25 kX. Raman spectra of the coatings were recorded from 1000 to 1900 cm^{-1} with an acquisition time of 300 s in a Horiba LabRam HR Evolution Confocal Raman Spectrometer, using a 20 mW/532 nm He-Ne laser excitation system. Subsequently, the spectra were deconvoluted via a five-peak fitting procedure after a linear baseline subtraction. The high resolution XPS data were collected with a Thermo Fisher ESCALAB 250 X-ray photoelectron spectrometer at a step of 0.1 eV. The molecular structure of carbon samples was evaluated via TEM and XRD using a Zeiss Libra 120 system operating at 120 kV with a point-to-point resolution of 0.34 nm and a Panalytical X'Pert Pro diffractometer operating in Bragg-Brentano mode, respectively. An incident X-ray beam was generated with Cu Kα radiation (λ = 1.54 Å) and the samples were scanned from 20° to 100° of 2θ, at 0.0032826° scan step size, 1° anti-scatter slit, 1/2° fixed divergence slit and 15 mm mask.

3. Results and discussion

3.1. Morphological features of the generated nanoparticles

Fig. 3 represents the morphology of carbon nanoparticles during different stages of the combustion process.

As seen in Fig. 3a, the open flame generates quasispherical nanoparticles that aggregate in a fractal-like network composed of elongated carbon chains separated by micro- nanoscale pores. Such a configuration is associated with superhydrophobic carbon soot that is highly fragile upon mechanical intervention and water interactions due to the prevalent sp^2 hybridization and the presence of dangling π—π* bonds [16,29,38]. Upon controlled combustion in our funnel, however, the soot changes its morphology and structure, and three prominent transition states occur. Initially, at an air flow of 0.0042 m^3/min, the soot is in

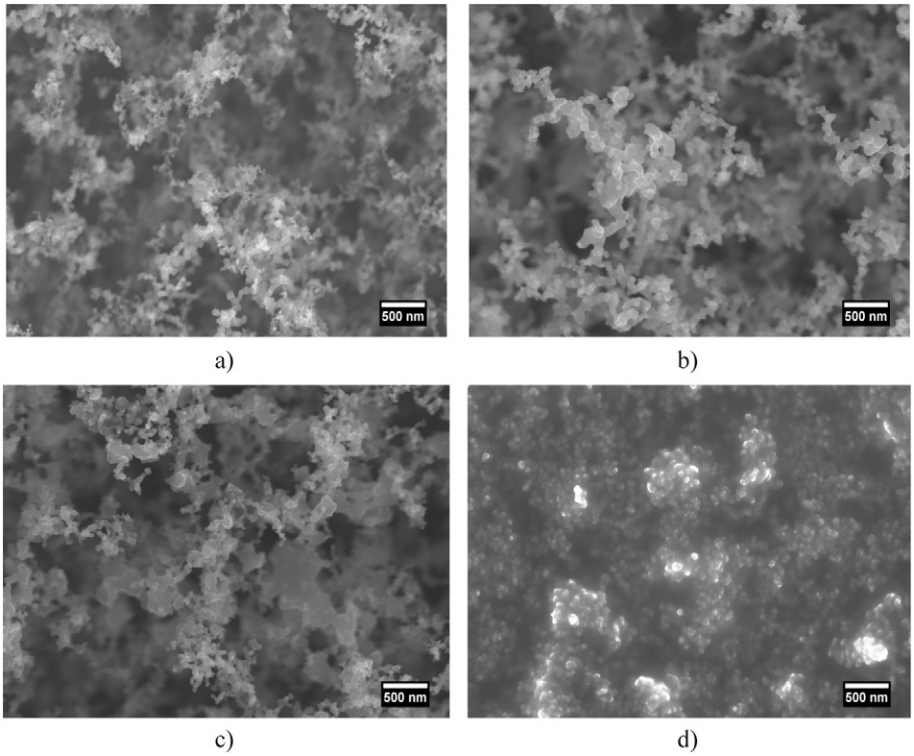

Fig. 3. Scanning electron micrographs of carbon nanostructures deposited at wick dimensions of 1.2 × 2.5 cm and $L \sim 3$ cm via a) an open flame and b) upon controllable combustion at an air flow of 0.0042 m^3/min, c) 0.0033 m^3/min and d) 0.0024 m^3/min.

an intermediate state, where most of the carbon chains look dense and fused, but some small areas still contain sphere-like particles (see Fig. 3b). Further reduction of the air flow to 0.0033 m^3/min induces a complete morphological transformation of the soot. At that stage, the nanoparticles are tightly connected and fused; forming elongated quasisquares, but the overall fractal-like structure is preserved. This arrangement corresponds to inherently robust carbon soot with an increased sp^3 hybridization and substantially reduced amount of π—π* bonds [16,29]. A subsequent decrease in the air flow to 0.0024 m^3/min causes a remarkable modification of both the morphology and structure of the uncombusted carbon particles. They convert into fine nanoscale grains, growing as bigger carbon clusters with reduced porosity compared to the soot (see Fig. 3d). These features of the particles completely match those in our previous study and presume the formation of highly sp^3 hybridized diamond-like carbon (DLC) with a short-range ordered nanocrystallinity [29]. The reported results suggest also an oxygen-fuel ratio dependent graphite-to-diamond transformation, which is partially supported by the kinetic models of soot formation in laminar premixed flames [21–23]. The models do not address possible structural transitions, but do explain the morphological alteration in the soot as a consequence of the reduced oxygen content and will be used as a key reference later in the article.

3.2. Structural analysis

To verify that the grain-like clusters deposited via the current experimental setup could be ascribed to DLC, we performed Raman spectroscopy, the results of which are shown in Fig. 4.

The visible Raman spectrum of amorphous carbon, such as soot, shows two prominent features and some minor modulations that can accurately be analyzed using a five-band fitting procedure [39]. According to that approach, the intensity peaks at ~1590 cm^{-1} and ~1350 cm^{-1} are associated with the G-band and D1-band of disordered graphite. The first one corresponds to the ideal graphitic lattice vibration mode with E_{2g} symmetry, while the D1-band is "forbidden" in perfect graphite and arises only in the presence of disorder due to the activation of A_{1g} symmetry mode [39,40]. Another three bands, labeled as D2, D3 and D4, complement the Raman spectra and account for lattice vibrations analogous to that of the G-band (D2-band), amorphous carbon fraction of soot (D3-band) and sp^2—sp^3, C—C or C ═C stretching vibrations (D4-band) [39]. The exact location of all five bands and their intensity depends on the type of material and its molecular structure (short-range order) [39,40].

At an open flame, the corresponding Raman spectrum accounts for the formation of highly disordered graphitic carbon with almost equal intensities of D1-band and G-band, giving an I_{D1}/I_G ratio of 0.9. Also, the high D1-band intensity is strictly related to a sixfold aromatic ring structure of the particles, while the D3-band accounts for the large fraction of amorphous carbon soot [39,40]. Such an interpretation is in perfect agreement with the quasispherical fractal-like network of the soot, revealed by the SEM (see Fig. 3a). Upon controlled combustion at an air flow of 0.0033 m^3/min, both D1-band and D3-band decrease their intensities and the I_{D1}/I_G ratio reduces up to ~0.76. Intuitively, this is attributed to the decreased quantity of disordered aromatic ring-shaped particles, which is clearly evident from the alteration of the soot's morphology (see Fig. 3c), as well as the increased amount of sp^3 bonds in the material [16,29]. We referred this state to as "modified" carbon soot with inherent robustness in terms of water jetting and dynamic water droplet interactions [16]. Although the spectra in Fig. 4a and b are similar to those reported for nanodiamonds, the location of G-band at 1591 cm^{-1} differs towards that of nanodiamond (~1640 cm^{-1}), indicating the absence of diamond phase and nanostructures composed mainly of graphitic shells [31].

Further reduction of the air flow to 0.0024 m^3/min causes a significant modification of the Raman spectrum. First, the D1-band intensity decreases vastly and the I_{D1}/I_G ratio collapses to ~0.67, indicating less disordered structure and distribution of clusters with orders and dimensions different than those of the aromatic rings [40]. Moreover, the D1-band shifts up to ~1360 cm^{-1} and overlaps the Raman scattering peak for bulk diamond at ~1332 cm^{-1} [2,40]. Second, the G-band is also

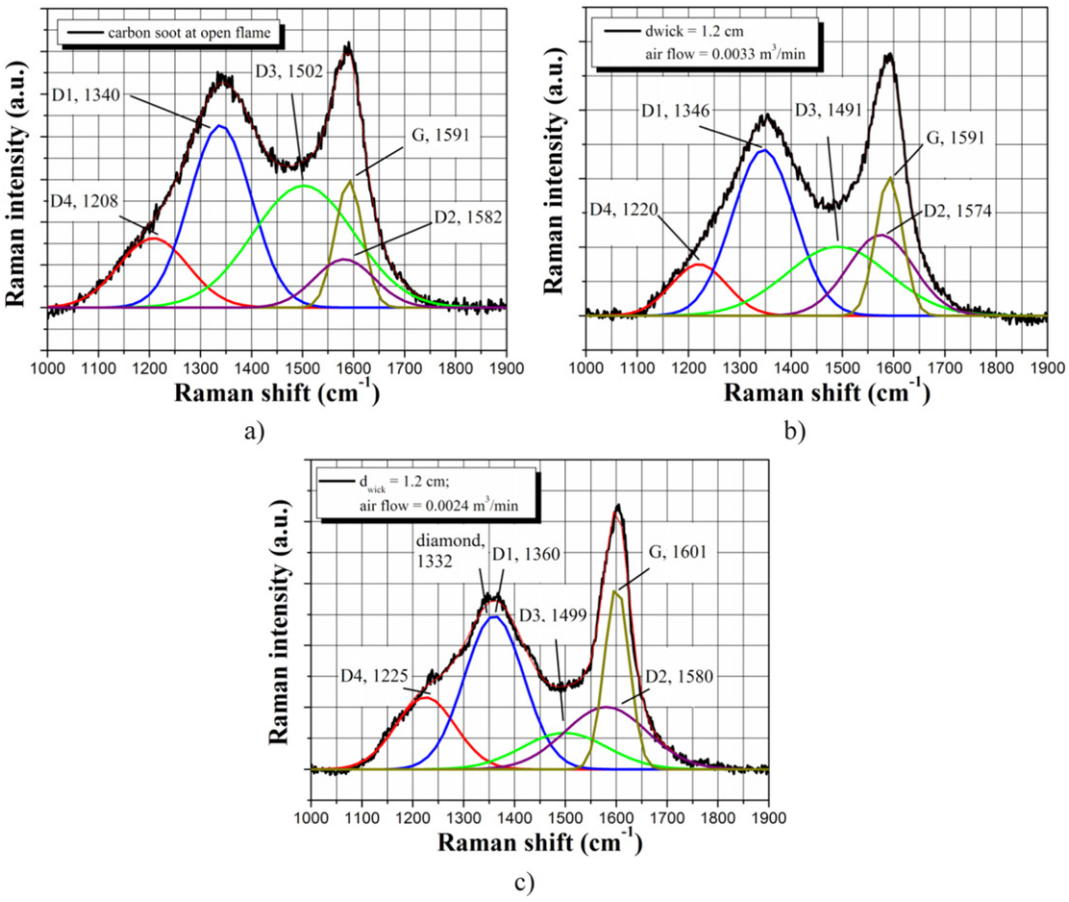

Fig. 4. Raman spectra of carbon nanostructures deposited at wick dimensions of 1.2 × 2.5 cm and L ~ 3 cm via a) an open flame and b) upon controllable combustion at an air flow of 0.0033 m^3/min and c) 0.0024 m^3/min. The goodness-of-fit is indicated by a high correlation coefficient value within 0.995–0.997.

shifted up from ~1591 cm^{-1} to 1601 cm^{-1}, likely as a result of the increased sp^3 content triggered by a change of sp^2 configuration from rings to olefinic C ═C groups with higher vibration frequencies [40]. In addition, the D3-band is less prominent in comparison with its intensity for the first two regimes of combustion (Fig. 4a, b); meaning that the overall soot content is low. Very similar spectral behavior is reported for nanodiamonds synthesized by ethanol dissociation [41] or using low power density microwave plasma-enhanced chemical vapor deposition [2]. These results support the probability for structural soot-to-DLC transformation, implied by the SEM imaging and unambiguously stated in our previous report [29].

Another corroborative argument is that the grain-like clusters showed in Fig. 3d, as well as their Raman spectrum in Fig. 4c, may correspond to an amorphous carbon with ~80% sp^3 bonds [29]. This is confirmed by a high-resolution XPS to the C1s performed on the grain-like nanostructures, as shown in Fig. 5.

The survey scan of these nanostructures reveals that the main component is carbon being ~92.5 at.% accompanied by oxygen with atomic

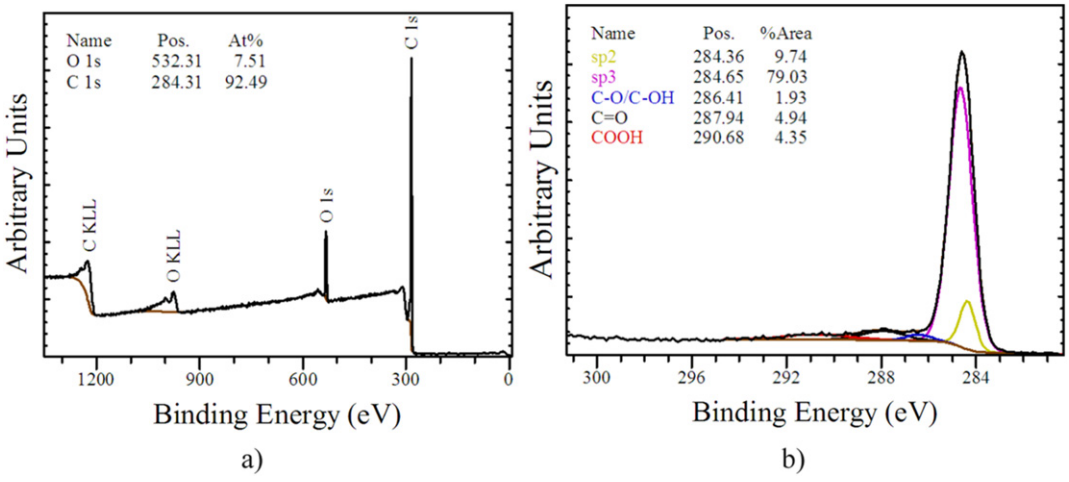

Fig. 5. Experimental data of a) XPS spectrum and b) C1s photoelectron core level of the grain-like clusters deposited at wick dimensions of 1.2 × 2.5 cm, upon controlled combustion at an air flow of 0.0024 m^3/min and L ~ 3 cm.

percentage of ~7.5 at.%. The two minor C_{KLL} and O_{KLL} peaks at higher binding energies correspond to the emission of Auger electrons of carbon and oxygen elements. In addition, the deconvolution of C1s shows mainly sp^3 hybridized carbon with sp^3 content approaching ~80%, along with the presence of other functional groups such as epoxy/hydroxyl (C—O—C/C—OH), carbonyl (C═O) and carboxylic acid (COOH) groups. The peak of COOH group is wide, suggesting the possibility for π—π* bonds formation, associated with the negligible sp^2 hybridization (~10%). Our material is considered in the literature as tetrahedral amorphous carbon (ta-C) that belongs to the family of DLC, thus, confirming the proposed structural transition [2,40].

The molecular structure of the samples was further investigated using TEM along with selected area electron diffraction (SAED) and XRD, as presented in Figs. 6 to 8

The TEM image in Fig. 6a confirms the spherical-like morphology of the soot generated via an open flame. The corresponding SAED pattern (Fig. 7a) exhibits a few continuous rings and diffused halos, suggesting the presence of a short-range order and amorphous phase. The diffraction rings are mainly assigned to graphite (G) structure and one peak that possibly could match diamond (D). Upon controlled combustion at an air flow of 0.0033 m^3/min (Fig. 6b), the scanned area indicates overlapped and fused carbon nanoparticles, whereas the SAED pattern shown in Fig. 7b mainly two diffused halos, one assigned to graphitic-like and the other to diamond-like nanostructures. In contrast, Fig. 6c illustrates more crystalline structure of the particles generated at an air flow of 0.0024 m^3/min. Denser composites with non-spherical morphology are observed and the rings in the SAED pattern are well defined (see Fig. 7c). The atomic d-spacing of the nanostructures in this particular case can be ascribed to both graphitic-like and diamond-like carbon with less amorphous phase in overall. A summary of these measurements along with the STD d-spacing for diamond and graphite is presented in Table 1.

Although graphitic-like structures are still present, the appearance of mainly sp^3 hybridized carbon and a short-range nanocrystallinity (see Fig. 5 and Table 1) imply that the combustion regime at an air flow of 0.0024 m^3/min and wick dimensions of 1.2 × 2.5 cm tends to form carbon with mostly diamond phase.

Finally, the XRD measurements shown in Fig. 8 will clarify whether the synthesized material at an air flow of 0.0024 m^3/min should be considered as nanodiamond or DLC. By definition, diamond is a tetrahedral (sp^3) bonded allotrope of carbon; however, not every material with considerable sp^3 bonding could possess the properties of bulk diamond [2]. This is the case for DLC, which has many of the bulk diamond features, but is fundamentally amorphous [2]. Furthermore, the appearance of crystallinity and mainly tetrahedral bonds is not an absolute prerequisite for the possession of bulk diamond properties, as the grain size and the amount of amorphous grain boundaries can "shift" the material towards DLC or bulk diamond [2].

The XRD spectrum shows one strong peak at 2Theta of 28.5 (2° apart from the graphite peak), which probably is induced by the graphite-like carbon content in the material. In addition, a weak peak at 2Theta of 43.5 clearly shows the appearance of (111) textured diamond. This peak is with negligible intensity, which means that the crystallinity is indeed on a short-range and most of the material is amorphous. Therefore, based on the detailed characterization and the nomenclature for crystalline and amorphous diamond [2], we conclude that the above discussed nanostructures should be considered as DLC rather than nanodiamond.

3.3. Structural and morphological variations in the nascent nanoparticles as a function of the experimental conditions

In this section, we aim to clarify the degree of importance of the flame temperature, oxygen-fuel ratio, burner-to-substrate distance L and the deposition time t for the formation of graphite-like or diamond-like materials. Fig. 9 reveals 2-D and 3-D maps of the flame temperature profiles, recorded in an open environment and upon controlled combustion.

The incomplete combustion of rapeseed oil in the open atmosphere creates an orange-red colored flame, whose temperature varies within 520–580 °C, which is in good agreement with the data reported for diffusion flames in open environments [18]. The observed deviations of ~60 °C from measurement to measurement (three sets for each size of the wick) are likely due to the turbulent nature of the flame. Since it moves around chaotically, some cooler fluxes from the surrounding atmosphere interact with the sensor probe, causing these slight upward or downward thermal shifts. In contrast, upon controlled combustion, the thermal readings are reproducible and two major parameters affect the flame color and its temperature, namely the air flow and wick's dimensions.

Careful analysis of the 3-D maps in Fig. 9 shows that at constant air flow and distance L (e.g. 0.0052 m^3/min; L ~ 3 cm), a gradual increase in the wick's diameter (d_{wick}) from 0.9 cm to 2.4 cm leads to an increase in the flame temperature (T_{flame}) from ~200 °C up to ~450 °C. This is a consequence of the larger amount of fuel involved in the combustion that is giving off more heat in the subsequent exothermic chemical reaction. On the other hand, at constant d_{wick} of 0.9 cm and L ~ 3 cm, the reduction of air flow from 0.0052 m^3/min to 0.0033 m^3/min causes an

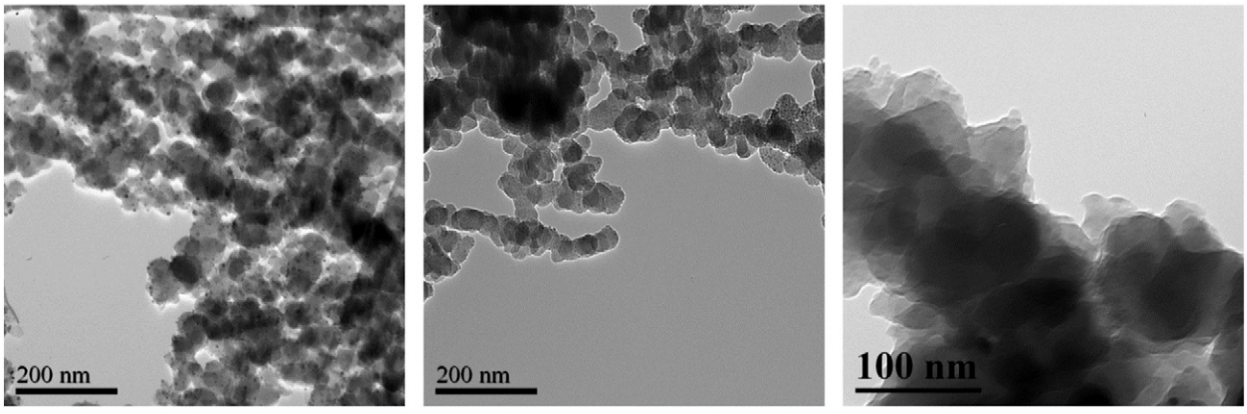

Fig. 6. TEM images of the carbon nanostructures deposited at wick dimensions of 1.2 × 2.5 cm and L ~ 3 cm via a) an open flame and b) upon controllable combustion at an air flow of 0.0033 m^3/min and c) 0.0024 m^3/min.

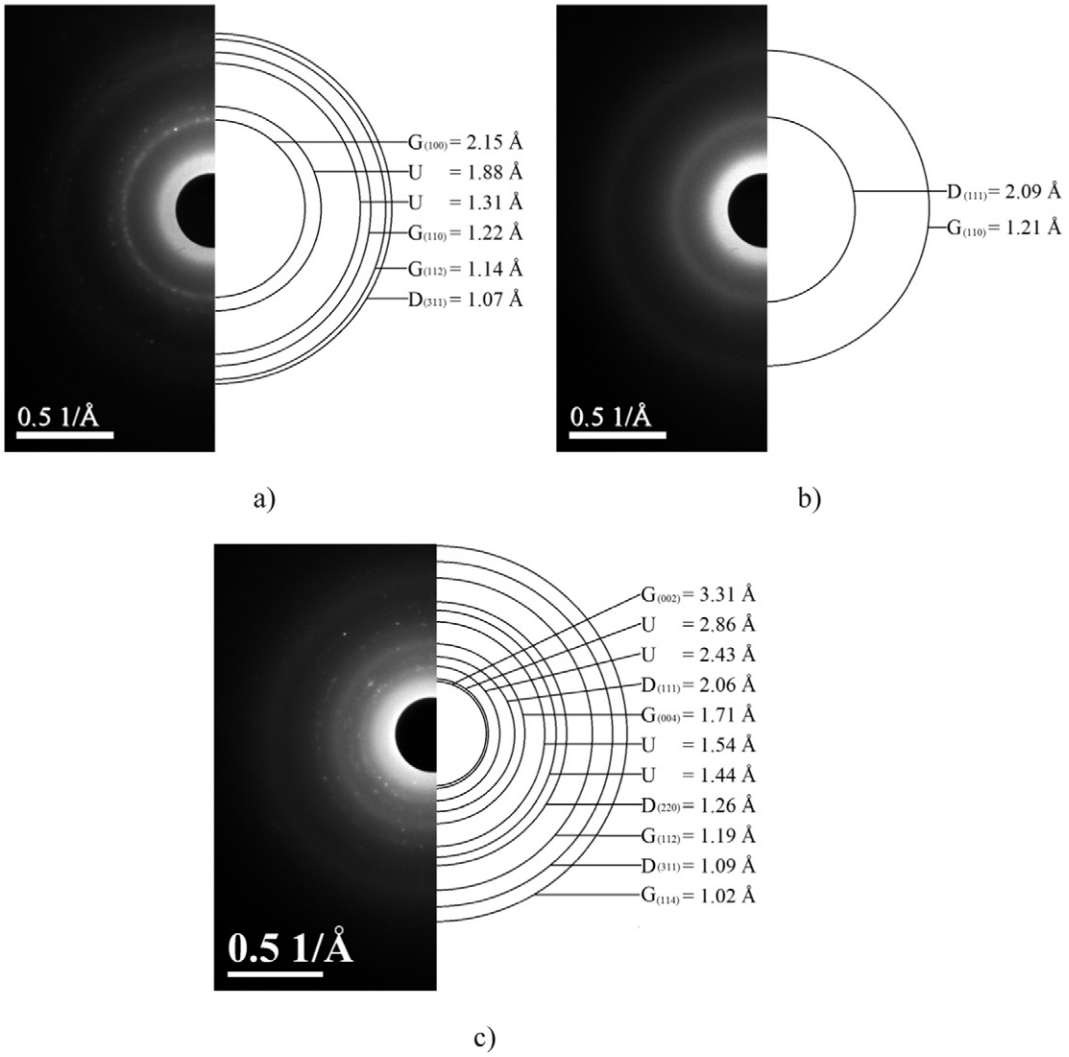

Fig. 7. SAED images of the carbon nanostructures deposited at wick dimensions of 1.2 × 2.5 cm and L ~ 3 cm via a) an open flame and b) upon controllable combustion at an air flow of 0.0033 m^3/min and c) 0.0024 m^3/min. The indices G, D and U correspond to graphite, diamond and unknown phase, respectively.

increase in T_{flame} with ~77 °C (see Fig. 9b), followed by relatively rapid cooling of ~67 °C at air flow of 0.0019 m^3/min. Similar temperature trend is observed in Fig. 9c, which implies that the amount of released thermal energy does not necessarily decay by reducing the air flow, as the combustion efficiency depends also on the success rate of oxidation

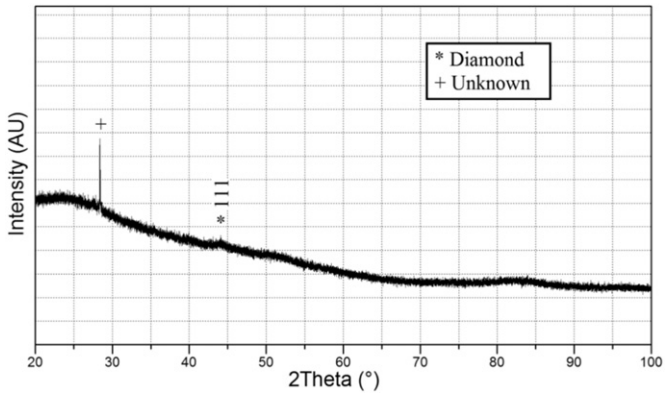

Fig. 8. X-ray diffraction of a glass slide coated with carbon nanostructures generated upon controlled combustion at wick dimensions of 1.2 × 2.5 cm, an air flow of 0.0024 m^3/min, and L ~ 3 cm.

[42]. In addition, at equal other conditions (constant d_{wick} and air flow), the variations in distance L induce corresponding changes in the flame temperature due to the specific characteristics of each flame/flow region (see Section 2.2).

Simultaneously with the thermal measurements, we coated approximately hundred 2.5 × 2.5 cm glass slides with carbon nanoparticles, generated at each measurement position, in order to correlate their morphological and structural peculiarities with the relevant combustion conditions. Regardless of the d_{wick}, an air flow of 0.0052 m^3/min promotes the formation of soot particles with either conventional (spherical) or mixed shape, assembled in chain-like aggregates (see Fig. 3a and b), and the flame's orange-red color is similar to that of an open flame. However, the transition to "modified" soot with inherent robustness (see Fig. 3c) is strongly influenced by the air flow and wick's surface area, which also affect the flame appearance. At a d_{wick} = 0.9 cm, the morphological alteration occurs at an air flow of 0.0024 m^3/min and subsequent increase in d_{wick} to 1.2–2.4 cm shifts up the transition point to flow values of 0.0033 m^3/min and 0.0042 m^3/min, respectively. In these stoichiometric regions, the flame width decreases and its color changes to dark red-brown, indicating an enhanced sooting tendency due to the lean oxygen content (at equal deposition time, the reduction of oxygen causes deposition of thicker soot coatings, as reported in ref. [16]). Identical behavior is observed upon analysis of the experimental conditions that trigger the soot-to-DLC transformation. First, the fume

Table 1
Comparison between the calculated d-spacing (Å) from the SAED patterns at different combustion regimes and the STD d-spacings and Miller index for diamond and graphite.

Calculated d-spacing (Å)			d-spacing and Miller index for some C allotropes			
			Diamond PDF 00-006-0675 Cubic Fd-3m		Graphite PDF 00-023-0064 Hexagonal P63/mmc	
Open flame	Air flow 0.0033 m^3/min	Air flow 0.0024 m^3/min	d-spacing (Å)	Miller index (h k l)	d-spacing (Å)	Miller index (h k l)
		3.31			**3.36**	**0 0 2**
		2.86				
		2.43				
2.15					**2.13**	**1 0 0**
	2.09	2.06	2.06	1 1 1		
					2.03	**1 0 1**
1.88						
		1.71			**1.67**	**0 0 4**
		1.54				
1.31		1.44				
		1.26	1.26	2 2 0		
1.22	**1.21**				**1.23**	**1 1 0**
1.14		**1.19**			**1.16**	**1 1 2**
1.07		1.09	1.07	3 1 1		
		1.02			**0.99**	**1 1 4**
			0.89	4 0 0		

The numbers in bold correspond to either graphite or diamond nanostructures. The latter is coloured in blue, while the previous in red.

alters its color to a light gray, while the flame is completely vanished. Second, the deposition of diamond-like structures becomes favorable only at air flows of 0.0019, 0.0024 and 0.0033 m^3/min when the wick's diameter (d_{wick}) is 0.9, 1.2 and 2.4 cm, respectively. Beyond this narrow range, the combustion conditions promote the formation of "modified", mixed or conventional soot particles. Interestingly, a similarity in the T_{flame} is observed in the vicinity of each transition, regardless of the chosen experimental conditions, as shown in Table 2.

According to Table 2, in two of three scenarios the flame temperature difference between the ranges for modified soot and DLC formation is ~60 °C. On the other hand, the substrate-to-burner distance L and deposition time t are irrelevant to the type of synthesized material. However, high-quality carbon nanostructures can be deposited only at L ~ 3 cm and for larger distances the quality rapidly decreases, likely due to the presence of oxidizing agents in the ambient atmosphere [28]. Furthermore, the time t determines only the thickness of the deposited carbon materials and does not affect any of their physicochemical properties. The above results, along with the resemblance of the T_{flame} at the transition regions, presume stoichiometric threshold that governs the particles' formation, as hinted in Fig. 10.

The oxygen-fuel ratio diagram confirms that the wick's larger surface area ensures increased amount of oil involved in the combustion, which also correlates with the increased flame temperature. Interestingly, the initial reduction of air flow causes unexpected gradual increase in the oxygen-fuel ratio to a point, where the relative oil vapor content becomes sufficient to decrease that ratio. At this point, different for each d_{wick}, the required stoichiometric threshold is reached and the nascency of diamond is preferential. Moreover, regardless of the equalized flame temperature values (see Table 2), the incipiency of diamond phase is favorable upon increase in the fuel content, because the hydrocarbons are unevenly distributed within the flame, which may facilitate or suppress the successful diamond growth [43]. In other words, there should be a sufficient amount of so called "carbon source" throughout

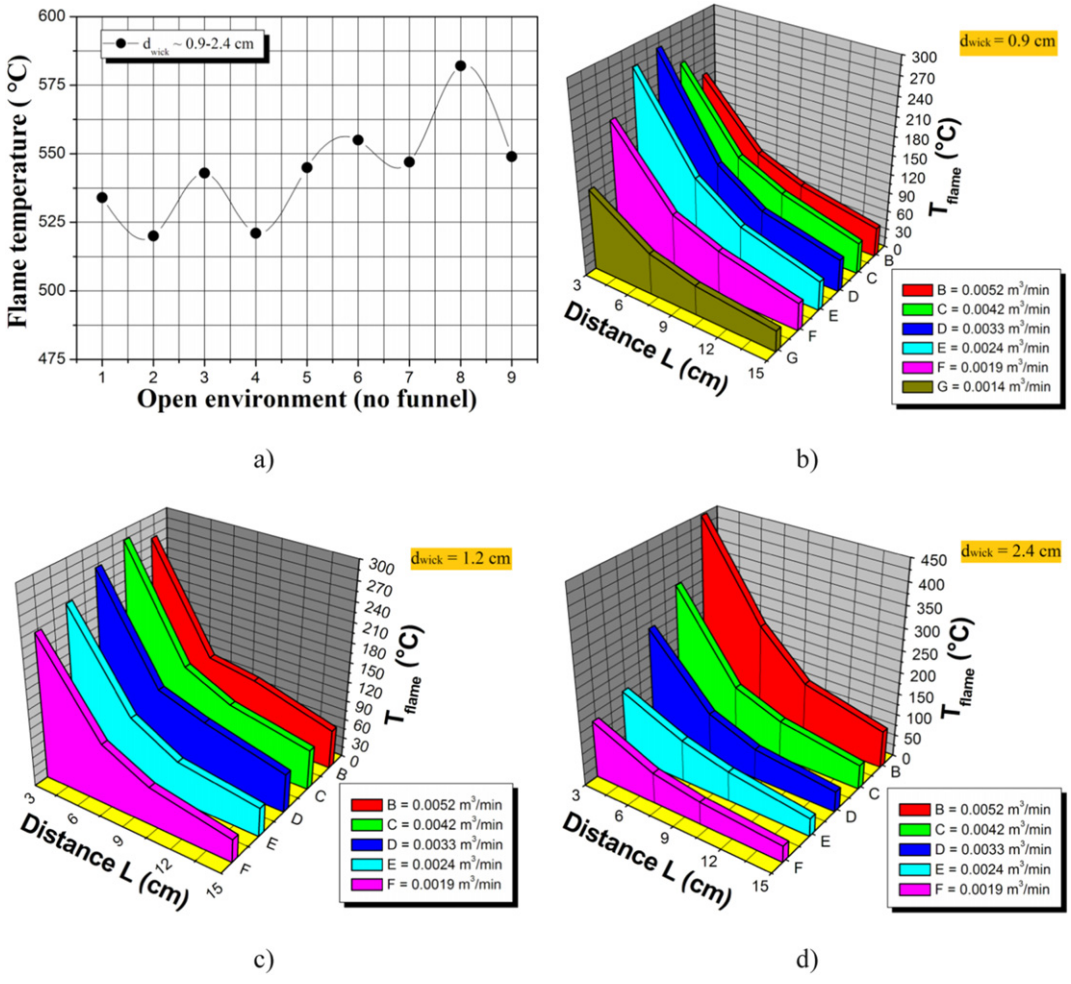

Fig. 9. Flame temperature profile in a) an open environment and b) upon controlled combustion at wick dimensions of 0.9 × 2.5 cm, c) 1.2 × 2.5 cm and d) 2.4 × 2.5 cm.

Table 2
Summarized experimental data for the type of synthesized carbon materials as a function of the deposition conditions.

Air flow (m^3/min)	d_{wick} (cm)	T_{flame} (°C)	L (cm)	Material
0.0052	0.9	200	3	Conventional soot
0.0042	0.9	240	3	Mixed soot
0.0033	0.9	277	3	Mixed soot
0.0024	0.9	270	3	Modified soot
0.0019	0.9	210	3	DLC
0.0052	1.2	270	3	Mixed soot
0.0042	1.2	285	3	Mixed soot
0.0033	1.2	270	3	Modified soot
0.0024	1.2	240	3	DLC
0.0019	1.2	225	3	No deposition
0.0052	2.4	450	3	Mixed soot
0.0042	2.4	325	3	Modified soot
0.0033	2.4	263	3	DLC
0.0024	2.4	150	3	No deposition
0.0019	2.4	125	3	No deposition

the flame in order to promote the formation of the required carbonaceous material [43]. These observations suggest that just a small part of the oxygen in the system is efficiently used to oxidize the fuel, while perhaps the excessive amount is released via the exhaust vent (funnel's tip). Hence, the estimation of the exact stoichiometry during the combustion process has a qualitative rather than a quantitative character. Nevertheless, the experimental conditions are in good agreement with the state-of-the-art in flame synthesis of diamond, since its formation is favorable in limited stoichiometric regions with sufficient mole fractions of fuel and lean oxygen content that suppresses the appearance of potential oxidizing agents [17,28]. Moreover, the observed tendency in DLC formation and the measured flame temperatures are in excellent agreement with the findings in our previous study, thereby, confirming that the basic mechanism of soot-to-DLC transformation is identical in both combustion systems [29].

3.4. Probable mechanism of the observed graphite-to-diamond transformation

The next few paragraphs provide new insights, although speculative to a certain extent, about the observed structural modifications during the incomplete combustion of rapeseed oil. For that purpose, we describe the formation mechanism of graphite-like and diamond-like nanostructures via the theory of soot formation in flames along with relevant numerical models for the reaction kinetics of the incipient carbonaceous particles [21–23,44]. Our considerations exclude the possibility for thermodynamically induced phase transition, since the maximum measured flame temperature of ~580 °C is well below the temperature of oxyacetylene flames, commonly used for thermal activation of the gas species and subsequent diamond formation [10–12,15,17]. Also, the proposed mechanism does not consider the probability for direct

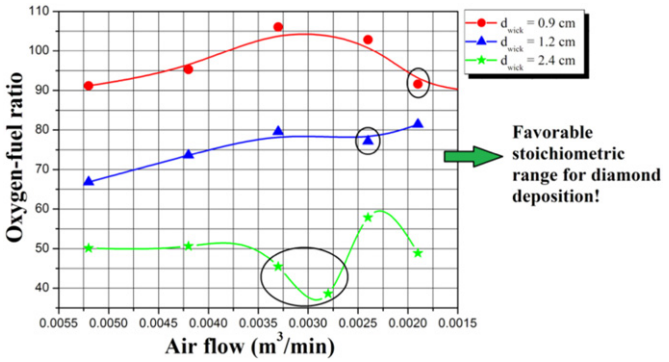

Fig. 10. Oxygen-fuel ratio towards the applied air flow and wick's surface area.

diamond formation from amorphous precursors, since this method requires high pressures and/or temperatures, which is inconsistent with the experimental conditions of diamond synthesis in this paper [45,46]. In addition, the results in Section 3.3 imply that the structural transition occurs in the flame. For instance, the incipiency of DLC outside the flame (i.e. on the substrate surface) is unlikely due to the necessity of substrate temperatures within ~500–750 °C [10]. These values are unachievable with our combustion system based on the thermal profiles in Fig. 9 and previously measured substrate temperatures [29]. If the carbon particles indeed undergo transformation on the substrate, then any variations in the substrate-to-burner distance *L* should cause the deposition of carbon nanostructures with different morphology [47]. Furthermore, it has been observed that diamond formation on solid substrates is strongly influenced by the deposition time *t* and the diamond peak in the Raman spectrum has been detected after prolonged and continuous deposition [17]. Since *L* and *t* are responsible for the quality and thickness of the material, and not for its physicochemical properties (see Section 3.3), the hypothesis for substrate-guided soot and DLC growth seems inapplicable to our particular conditions.

According to the fundamentals of combustion, the solid particulate matter formation begins with homogeneous nucleation of polycyclic aromatic hydrocarbons (PAHs) generated by thermal decomposition of the vaporized fuel (here, rapeseed oil) [44]. These PAHs pack together into hexagonal face-centered arrays, known as platelets, which further arrange in layers to form crystallites and the primary spherical soot particle (typically 10^3 crystallites per particle). The subsequent formation of larger particles and aggregates is governed by the interplay between several processes such as coalescence, coagulation, surface growth and aggregation [21–23]. Initially, the pristine soot particles collide to one another and coalesce completely at small scales (units of nm) [22]. As the size of secondary particles becomes significantly larger than that of the constituent primary particles, the coalescence is replaced by coagulation, followed by chain-like aggregation due to insufficient time for complete fusing [22]. The validity of this hypothesis is confirmed experimentally in Fig. 3a, as the SEM imaging shows a fractal-like network of quasispherical soot particles with approximate size of 50 nm, exceeding by a factor of ~25 the size of pristine particulate [44]. Since the overall process has duration of a few milliseconds, a detailed modeling shows an equal growth rate for the candidate and already aggregated particles. Hence, the models suggest simultaneous occurrence of nucleation, surface growth and aggregation [21,22].

On the other hand, the particles' morphology is strongly influenced by the nucleation rate that depends on the oxygen-fuel ratio and its manipulation can trigger a transition from coalescent to aggregate particle growth [21]. At low rates and constant surface growth, the aggregated particles acquire a spherical shape, while at intensive nucleation the degree of particle overlapping increases significantly [21]. In fact, an experimental study of post-flame soot particles in laminar diffusion flames shows a remarkable similarity of the soot's morphology at low oxygen-ethene ratio with that illustrated in Fig. 3c [48]. Unfortunately, the authors do not disclose any data regarding the ratio of chemical bonds in the soot; therefore, it is impossible to establish full correlation between their and our findings. Moreover, the relevant numerical models do not account for possible structural alterations in the pristine particles (sp^2/sp^3 ratio, for instance), caused by changes in the oxygen-fuel ratio and subsequently the nucleation rate [21–23]. However, a study of the early history of soot formation from various hydrocarbon diffusion flames shows that the soot's structure and morphology could be manipulated depending on the fuel's chemistry and distance between the exit port and collecting substrate [47]. Surprisingly, and in line with our observations, the earliest deposits from benzene (aromatic molecule) are of non-aromatic nature [47]. These results support the hypothesis that at certain reaction kinetics an aromatic molecule (e.g. the PAHs that nucleate as conventional quasispherical soot) can be transformed into a non-aromatic one (e.g. non-aromatic grain-like clusters of DLC).

Although there is a lack of a numerical model that may complement the experimental data, we believe that the morphological modifications and the corresponding changes in sp^2/sp^3 content are closely linked to variations in the reaction kinetics. For instance, during the first stage of collision, the primary solid particles collide and completely coalesce, but this event occurs at a certain kinetic energy of the gas flow. Since from thermodynamic point-of-view this energy depends on the gas temperature i.e. the flame/fume temperature, one can assume with sufficient conviction that cooler flames will possess lower kinetic energy and the gas molecules (the PAHs) along with the nucleated particles will undergo elastic collisions with reduced velocity and magnitude. Thereby, we hypothesize that the strength of elastic impact is governed by the particles' kinetic energy and their morphology, and structure are determined by the current impact conditions. In this research, the air flow and wick's dimensions are mainly responsible for the values of oxygen-fuel ratio and flame temperature, thus, for the magnitude of subsequent elastic collisions within the flame/gas flow and the transformation of pristine soot to DLC. These speculations correlate well with the proposed nonequilibrium route to nanodiamond formation, where the authors demonstrate that carbon onions can directly be transformed into nanodiamond by kinetically driven mechanism [36]. Identically to our results, carbon onion to nanodiamond conversion is highly successful in a narrow range of incident energies (in our case, specific oxygen-fuel ratio and flame temperature) and beyond that the impact energy is either insufficient to overcome the barrier between sp^2 and sp^3 bonding or high enough to destroy the crystalline region [36].

Of course, the above considerations may raise additional questions regarding the probability of diamond formation simultaneously with the soot rather than a subsequent transformation [32,33] or concerns related with the effect of fuel's chemistry on the particles' morphology and structure [47]. If diamond forms along with the soot, at least a small portion of diamond-like carbon and/or nanodiamond should be available in the final structure deposited at an open flame (no funnel). The coating at this regime is typical superhydrophobic carbon soot with undetectable diamond phase (on a macro and micro scale). In fact, diamond in a candle flame is captured via anodic aluminum oxide foils, ensuring “original state” of the particles at the collecting position [32]. Furthermore, along with nanodiamonds, graphite, fullerenes and amorphous carbon are identified based on the chosen flame region [32]. It is well known that each flame region has a different temperature; therefore, we assume that various carbon particles are collected simply because the kinetics at each region is different. Also, even if the formation is simultaneous, the average candle flame temperature is ~1400 °C [18], which is ~2.4 times higher temperature in comparison with that of the burning rapeseed oil. Thus, the candle might be able of supporting “local” thermodynamic phase transition of the nucleated particles within the flame. On the other hand, the concern about the fuel's chemistry is interesting and relevant. The results in this research might be achievable only with a limited number of hydrocarbon precursors, since various fuels decompose differently due to their chemical bonds and composition. As a consequence, the energy released during the initial phase of thermal decomposition and the subsequent flame temperature and reaction kinetics might vary from fuel to fuel, which would affect the particles' formation. The above question is a subject of fundamental importance and requires thorough and detailed theoretical and experimental investigations that are not in the scope of the present article, but will be planned as a future work.

4. Conclusions

In this study, we considered the formation mechanism of graphite-like and diamond-like nanostructures in low temperature laminar diffusion flames. An enhanced combustion system, composed of an inverted tin funnel connected to a flow meter and an air pump, was used to manipulate *in-situ* the incomplete combustion of a cylindrical paper wick immersed in rapeseed oil. The morphological and structural analysis of the as synthesized materials showed the precipitation of either carbon soot or DLC. Furthermore, the flame temperature profiles and the oxygen-fuel ratios, for the chosen combustion conditions, revealed that the DLC nanostructures could be generated only in a narrow stoichiometric range and T_{flame} ~ 210–260 °C. Beyond that, the carbon nanoparticles were associated with conventional (spherical), mixed or modified (quasisquare shaped) soot. These observations suggested a novel principle of graphite and diamond growth in flames, related with alteration of the reaction kinetics during the combustion process. Our hypotheses correlated partially with the kinetic models of soot formation in flames and were also supported by the recently disclosed nonequilibrium route for nanodiamond formation. We believe that the considered formation mechanism, although speculative to a certain extent, provides new and important information about the fundamentals of combustion and may be used as a benchmark for further development of detailed numerical models.

Future work

The future research activities encompass the usage of fuels with different physicochemical properties (chemical composition, flash point, density, viscosity, etc.) in order to assess their influence on the structure and morphology of the generated carbon nanostructures. Also, a comprehensive numerical model that will further enlighten on the reaction kinetics during diamond and graphite synthesis in low temperature diffusion flames is required.

Acknowledgments

The authors wish to acknowledge the VCU's Nanomaterials Core Characterization Facility for providing access to the surface characterization equipment. Also, the startup support from Virginia Commonwealth University under grant 137422 is greatly acknowledged.

References

[1] S.H. Friedman, The four worlds of carbon, Nat. Chem. 4 (2012) 426.
[2] O.A. Williams, Nanocrystalline diamond, Diam. Relat. Mater. 20 (2011) 621–640.
[3] V.V. Danilenko, On the history of the discovery of nanodiamond synthesis, Phys. Solid State 46 (2004) 595–599.
[4] R.J. Nemanich, J.A. Carlisle, A. Hirata, K. Haenen, CVD diamond- research, applications and challenges, MRS Bull. 39 (2014) 490–494.
[5] S.S. Yap, W.O. Siew, C.H. Nee, T.Y. Tou, Parametric studies of diamond-like carbon by pulsed Nd: YAG laser deposition, Diam. Relat. Mater. 20 (2011) 294–298.
[6] I. Kumar, A. Khare, Multi- and few-layer graphene on insulating substrate via pulsed laser deposition technique, Appl. Surf. Sci. 317 (2014) 1004–1009.
[7] J. Zemek, P. Jiricek, J. Houdkova, A. Artemenko, M. Jelinek, Diamond-like carbon and nanocrystalline diamond film surfaces sputtered by argon cluster ion beams, Diam. Relat. Mater. 68 (2016) 37–41.
[8] Z. Wu, X. Tian, G. Gui, C. Gong, S. Yang, P.K. Chu, Microstructure and surface properties of chromium-doped diamond-like carbon thin films fabricated by high power pulsed magnetron sputtering, Appl. Surf. Sci. 276 (2013) 31–36.
[9] A.N. Yurkov, N.N. Melnik, V.V. Sychev, V.V. Savranskii, D.V. Vlasov, V.I. Konov, Synthesis of carbon films by magnetron sputtering of a graphite target using hydrogen as plasma-forming gas, Bull. Lebedev Phys. Inst. 38 (2011) 263.
[10] Y. Hirose, S. Amanuma, K. Komaki, The synthesis of high quality diamond in combustion flames, J. Appl. Phys. 68 (1990) 6401–6405.
[11] I. Doi, M.S. Haga, Y.E. Nagai, Properties of DLC films deposited by an oxyacetylene flame, Diam. Relat. Mater. 8 (1999) 1682–1685.
[12] J.B. Donnet, H. Oulanti, T.L. Huu, M. Schmitt, Synthesis of large single crystal diamond using combustion flame method, Carbon 44 (2006) 374–380.
[13] N.K. Memon, S.D. Tse, J.F. Al-Sharab, H. Yamaguchi, A.B. Goncalves, et al., Flame synthesis of graphene films in open environments, Carbon 49 (2011) 5064–5070.
[14] H. Zhu, T. Kuang, B. Zhu, S. Lei, Z. Liu, S.P. Ringer, Flame synthesis of carbon nanostructures Ni-plated hardmetal substrates, Nanoscale Res. Lett. 6 (2011) 331.
[15] K.L. Yarina, D.S. Dandy, E. Jensen, J.E. Butler, Growth of diamond films using an enclosed methyl-acetylene and propadiene combustion flame, Diam. Relat. Mater. 7 (1998) 1491–1502.
[16] K.D. Esmeryan, C.E. Castano, A.H. Bressler, M. Abolghasemibizaki, R. Mohammadi, Rapid synthesis of inherently robust and stable superhydrophobic carbon soot coatings, Appl. Surf. Sci. 369 (2016) 341–347.
[17] U. Bergmann, K. Lummer, B. Atakan, K.K. Höinghaus, Flame deposition of diamond films: an experimental study of the effects of stoichiometry, temperature, time and the influence of acetone, Ber. Bunsenges. Phys. Chem. 102 (1998) 906–914.

[18] V. Babrauskas, Temperatures in Flames and Fires, www.doctorfire.com/flametmp.html. Last access: October 25, 2016.
[19] J.J. Schermer, W.A.L.M. Elst, L.J. Giling, The influence of differences in gas phase between turbulent and laminar acetylene-oxygen combustion flames on diamond growth, Diam. Relat. Mater. 4 (1995) 1113–1125.
[20] F. Ossler, S.E. Canton, J. Larsson, X-ray scattering studies of the generation of carbon nanoparticles in flames and their transition from gas phase to condensed phase, Carbon 47 (2009) 3498–3507.
[21] M. Balthasar, M. Frenklach, Detailed kinetic modeling of soot aggregate formation in laminar premixed flames, Combust. Flame 140 (2005) 130–145.
[22] P. Mitchell, M. Frenklach, Particle aggregation with simultaneous surface growth, Phys. Rev. E 67 (2003) 061407.
[23] N. Morgan, M. Kraft, M. Balthasar, D. Wong, M. Frenklach, P. Mitchell, Numerical simulations of soot aggregation in premixed laminar flames, Proc. Combust. Inst. 31 (2007) 693–700.
[24] T.S. Totton, D. Chakrabarti, A.J. Misquitta, M. Sander, D.J. Wales, M. Kraft, Modelling the internal structure of nascent soot particles, Combust. Flame 157 (2010) 909–914.
[25] T.S. Totton, A.J. Misquitta, M. Kraft, A quantitative study of the clustering of polycyclic aromatic hydrocarbons at high temperatures, Phys. Chem. Chem. Phys. 14 (2012) 4081–4094.
[26] F. Ossler, L. Vallenhag, S.E. Canton, J.B.A. Mitchell, J.L. Garrec, et al., Dynamics of incipient carbon particle formation in a stabilized ethylene flame by in situ extended-small-angle and wide-angle X-ray scattering, Carbon 51 (2013) 1–19.
[27] M. Okkerse, C.R. Kleijn, H.E.A. van der Akker, M.H.J.M. de Croon, G.B. Marin, Two-dimensional simulation of an oxy-acetylene torch diamond reactor with a detailed gas-phase and surface mechanism, J. Appl. Phys. 88 (2000) 4417.
[28] K.K. Höinghaus, A. Löwe, B. Atakan, Investigations of the gas phase mechanism of diamond deposition in combustion CVD, Thin Solid Films 368 (2000) 185–192.
[29] K.D. Esmeryan, C.E. Castano, A.H. Bressler, C.P. Fergusson, R. Mohammadi, Single-step flame synthesis of carbon nanoparticles with tunable structure and chemical reactivity, RSC Adv. 6 (2016) 61620–61629.
[30] R.Z. Khaliullin, H. Eshet, T.D. Kühne, J. Behler, M. Parrinello, Nucleation mechanism for the direct graphite-to-diamond phase transition, Nat. Mater. 10 (2011) 693–697.
[31] V.N. Mochalin, O. Shenderova, D. Ho, Y. Gogotsi, The properties and applications of nanodiamonds, Nat. Nanotechnol. 7 (2012) 11–23.
[32] Z. Su, W. Zhou, Y. Zhang, New insights into the soot nanoparticles in a candle flame, Chem. Commun. 47 (2011) 4700–4702.
[33] W.Z. Zhou, F.J. Yu, H.F. Greer, Z. Jiang, P.P. Edwards, Electron microscopic studies of growth of nanoscale catalysts and soot particles in a candle flame, Appl. Petrochem. Res. 2 (2012) 15–21.
[34] M. Choucair, J.A. Stride, The gram-scale synthesis of carbon onions, Carbon 50 (2012) 1109–1115.
[35] J.C. Vinci, L.A. Colon, Fractionation of carbon-based nanomaterials by anion-exchange HPLC, Anal. Chem. 84 (2012) 1178–1183.
[36] N.A. Marks, M. Lattemann, D.R. McKenzie, Nonequilibrium route to nanodiamond with astrophysical implications, Phys. Rev. Lett. 108 (2012) 075503.
[37] G. Anastopoulos, Y. Zannikou, S. Stournas, S. Kalligeros, Transesterification of vegetable oils with ethanol and characterization of the key fuel properties of ethyl esters, Energies 2 (2009) 362–376.
[38] K.D. Esmeryan, E.I. Radeva, I.D. Avramov, Durable superhydrophobic carbon soot coatings for sensor applications, J. Phys. D. Appl. Phys. 49 (2016) 025309.
[39] A. Sadezky, H. Muchkenhuber, H. Grothe, R. Niessner, U. Pöschl, Raman microspectroscopy of soot and related carbonaceous materials: spectral analysis and structural information, Carbon 43 (2005) 1731–1742.
[40] A.C. Ferrari, J. Robertson, Interpretation of Raman spectra of disordered and amorphous carbon, Phys. Rev. B 61 (2000) 14095–14107.
[41] A. Kumar, P.A. Lin, A. Xue, B. Hao, Y.K. Yap, R.M. Sankaran, Formation of nanodiamonds at near-ambient conditions via microplasma dissociation of ethanol vapour, Nat. Commun. 4 (2013) 2618.
[42] R. Sonnier, B. Otazaghine, L. Ferry, J.M.L. Cuesta, Study of the combustion efficiency of polymers using a pyrolysis-combustion flow calorimeter, Combust. Flame 160 (2013) 2182–2193.
[43] T.X. Li, K. Kuwana, K. Saito, H. Zhang, Z. Chen, Temperature and carbon source effects on methane-air flame synthesis of CNTs, Proc. Combust. Inst. 32 (2009) 1855–1861.
[44] O.I. Smith, Fundamentals of soot formation in flames with application to diesel engine particulate emissions, Prog. Energy Combust. Sci. 7 (1981) 275–291.
[45] K. Higashi, A. Onodera, Non-catalytic synthesis of diamond from amorphous carbon at high static pressure, Physica B+C 139–140 (1986) 813–815.
[46] J. Zhang, V. Prakapenka, A. Kubo, A. Kavner, H.W. Green, L.F. Dobrzhinetskaya, Diamond formation from amorphous carbon and graphite in the presence of COH fluids: an *in situ* high-pressure and -temperature laser-heated diamond anvil cell experimental study, in: L. Dobrzhinetskaya, S.W. Fariad, S. Wallis, S. Cuthbert (Eds.), Ultrahigh-pressure Metamorphism, Elsevier 2007, pp. 113–124.
[47] K. Saito, A.S. Gordon, F.A. Williams, W.F. Stickle, A study of the early history of soot formation in various hydrocarbon diffusion flames, Combust. Sci. Technol. 80 (1991) 103–119.
[48] J.F. Widmann, J.C. Yang, T.J. Smith, S.L. Manzello, G.W. Mulholland, Measurement of the optical extinction coefficients of post-flame soot in the infrared, Combust. Flame 134 (2003) 119–129.

Applied Surface Science 390 (2016) 452–460

Contents lists available at ScienceDirect

Applied Surface Science

journal homepage: www.elsevier.com/locate/apsusc

Rational strategy for the atmospheric icing prevention based on chemically functionalized carbon soot coatings

Karekin D. Esmeryan[a,b], Ashton H. Bressler[a], Carlos E. Castano[a,c], Christian P. Fergusson[a], Reza Mohammadi[a,*]

[a] Department of Mechanical and Nuclear Engineering, Virginia Commonwealth University, Richmond, VA, 23284, USA
[b] Georgi Nadjakov Institute of Solid State Physics, 72, Tzarigradsko Chaussee Blvd., 1784 Sofia, Bulgaria
[c] Nanomaterials Core Characterization Facility, Department of Chemical and Life Science Engineering, Virginia Commonwealth University, Richmond, VA, 23284, USA

ARTICLE INFO

Article history:
Received 16 June 2016
Received in revised form 12 August 2016
Accepted 20 August 2016
Available online 28 August 2016

Keywords:
Anti-icing
Carbon soot
Freezing time
Icephobicity
Impact dynamics
Superhydrophobicity

ABSTRACT

Although the superhydrophobic surfaces are preferable for passive anti-icing systems, as they provide water shedding before initiation of ice nucleation, their practical usage is still under debate. This is so, as the superhydrophobic materials are not necessarily icephobic and most of the synthesis techniques are characterized with low fabrication scalability. Here, we describe a rational strategy for the atmospheric icing prevention, based on chemically functionalized carbon soot, suitable for large-scale fabrication of superhydrophobic coatings that exhibit and retain icephobicity in harsh operational conditions. This is achieved through a secondary treatment with ethanol and aqueous fluorocarbon solution, which improves the coating's mechanical strength without altering its water repellency. Subsequent experimental analyses on the impact dynamics of icy water droplets on soot coated aluminum and steel sheets show that these surfaces remain icephobic in condensate environments and substrate temperatures down to −35 °C. Furthermore, the soot's icephobicity and non-wettability are retained in multiple icing/de-icing cycles and upon compressed air scavenging, spinning and water jetting with impact velocity of ∼25 m/s. Finally, on frosted soot surfaces, the droplets freeze in a spherical shape and are entirely detached by adding small amount of thermal energy, indicating lower ice adhesion compared to the uncoated metal substrates.

1. Introduction

The atmospheric icing is a natural phenomenon that occurs when supercooled water droplets in the atmosphere freeze upon impact on solid objects [1]. Supercooling is a process of lowering the temperature of a liquid below its freezing point, without triggering a phase transition to a solid [2]. Normally, the water freezes around 0 °C, but in certain circumstances (high purity or lack of nucleation sites) it could be supercooled down to its homogeneous nucleation temperature (-48.3 °C) [3]. In turn, the supercooled water droplets could freeze almost instantly (units of seconds) upon contact with a solid surface, which may lead to catastrophic socioeconomic consequences. For instance, even a thin ice layer is sufficient to destroy the high-voltage power lines or telecommunication networks, leaving hundreds of households with no electricity and telecommunications [4]. Furthermore, the ice accretion on the wings, propellers and rotor blades of the aircrafts can cause a loss of aerodynamics [5] or excessive vibrations due to imbalanced rotors [6] that sometimes lead to fatal accidents [7,8]. In addition, the icing of cold-region wind turbines degrades their operation efficiency and may reduce the energy production and lifetime of the turbine [9,10].

The most common strategies for icing protection include electro-thermal and mechanical systems, which use electric current or mechanical vibrations to suspend the accumulated ice [11]. However, the electro-thermal approach covers only the leading edge of the wing or rotor blade and requires materials with high thermal conductivity [11]. In turn, such systems are prone to "runback ice" formation and along with their bulkiness and cyclic operation (to reduce the power consumption) are economically inexpedient [11]. Furthermore, the efficient operation of mechanical systems is restricted by the elastic, dielectric or piezoelectric losses in the actuator, which reduces the overall mechanical stress applied to overcome the ice adhesion forces [12,13]. On

* Corresponding author.
E-mail address: rmohammadi@vcu.edu (R. Mohammadi).

http://dx.doi.org/10.1016/j.apsusc.2016.08.101
0169-4332/

the other hand, the usage of chemical reagents for icing mitigation or prevention has the advantage of being passive (no external power required) and therefore, a low weight and reliable technique. Various chemicals are incorporated into coatings with an aim to dissolve the incipient ice, but some of them can corrode the protected surface and need to be monitored and replaced frequently [14].

Alternatively, the interest in superhydrophobic materials as passive anti-icing systems has rapidly increased over the past decade [15–18]. The concept of icephobicity of the superhydrophobic surfaces relies on their extreme non-wettability upon contact with water, as well as the ability to promote rebound of the impacting liquid droplets [19]. It has been argued that the impingement of water droplets on superhydrophobic surfaces leads to a transfer between the kinetic and surface energy of the liquid and subsequent droplet rebound [20]. As a result, the solid-liquid contact time decreases down to a few milliseconds, hence, the exchanged thermal energy is insufficient to trigger nucleation and the water is shed-off before freezing. Moreover, the suspended Cassie-Baxter state of the superhydrophobic materials minimizes the solid-liquid contact area, thereby reduces the heat transfer rate and the icing probability, which is a function of the surface area and wettability [21–23]. Furthermore, even if nucleation occurs, the air trapped at the solid-liquid interface reduces the actual ice-coated surface area and disrupts the bonding by creating stress concentrations [16]. Thus, the ice adhesion forces are significantly weakened, which decreases up to 80% the amount of energy required to keep the protected surface free of ice [19].

Although superhydrophobic surfaces (coatings) are very promising for passive icing protection, their applicability is yet under debate, because of several important technological factors. Firstly, by definition the terms “superhydrophobicity” and “icephobicity” are different, and as stated elsewhere not every superhydrophobic surface (coating) can exhibit icephobicity [24,25]. The reason is that the critical size of the particles that makeup the surface is in different length scales for superhydrophobicity and icephobicity [24]. For instance, ice does not form on surfaces coated with organosilane-modified silica particles with diameters between 20 and 50 nm; however, the icing probability increases remarkably when the particle diameter is larger than 50 nm [24]. Despite that, the same surfaces support superhydrophobicity in the entire range of particle sizes. Also, the water and ice adhere differently to the substrate, as the force needed to detach a water droplet depends on the contact angle hysteresis, while the force required to detach a piece of ice depends on the receding contact angle and the initial size of interfacial cracks [25]. Secondly, the humid environments introduce a major challenge to the usage of superhydrophobic surfaces, as the water vapor may condense both on top and between the surface asperities, causing frost formation and freezing of the impacting water droplets [1,26]. Thirdly, some superhydrophobic surfaces cannot withstand harsh operational conditions (heavy rains, gusty winds, sand particles, thermal drifts, multiple icing/de-icing cycles, etc.) and their icephobicity is degraded after a few experimental tests [27,28]. Finally, even if the above mentioned shortcomings are circumvented, most of the available synthesis techniques are characterized with low fabrication scalability (e.g. efficiency only at small scales, high cost, etc.) [28]. The latter is of crucial importance for the industrial applicability of the icephobic/superhydrophobic materials and as mentioned elsewhere, the problem of fabrication scalability and the good degree of robustness have received less attention in the literature to date, and they need to become a research priority [28]. There are some investigations in regard to the mechanical durability of the superhydrophobic coatings [29,30], but most of the approaches do not comply with the requirement for high fabrication scalability.

Therefore, the emphasis of this paper is on the anti-icing performance of chemically functionalized carbon soot coatings that are suitable for large-scale fabrication of durable icephobic surfaces. Inspired from our recent technology for synthesis of inherently robust soot coatings [31] and the possibility to reinstate their water repellency through a secondary treatment with fluorocarbon solution [32], we demonstrate that after functionalization with ethanol and fluorocarbon the mechanical strength and surface adhesion of the soot are significantly improved. Thus, the major advantage of the as prepared coatings is related with their ability to exhibit icephobicity in multiple icing/de-icing cycles in cold humid environments. In addition, the soot coated surfaces are capable of retaining their non-wetting properties upon simulation of harsh operational conditions such as gusty winds, heavy rains or high rotational velocities. Herein, the proposed technique is characterized with high fabrication scalability, as it is time-efficient (icephobic coatings can be fabricated within a few minutes), inexpensive (compared to most of the available methods), suitable for large-scale objects and highly reproducible.

2. Methods

2.1. Chemical functionalization of the carbon soot coatings

The model substrates were prepared by cutting 3 mm thick sheets of aluminum (6061) and steel (1018) alloys (McMaster-Carr) into 25 × 25 mm squares. All samples were cleaned with acetone (99%, Sigma-Aldrich) and coated with carbon soot by exposing them for 20 s over a black fume released from a conical chimney, used to manipulate the combustion process of rapeseed oil [31]. Afterwards, each sample was gently immersed in ethanol (99%, Sigma-Aldrich) for 5 s and dried for 2 min at 100 °C using a hot plate. Subsequently, the substrates were treated with fluorocarbon solution (Grangers Performance Proofer, UK) designed for waterproof breathable fabrics. The chemical emulsion, which is mainly composed of a block copolymer of perfluorocarbon and polyvinylalcohol [33], was diluted in de-ionized water by a factor of 7 and the samples were immersed in it for 10 min at room temperature. Finally, each substrate was dried for 3 min at 100 °C in order to remove the excessive chemical residues.

2.2. Surface characterization and wettability

The morphology and surface roughness of the soot coated substrates prior to and after chemical functionalization were examined using scanning electron microscopy (SEM) and atomic force microscopy (AFM). The SEM experiments were performed using a Hitachi SU-70 Field Emission Scanning Electron Microscope and images were taken with magnifications up to 50k, while the AFM images were obtained in tapping mode with Bruker BioScope Catalyst for an area of 1 × 1 μm at a rate of 0.4 Hz. The chemical composition of the coatings was investigated qualitatively by energy dispersive spectroscopy (EDS) at 15 KeV using an EDAX detector with an active area of 10 mm^2. The surface wettability of the samples was determined through static contact angle (SCA) and contact angle hysteresis (CAH) measurements for 3 μl droplets of de-ionized water by using a Drop Shape Analyzer (DSA 25E, Krüss Germany).

2.3. Icing experiments

The system for these experiments was based on a Summit VLT650 Laboratory Upright Freezer, depicted in Fig. 1. The door of the freezer was replaced with 50 mm thick polystyrene foam, in the middle of which a 150 × 300 mm window of polished acrylic plate was installed. A wood platform, used as a sample holder, was placed inside the freezer and its tilt angle was manipulated through an MG 995 servo motor. This process was controlled with ±0.2° accuracy

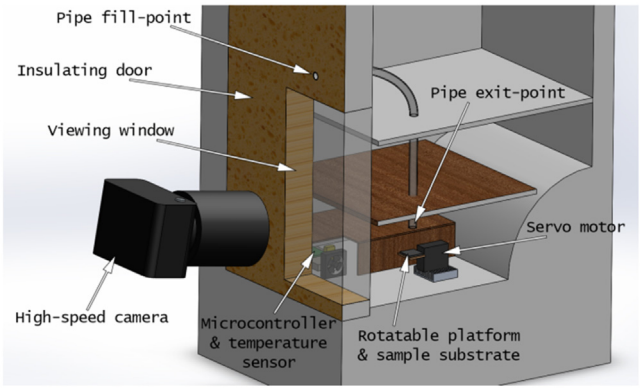

Fig. 1. Scheme of the experimental setup.

by an Arduino Micro Controller linked to a laptop. In addition, a second controller was used to measure the temperature levels, which were displayed on a 40 mm screen. All electronic components were powered by a modular 450 W computer power supply.

Initially, uncoated, as well as soot coated aluminum and steel sheets were mounted one at a time on the holder and positioned at fixed tilt angles (θ = 0, 10, 30 and 50°). Subsequently, 200 μl of icy water (~0 °C) were dropped on the samples through a plastic capillary tube and the incoming water flow was controlled using a rubber dust blower (known also as air ball). In fact, depending on the applied mechanical force, the air ball was capable of creating water droplets with relatively equal size and impact velocity. Therefore, icy water droplets with various diameters in the range of 1–8 mm were formed at the tip of the tube and impinged on the sample's surface from a fixed distance of 70 mm. The tests were done at impact velocities within 1–5 m/s, corresponding to droplet dynamics at Weber and Reynolds numbers of *We* ~14-897 and *Re* ~560–10717, respectively. The maximum values of *We* and *Re* were calculated at impact velocity of 3.42 m/s and droplet diameter of 5.6 mm, since this was the optimal/highest experimentally observed combination of both parameters. For each set of tilt angles, the substrate temperature (T_{sub}) was varied in the range of −25 °C to −35 °C with a step of 5 °C. This thermal range was chosen based on the average air temperatures for altitudes, at which an aircraft could encounter icing clouds and also due to the cooling threshold of the freezer (−37 °C). Furthermore, these temperatures are very common in some regions on the earth, which may compromise the performance of cold-region wind turbines. In addition, the relative humidity in the chamber was measured by a DHT 22 humidity sensor and kept close to saturation (~100%) through a tank full with de-ionized water. During the experiments, the impact dynamics of the droplets, as they impinge on the target substrate, was captured by means of a Phantom Miro eX2 high speed camera with a resolution up to 7400 frames/s. The retraction velocity (V_{ret}), solid-liquid contact time (t_{sl}) and the subsequent freezing time (t_{freez}), if ice nucleation occurs, were determined via PCC 2.5 (Phantom Camera Control) commercial computer software.

3. Results and discussion

3.1. Morphology and surface adhesion of the carbon soot coatings prior to and after chemical functionalization

Although the surfaces made of carbon soot exhibit extreme water repellency, their anti-icing properties have not been studied yet, as the bonds between the individual nanoparticles are weak, leading to inherent brittleness of the non-modified material and inability of the chimney-modified soot to retain its non-wettability upon harsh operational conditions [31,34,35]. To address these limitation, we have developed a method for chemical functionalization of the soot that enhances its robustness and surface adhesion under harsh operational conditions. Fig. 2 reveals the structure and morphology of the carbon soot, deposited on aluminum (Al) and steel substrates using the chimney method [31], before and after treatment with ethanol and aqueous fluorocarbon solution. It seems that regardless of the chemical functionalization, the soot's amorphous structure composed of tightly bonded and elongated nanoparticles

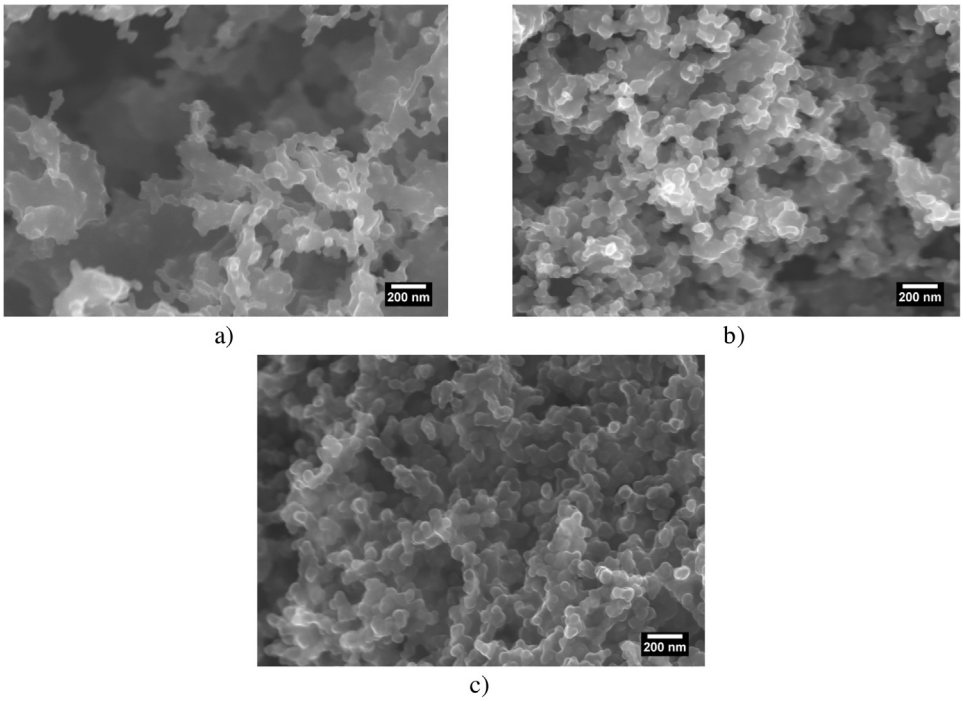

Fig. 2. Scanning electron micrographs of the structure and morphology of the chimney modified carbon soot a) prior to and after treatment with b) ethanol and c) aqueous fluorocarbon solution.

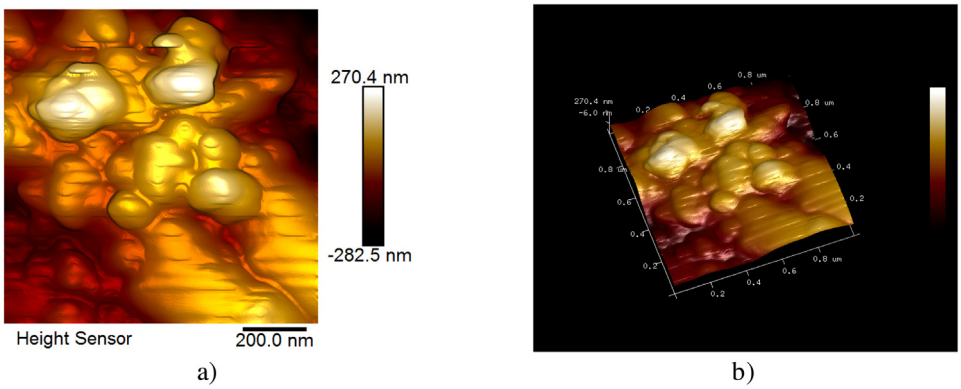

Fig. 3. a) 2-D and b) 3-D AFM images of carbon soot treated with ethanol.

with an average size of ~60 nm remains unaltered. Prior to ethanol treatment, the soot coating is extremely water repellent with SCA and CAH being ~155° and 1°, respectively.

However, as seen in Fig. 2b), upon immersion in ethanol, the overall area of micro- and nanoscale cavities decreases significantly. Furthermore, at this stage the surface is characterized with a high SCA of 155° ± 2°, accompanied by dramatically increased CAH of 15° ±3°. These results clearly indicate Cassie-Baxter to Wenzel state transition, where the water droplets still may acquire a spherical shape, but are immobilized and unable to roll-off [32]. To correlate the observed wetting transition with possible changes in the surface topography, we examined the ethanol treated coating by atomic force microscopy, the results of which are shown in Fig. 3. The average root mean square roughness (R_{rms}) of the chimney modified soot is around 100 nm [31], while after immersion in ethanol the it decreases to about 80 nm, meaning that the peak features become more rounded, as suggested in ref. [32].

The reduced surface roughness and porosity of the soot imply that the ethanol reacts with the oxygen sites still present in the soot, promoting partial breaking of the exsiting bonds and leading to denser and well adhered structures. Although the physicochemical nature of these interactions is poorly addressed in the literature, we assume that the enhanced adhesion of the soot could be a consequence of the increased amount of sp^3 bonds in the coating, due to the specific deposition process [31], that along with the reduced porosity strengthen the links between the nanoparticles. In addition, the ethanol increases the total fraction of solid in contact with the water, which accounts for the increased CAH. Subsequent treatment of the surface with fluorocarbon recovers the mobility of water droplets and the CAH decreases to 0.8° ± 0.3°. Such a phenomenon is associated with the formation of a thin (~nm) hydrophobic layer on top of the soot, as indicated by the presence of ~4 at.% fluorine on the surface, depicted in Fig. 4.

A comparison between Fig. 2b) and c) shows that the fluorine-based treatment does not significantly alter the surface topography and only a slight (<5 nm) increase in the particle size is observed. This suggests the formation of a very conformal fluorine-based coating with a thickness of a few nanometers that along with the (R_{rms}) of ~80 nm reinstates its water repellency. Similar observation has been reported for SU-8 photoresist based patterns immersed in aqueous fluorocarbon solutions [36]. To verify the enhanced surface adhesion of the functionalized soot, and hence its potential to withstand harsh operational conditions, the coatings' integrity and wettability were tested after compressed air scavenging with an air velocity of ~340 m/s and spinning at rotational velocities up to 10 000 rpm. In both cases, the coating kept its integrity and superhydrophobic behavior (supporting Figs. S1, S2 and videos S1, S2). The surface adhesion of non-functionalized and fluorocarbon-modified soot coatings (lack of ethanol) was examined as well, with an aim to clarify whether the ethanol promotes the enhanced adhesion and robustness of the soot. The coatings with no alcohol treatment were easily peeled-off during the air scavenging; thus, indicating that the improved adhesion can be mainly associated with the impact of ethanol (supporting videos S3 and S4). The above experimental observations suggest that the chemically functionalized soot would be capable of withstanding gusty winds and high rotational velocities if intended to serve as protective coating for cold-region wind turbines.

3.2. Anti-icing performance of the functionalized soot coatings

After fabrication and functionalization, the anti-icing properties of as prepared soot coated Al and steel substrates were studied in detail. Uncoated Al and steel counterparts were used as a reference in order to assess the differences in droplet dynamics when the surface wettability changes from hydrophilic to superhydrophobic. The impact behavior of icy water droplets was investigated for different Weber and Reynolds numbers at sub-zero substrate temperatures (T_{sub}) and ~100%RH (see Methods for more information). As demonstrated in Fig. 5, for the uncoated sheets, the retraction after spreading is negligible and the maximum spreading diameter of the droplet (d_{spread}) is approximately equal to the maximum retraction diameter (d_{ret}) regardless of the substrate's tilt angle. This is expected since the hydrophilic substrates, such as Al or steel, ensure large surface area in contact with the liquid. Hence, the viscous forces and the friction at the solid-liquid contact area cause significant energy dissipation that reduces the remaining energy for recoil and the impinged water droplets freeze almost instantly [37].

Fig. 6 shows the relation between the freezing time of icy water droplets and the substrate temperature of uncoated Al and steel wafers.

As seen, the gradual reduction in the substrate temperature accelerates the nucleation and the freezing time (t_{freez}) decreases exponentially regardless of the chosen substrate. However, at −35 °C, the water droplets on bare Al wafer undergo crystal nucleation for ~0.15 s, while on the steel they nucleate within ~1.1 s, which shows that (t_{freez}) depends also on the thermal conductivity of the material. Similar trend of the droplets' freezing time is observed for the entire range of temperatures (−25 °C to −35 °C), which is in good agreement with the classical nucleation theory [38]. In addition, the retraction velocity (V_{ret}), determined through the time difference between the maximum spreading and retraction of the water droplet, decreases by reducing the substrate temperature. For an uncoated Al, V_{ret} ~0.073-0.037 m/s at −25 °C and −35 °C, respectively, while for the steel counterparts is ~0.16-

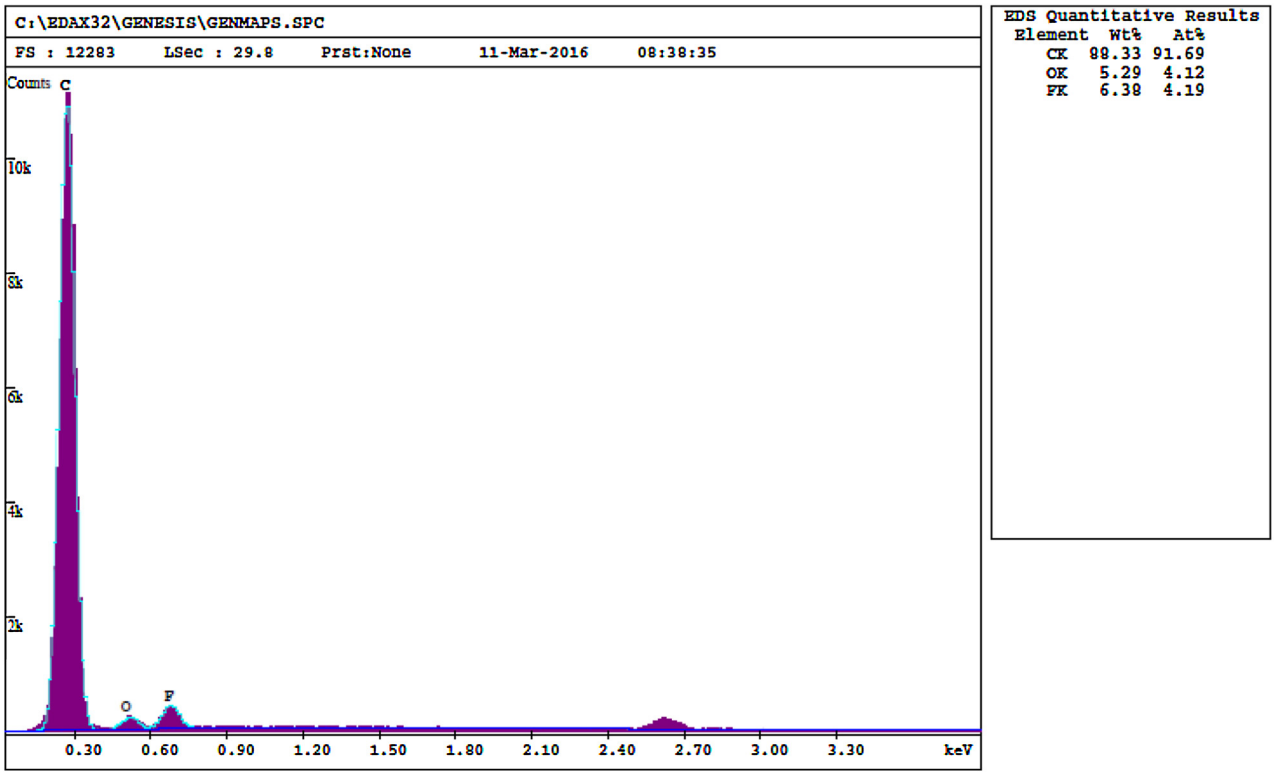

Fig. 4. Chemical composition of the functionalized soot based on EDS measurements.

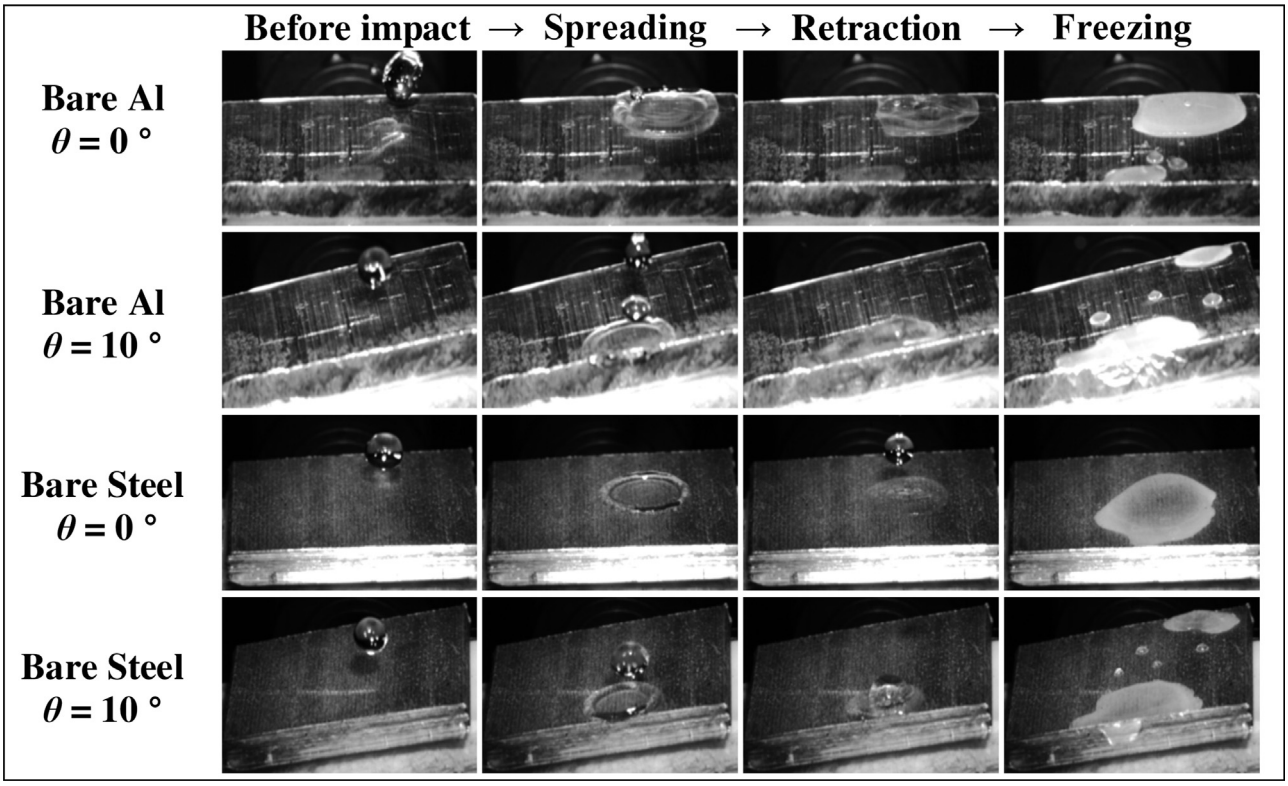

Fig. 5. Impact dynamics of icy water droplets impinging on horizontal and 10° tilted bare Al and steel substrates from a 70 mm height at T_{sub} = −35 °C and RH ~100%. The images are taken at 500 μs frame time and *We* ~16-80, *Re* ~698-2636.

0.055 m/s in the same thermal range. This effect is attributed to the increased losses of kinetic energy, resulting from the increased viscous shear and dissipation at the three-phase contact line [14].

In contrast, the droplet dynamics on soot coated superhydrophobic surfaces changes drastically. Complete retraction (d_{ret} = 0) followed by droplet rebound and/or splashing occurs in

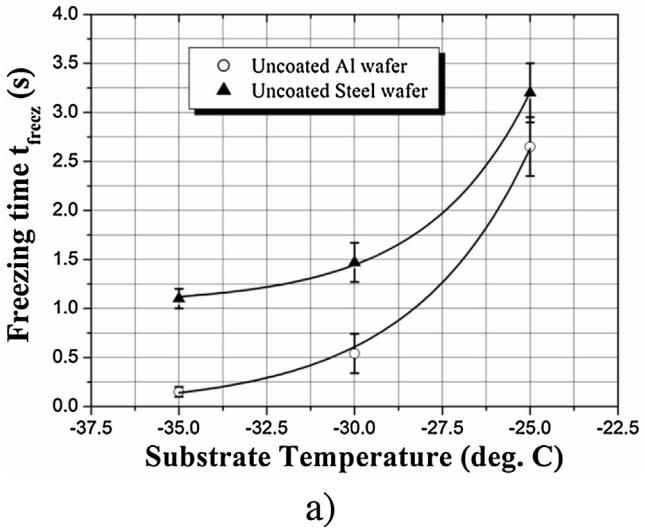

Fig. 6. Freezing time of icy water droplets as a function of the substrate temperature. The data plots are an average value of four independent measurements at tilt angles in the range of 0–50°. The solid lines represent the best fit curves of the experimental data.

the entire range of temperatures independent on the tilt angle of the substrate, as illustrated in Fig. 7. This complicated dynamic behavior of the droplets is guided by the competition between their inertial and capillary forces [39]. For the calculated Weber and Reynolds numbers ranging within *We* ~14-27 and *Re* ~560-1120, respectively, the droplets retract under the action of capillary forces, which tend to minimize the contact with the surface [39,40]. Since on superhydrophobic surfaces, in particular soot coated ones, the droplets behave as if on a frictionless surface [14]; their kinetic energy at impact is transformed into a surface energy, causing subsequent bounce-off [20]. As a result, the solid-liquid contact time is reduced to a few milliseconds (t_{sl} = 3–20 ms) and for the chosen range of substrate temperatures, the droplets shed-off before nucleation takes place.

Beyond the above mentioned values of *We* and *Re*, the initial kinetic energy is enough to overcome the capillary forces, which are unable to keep the integrity of the liquid on the surface and droplet splashing occurs. During the retraction phase, the droplets disintegrate into smaller satellites that jetting out from the outermost perimeter [39]. Despite that, the impacted surfaces remain completely free of ice in the entire range of substrate temperatures, demonstrating clearly the anti-icing properties of the chemically functionalized carbon soot coatings. Moreover, the soot retains icephobicity during the entire stage of icing experiments (12 cycles for Al and steel), confirming its strong potential for utilization in passive anti-icing systems.

3.3. Verification of the icing experiments with the kinetic model for three-dimensional heterogeneous nucleation

The remarkable icephobic behavior of the functionalized soot coatings can be explained through the kinetic model for three-dimensional heterogeneous nucleation used to explain the effect of the critical particle size of various composites on their icephobic properties [24,41]. According to this model, the kinetics of homogeneous nucleation is described by the nucleation rate (J), defined as the number of nuclei created per unit volume for a specific time (t). This rate (J) depends on the thermodynamic free energy barrier (ΔG_n^{homo}) and when the ice embryo formation occurs on solid surface i.e. heterogeneous nucleation, the energy barrier is reduced by a factor (f) ranging from 1 to 0:

$$\Delta G_n = \Delta G_n^{homo} f(m, x) \quad (1),$$

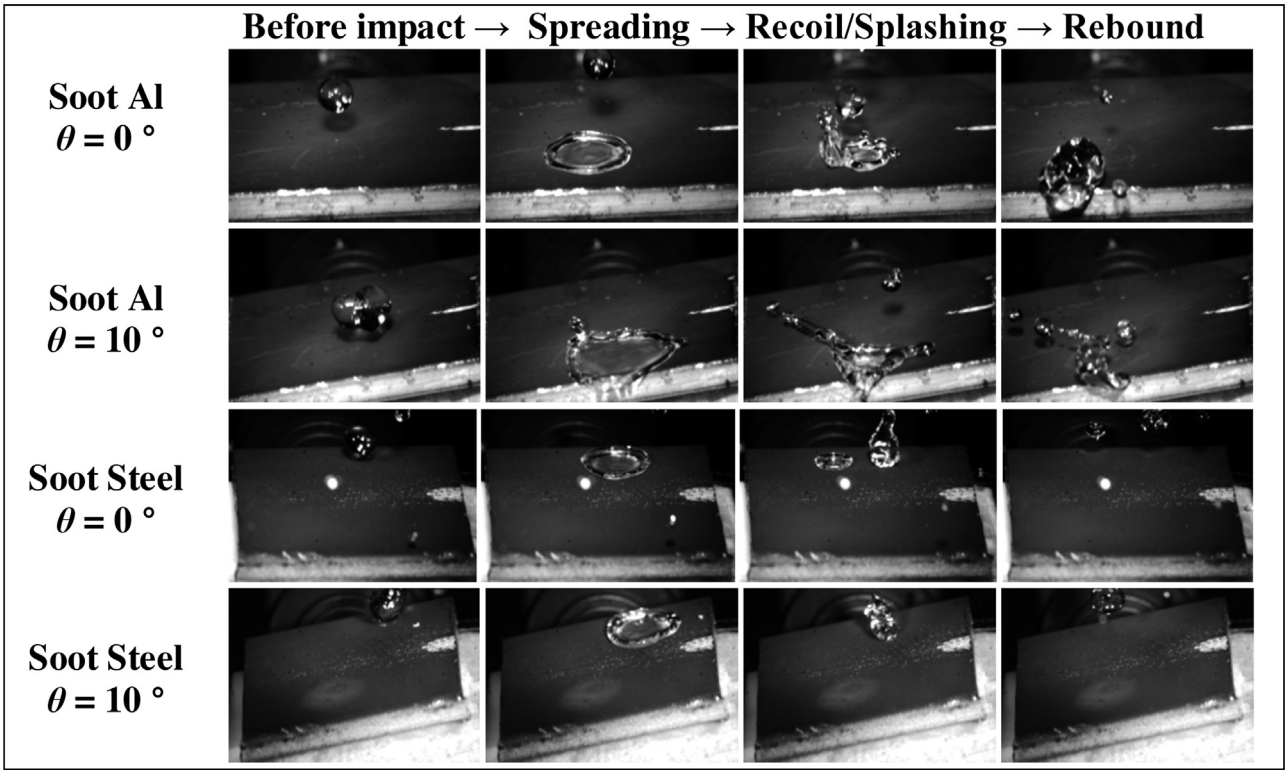

Fig. 7. Impact dynamics of icy water droplets impinging on horizontal and 10° tilted soot coated Al and steel substrates from a 70 mm height at T_{sub} = –30 °C and RH ~100%. The images are taken at 500 μs frame time and *We* ~14-213, *Re* ~560-5404.

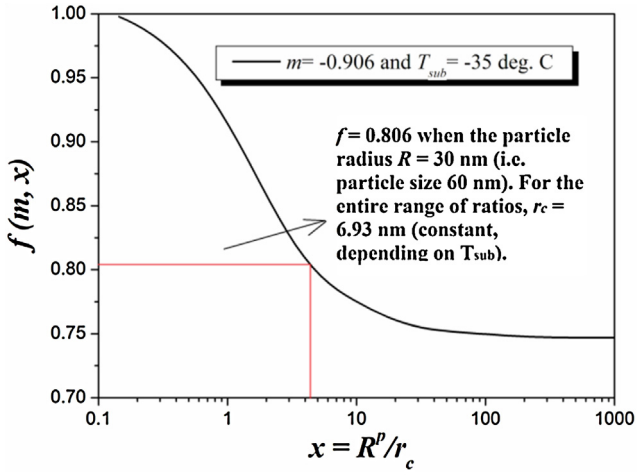

Fig. 8. Alteration of the reduction factor (f) as a function of the relative particle size (x) at T_{sub} = −35 °C and θ = 155° (m = −0.906).

where

$$f(m,x) = \frac{1}{2} + \frac{1}{2}\left(\frac{1-mx}{w}\right)^3 + \frac{1}{2}x^3\left[2 - 3\left(\frac{x-m}{w}\right) + \left(\frac{x-m}{w}\right)^3\right] + \frac{3}{2}mx^2\left(\frac{x-m}{w} - 1\right) \quad (2)$$

In Eq. (2), the parameters (m), (x) and (w) are used to account the influence of the surface properties on the reduction factor (f):

$$m = cos\theta = \left(\frac{\gamma_{sv} - \gamma_{sl}}{\gamma_{lv}}\right) \quad (3)$$

$$x = \frac{R^p}{r_c} \quad (4)$$

$$w = \sqrt{\left(1 + x^2 - 2xm\right)} \quad (5)$$

Eq. (3) expresses the equilibrium contact angle θ, providing $-1 \leq m \leq 1$, which determines the wettability of the solid surface. On the other hand, (x) is a dimensionless parameter that presents the ratio of the radius of a spherical solid particle (R^p), around which the ice embryo forms, towards those of the critical ice embryo (r_c) (the minimum size that an incipient ice crystal needs to acquire to trigger freezing [25]). The latter is obtained as a function of the water-ice interfacial tension (γ), water molar volume (), water heat capacity (C_p), ice melting temperature (T_m) and the substrate temperature (T_{sub}), as shown by Cao et al. [24]. Adapting their approach to our experimental conditions (T_{sub} = −35 °C), r_c was calculated to be 6.93 nm.

Fig. 8 represents the calculated alteration of the reduction factor (f) as a function of (x) at particular substrate temperature (T_{sub}) and water contact angle (θ is expressed through m), similarly as in Refs. [24,28,41].

The exponential decay of (f) indicates that the free energy barrier for heterogeneous nucleation (ΔG_n) decreases when the relative particle size (x) increases. At the upper extreme value of f = 1, ΔG_n equals $\Delta G_n{}^{homo}$ and the nucleation rate (J) is low, while at f = 0 the energy barrier vanishes and nucleation should occur instantly (see Eq. (1)). In our case, the average size of the functionalized soot particles is ∼60 nm, which corresponds to f = 0.806. Therefore, at substrate temperatures of −35 °C, the reduction in the nucleation barrier with less than 20% and the decreased solid-liquid contact time t_{sl} = 3–20 ms are insufficient to initiate ice nucleation. These observations are in good agreement with the experimental results reported from Cao *et.al.*, where it is shown that the icing probability is relatively low at particles' size up to ∼100 nm [24].

3.4. Control experiments

Considering the possible practical applicability of our coatings, further experiments simulating harsh operational conditions were performed. Since the cold-region wind turbines are designed to operate continuously, the daily thermal drifts may cause condensation of water vapor on the substrate and subsequent loss of icephobicity [1,26]. Fig. S3 in the supporting information represents the impact dynamics of icy water droplets on horizontal soot coated Al sheet placed in a condensate environment (RH ∼100%), when the ambient temperature is gradually decreased over time from +21 °C to −35 °C with a cooling rate of ∼10 °C/h. Even in such an extreme case, where the ambient temperature changes drastically within a few hours, the functionalized carbon soot prevents the ice formation. The spreading and recoiling regimes take place within ∼14 ms, which inhibits the ice nucleation. Interestingly, the bouncing ability of the impinging droplets is lowered and they coalesce into bigger water droplet, which then shed-off the surface by sliding instead of rebounding. This observation might be ascribed to the mass of the liquid and the low impact velocity of 1 m/s, which can reduce the restitution coefficient of the droplet and suppress its bouncing [20]. However it may also be attributed to the frost formation on the surface, triggered by the condensation of water vapor upon reduction of the substrate temperature. The frost forms inevitably on any surface, whose temperature is below the dew point [42]; however, at 100% relative humidity the ambient temperature and dew point temperature match. Since we gradually decreased the ambient temperature when the air was saturated with water vapor, it was expected that the vapor may condense on the substrate. Indeed, the inner walls, as well as the shelves of the icing chamber were covered with frost, while on eye inspection the soot seemed to be unaffected and the icy droplets were successfully suspended after impact. One possible explanation is that the air has been cooled down faster than the superhydrophobic surface, which prevents the condensation of water vapor on the soot. However, the heat capacity of the Al alloy (6061) is higher than that of air ($C_v$air = 0.716 kJ/kgK; C_vAl6061 = 0.896 kJ/kgK at T = 300 K), implying that the Al substrate will decrease its temperature with a higher rate than the air. Another reason could be related with the low conduction of heat through the air, which in turn would increase the time needed for cooling of the soot coated Al sheet. However, such a hypothesis seems unlikely, since if this was true, then the inner walls and shelves of the chamber would also be free of frost. Apparently, that is not the case and the frosted shelves and inner walls of the chamber suggest that the metal surfaces, perhaps the soot coated Al substrate as well, have been cooled below the dew point temperature. Thus, in such a medium, the water vapor preferentially condensate on the hydrophilic (the shelves and walls) surfaces rather than the superhydrophobic ones (the soot coated Al), since the nucleation free energy barrier decreases significantly by switching the surface wettability from superhydrophobic to hydrophilic [2]. In fact, it has quantitatively been demonstrated that a soot coated quartz substrate adsorbs ∼7 times lower amount of water vapor compared to its uncoated counterpart [43]. Up to now, there is no unambiguous explanation of the soot's water vapor repellency; therefore, we can only speculate for the inhibited frost formation, assuming that the soot's immiscibility in water and its nanoscale surface topography are the primary reasons for that phenomenon [2,44]. Other scenario may consider the formation of spherical condensates on the superhydrophobic surface that are capable of spontaneous jumping off before initiation of freezing, as reported by Boreyko et al. for different chemical micropatterns [16,42].

Finally, we investigated the icephobicity of the functionalized coating upon frosting (large and instant thermal drifts causing condensation), as well as its mechanical durability under water jetting with velocity of ~25 m/s. Soot coated steel substrate (25 × 25 mm), cooled down in the icing chamber to −30 °C, was exposed to room temperature water vapor for 30 s (T ~22 °C) and then again mounted in the test chamber. Although such an instant thermal drift (change in the ambient temperature from −30 °C to +22 °C within seconds) is not common in "real-world" conditions, it is an excellent benchmark for evaluation of the materials' icephobicity upon frosting [1,16,42]. After exposure to room temperature, the entire soot surface covered with frost instantly and afterwards the icephobicity of the sample was tested again. Expectedly, the impinging water droplets turned into ice; however, they froze in a spherical shape. This might be caused by the air trapped within the surface protrusions, which reduces the actual solid-liquid surface area, allowing retention of the suspended Cassie-Baxter state even upon nucleation [14,15,42]. Furthermore, small amount of thermal energy and slight tilting of the sample (T_{sub} = ~−10 °C, θ ~30°) were enough to promote sliding of the entire piece of ice (Fig. S4 in the supporting information). The T_{sub}, at which sliding occurred, was measured with a Kintrex IRT0421 infrared thermal sensor, whose measurement accuracy was verified by determining the ambient and human body temperatures. In both cases the measurement accuracy was within ±1 °C. The ice was removed without any loss of integrity, while on bare Al or steel substrates it detached after complete melting. This implies low ice adhesion on the functionalized soot due to stress concentrations arisen from the air gaps in the coating and the reduced solid-liquid contact area, which further disrupt the ice bonds [11,16]. As a secondary effect, after the ice removal and subsequent increase in the substrate temperature above 0 °C, the frost was transformed into small spherical liquid droplets that then slid-off the surface. The dynamic removal of the melted frost may be a consequence of spontaneous dewetting followed by gravitational mobilization, as firstly shown by Boreyko et al. [45]. The authors explain this dynamic defrosting by the energetically driven minimization of the liquid's surface energy, which is physically enabled by the suspended Cassie-Baxter state of the surface [45]. Later, the soot coated steel substrate was heated up to room temperature and exposed for 5 s under water jetting with velocity of ~25 m/s. Even after such a reckless treatment, the central part of the surface remained hydrophobic, while the edges were still water repellent (supporting video S5). Moreover, a secondary treatment with fluorocarbon solution recovered the superhydrophobicity of more than 80% of the surface area, revealing that the chemical functionalization can substantially lengthen the lifetime of the coating (supporting video S6). For the sake of completeness, we investigated the durability of non-functionalized and fluorocarbon-modified soot samples (no ethanol treatment) under the same water jet (supporting videos S7, S8). After termination of the experiments, both types of coatings were completely destroyed and the surfaces exhibited hydrophilicity. Based on these comparative results, we presume that the functionalized soot would be able to resist the impact of heavy rains, which may occur during the operation of wind turbines.

4. Conclusions

This paper presented systematic experimental investigations on the icephobic properties of carbon soot coated Al and steel substrates. The inherent brittleness of the soot was circumvented by a secondary chemical treatment with ethanol and fluorocarbon solution. We found that the functionalized coatings exhibit enhanced mechanical strength and surface adhesion under compressed air scavenging, spinning and water jetting, which has important implications for their practical applicability. Also, the as prepared soot surfaces remained free of ice in the entire range of substrate temperatures at various impact dynamics scenarios. Our experiments correlated well with the kinetic model for three-dimensional heterogeneous nucleation and revealed that the average soot particle size falls into the length scale of icephobicity. In addition, upon frosting of the soot, the icy droplets nucleated in a ball-up shape and were easily removed using negligible amount of thermal energy. This implied reduced ice adhesion on the functionalized soot, attributed to the weakening and disruption of the ice bonds caused by the air trapped within the surface. Moreover, upon frosting and subsequent thermal heating above the freezing temperature, the soot coating was dynamically defrosted, which is of particular interest for a variety of systems in condensate environments. Last but not least, the high fabrication scalability of our approach, along with the enhanced durability of the soot coating, may further advance and facilitate the development of long lasting and inexpensive icephobic surfaces, which is of utmost importance for their industrial applicability. Achieving this goal goes through elucidation of the soot's frosting/defrosting mechanism, its water vapor repellency at certain circumstances and the physicochemical nature of the soot-ethanol interactions, which is planned as a future work. Although the prevention of atmospheric icing is a complex and non-trivial task, we believe that the results of this study are fundamental for the significant extension and enrichment of the current strategies for passive icing protection.

Acknowledgments

The authors wish to acknowledge the VCU's Nanomaterials Core Characterization Facility for providing access to the surface characterization equipment. Also, the startup support from Virginia Commonwealth University under grant 137422 is greatly acknowledged. Dr. Esmeryan wishes to gratefully acknowledge Prof. Neil Shirtcliffe from Rhine-Waal University of Applied Sciences for his comments about the chemistry of Grangers Performance Proofer and fruitful discussions.

Appendix A. Supplementary data

Supplementary data associated with this article can be found, in the online version, at http://dx.doi.org/10.1016/j.apsusc.2016.08.101.

References

[1] S. Farhadi, M. Farzaneh, S.A. Kulinich, Anti-icing performance of superhydrophobic surfaces, Appl. Surf. Sci. 257 (2011) 6264–6269.
[2] R.P. Sear, Nucleation: theory and applications to protein solutions and colloidal suspensions, J. Phys: Condens. Matter 19 (2007) 033101.
[3] E.B. Moore, V. Molinero, Structural transformation in supercooled water controls the crystallization rate of ice, Nature 479 (2011) 506–508.
[4] C.R. Sullivan, V.F. Petrenko, J.D. McCurdy, V. Kozliouk, Breaking the ice: de-icing power transmission lines with high-frequency high-voltage excitation, IEEE Ind. Appl. Mag. 9 (2003) 49–54.
[5] Y.H. Yeong, R. Mudafort, A. Steele, I. Bayer, E. Loth, Water droplet impact dynamics at icing conditions with and without superhydrophobicity, AIAA Paper 3134 (2012) 1–14.
[6] A.M. Palacios, J.L. Palacios, L. Sánchez, Eliciting a human understandable model of ice adhesion strength for rotor blade leading edge materials from uncertain experimental data, Expert Syst. Appl. 39 (2012) 10212–10225.
[7] R.W. Gent, N.P. Dart, J.T. Cansdale, Aircraft icing, Philos. Trans. R Soc. A 358 (*2000*) 2873–2911.
[8] P. Appiah-Kubi, US Inflight Icing Accidents and Incidents 2006–2010, Master's Thesis, University of Tennessee, 2011.
[9] N. Dalili, A. Edrisy, R. Carriveau, A review of surface engineering issues critical to wind turbine performance, Renew. Sustain. Energy Rev. 13 (2009) 428–438.
[10] O. Parent, A. Ilinca, Anti-icing and de-icing techniques for wind turbines: critical review, Cold Reg. Sci. Tech. 65 (2011) 88–96.

[11] S. Tarquini, C. Antonini, A. Amirfazli, M. Marengo, J. Palacios, Investigation of ice shedding properties of superhydrophobic coatings on helicopter blades, Cold Reg. Sci. Tech. 100 (2014) 50–58.
[12] S. Ramanathan, V.V. Varadhan, V.K. Varadhan, De-Icing of Helicopter Blades Using Piezoelectric Actuators, Smart Structures and Materials 2000: Smart Electronics and MEMS, SPIE Publishing, Seattle, WA, 2002, pp. 354–363.
[13] J. Palacios, E. Smith, J. Rose, R. Royer, Ultrasonic de-icing of wind-tunnel impact icing, J. Aircraft 48 (2011) 1020–1027.
[14] L. Mishchenko, B. Hatton, V. Bahadur, J.A. Taylor, T. Krupenkin, J. Aizenberg, Design of ice-free nanostructured surfaces based on repulsion of impacting water droplets, ACS Nano 4 (2010) 7699–7707.
[15] S. Jung, M. Dorrestijn, D. Raps, A. Das, C.M. Megaridis, D. Poulikakos, Are superhydrophobic surfaces best for icephobicity? Langmuir 27 (2011) 3059–3066.
[16] J.B. Boreyko, C.P. Collier, Delayed frost growth on jumping-drop superhydrophobic surfaces, ACS Nano 7 (2013) 1618–1627.
[17] M. Zou, S. Beckford, R. Wei, C. Ellis, G. Hatton, M.A. Miller, Effects of surface roughness and energy on ice adhesion strength, Appl. Surf. Sci. 257 (2011) 3786–3792.
[18] V. Hejazi, K. Sobolev, M. Nosonovsky, From superhydrophobicity to icephobicity: forces and interaction analysis, Sci. Rep. 3 (2013) 02194.
[19] C. Antonini, M. Innocenti, T. Horn, M. Marengo, A. Amirfazli, Understanding the effect of superhydrophobic coatings on energy reduction in anti-icing systems, Cold Reg. Sci. Tech. 67 (2011) 58–67.
[20] D. Richard, D. Quere, Bouncing water drops, Europhys. Lett. 50 (2000) 769–775.
[21] A. Alizadeh, M. Yamada, Ri Li, W. Shang, S. Otta, et al., Dynamics of ice nucleation on water repellent surfaces, Langmuir 28 (2012) 3180–3186.
[22] P. Tourkine, M.L. Merrer, D. Quere, Delayed freezing on water repellent materials, Langmuir 25 (2009) 7214–7216.
[23] P. Guo, Y. Zheng, M. Wen, C. Song, Y. Lin, L. Jiang, Icephobic/anti-icing properties of micro/nanostructured surfaces, Adv. Mater. 24 (2012) 2642–2648.
[24] L. Cao, A.K. Jones, V.K. Sikka, J. Wu, D. Gao, Anti-icing superhydrophobic coatings, Langmuir 25 (2009) 12444–12448.
[25] M. Nosonovsky, V. Hejazi, Why superhydrophobic surfaces are not always icephobic, ACS Nano 6 (2012) 8488–8491.
[26] S. Jung, M.K. Tiwari, N.V. Doan, D. Poulikakos, Mechanism of supercooled droplet freezing on surfaces, Nat. Commun. 3 (2012) 615.
[27] S.A. Kulinich, M. Farzaneh, How wetting hysteresis influences ice adhesion strength on superhydrophobic surfaces, Langmuir 25 (2009) 8854–8856.
[28] T.M. Schutzius, S. Jung, T. Maitra, P. Eberle, C. Antonini, C. Stamatopoulos, D. Poulikakos, Physics of icing and rational design of surfaces with extraordinary icephobicity, Langmuir 31 (2015) 4807–4821.
[29] T. Verho, C. Bower, P. Andrew, S. Franssila, O. Ikkala, R.H.A. Has, Mechanically durable superhydrophobic surfaces, Adv. Mater. 23 (2011) 673–678.
[30] A. Milionis, E. Loth, I.S. Bayer, Recent advances in the mechanical durability of superhydrophobic materials, Adv. Colloid Interface Sci. 229 (2016) 57–79.
[31] K.D. Esmeryan, C.E. Castano, A.H. Bressler, M. Abolghasemibizaki, R. Mohammadi, Rapid synthesis of inherently robust and stable superhydrophobic carbon soot coatings, Appl. Surf. Sci. 369 (2016) 341–347.
[32] K.D. Esmeryan, G. McHale, C.L. Trabi, N.R. Geraldi, M.I. Newton, Manipulated wettability of a superhydrophobic quartz crystal microbalance through electrowetting, J. Phys. D: Appl. Phys. 46 (2013) 345307.
[33] N.J. Shirtcliffe, private communication May 2016.
[34] X. Deng, L. Mammen, H.J. Butt, D. Volmer, Candle soot as a template for a transparent robust superamphiphobic coating, Science 335 (2012) 67–70.
[35] K.D. Esmeryan, E.I. Radeva, I.D. Avramov, Durable superhydrophobic carbon soot coatings for sensor applications, J. Phys. D Appl. Phys. 49 (2016) 025309.
[36] N.J. Shirtcliffe, S. Aqil, C. Evans, G. McHale, M.I. Newton, C.C. Perry, P. Roach, The use of high aspect ratio photoresist (SU-8) for super-hydrophobic pattern prototyping, J. Micromech. Microeng. 14 (2004) 1384–1389.
[37] A. Alizadeh, V. Bahadur, S. Zhong, W. Shang, R. Li, J. Ruud, M. Yamada, L. Ge, A. Dhinojwala, M. Sohal, Temperature dependent droplet impact dynamics on flat and textured surfaces, Appl. Phys. Lett. 100 (2012) 111601.
[38] L.H. Seeley, G.T. Seidler, Two-dimensional nucleation of ice from supercooled water, Phys. Rev. Lett. 87 (2001) 055702.
[39] V. Bertola, Drop impact on a hot surface: effect of a polymer additive, Exp. Fluids 37 (2004) 653–664.
[40] V. Bergeron, D. Bonn, J.Y. Martin, L. Vovelle, Controlling droplet deposition, Nature 405 (2000) 772–775.
[41] X.Y. Liu, A new kinetic model for three-dimensional heterogeneous nucleation, J. Chem. Phys. 111 (1999) 1628–1635.
[42] J.B. Boreyko, R.R. Hansen, K.R. Murphy, S. Nath, S.T. Retterer, C.P. Collier, Controlling condensation and frost growth with chemical micropatterns, Sci. Rep. 6 (2016) 19131.
[43] K.D. Esmeryan, T.A. Yordanov, L.G. Vergov, Z.G. Raicheva, E.I. Radeva, Humidity tolerant organic vapor detection using a superhydrophobic quartz crystal microbalance, IEEE Sens. J. 15 (2015) 6318–6325.
[44] S. Henning, M. Ziese, A. Kiselev, H. Saathoff, O. Möhler, T.F. Mentel, A. Buchholz, C. Spindler, V. Michaud, M. Monier, K. Sellegri, F. Stratmann, Hygroscopic growth and droplet activation of soot particles: uncoated succinic or sulfuric acid coated, Atmos. Chem. Phys. 12 (2012) 4525–4537.
[45] J.B. Boreyko, B.R. Srijanto, T.D. Nguyen, C. Vega, M.F. Cabrera, C.P. Collier, Dynamic defrosting on nanostructured superhydrophobic surfaces, Langmuir 29 (2013) 9516–9524.

Applied Surface Science 369 (2016) 341–347

Contents lists available at ScienceDirect

Applied Surface Science

journal homepage: www.elsevier.com/locate/apsusc

Perspective Article

Rapid synthesis of inherently robust and stable superhydrophobic carbon soot coatings

Karekin D. Esmeryan[a,b], Carlos E. Castano[a,c], Ashton H. Bressler[a], Mehran Abolghasemibizaki[a], Reza Mohammadi[a,*]

[a] Department of Mechanical and Nuclear Engineering, Virginia Commonwealth University, Richmond, VA 23284, USA
[b] Georgi Nadjakov Institute of Solid State Physics, 72, Tzarigradsko Chaussee Blvd, 1784 Sofia, Bulgaria
[c] Nanomaterials Core Characterization Facility, Department of Chemical and Life Science Engineering, Virginia Commonwealth University, Richmond, VA 23284, USA

ARTICLE INFO

Article history:
Received 6 October 2015
Received in revised form 2 February 2016
Accepted 7 February 2016
Available online 9 February 2016

Keywords:
Superhydrophobicity
Carbon soot
Rapeseed oil
Cone-shaped chimney

ABSTRACT

The fabrication of superhydrophobic coatings using a candle flame or rapeseed oil has become very attractive as a novel approach for synthesis of water repellent surfaces. Here, we report an improved, simplified and time-efficient method for the preparation of robust superhydrophobic carbon soot that does not require any additional stabilizers or chemical treatment. The soot's inherent stabilization is achieved using a specially-designed cone-shaped aluminum chimney, mounted over an ignited paper-based wick immersed in a rapeseed oil. Such configuration decreases the level of oxygen during the process of combustion; altering the ratio of chemical bonds in the soot. As a result, the fractal-like network of the carbon nanoparticles is converted into dense and fused carbon chains, rigidly coupled to the substrate surface. The modified carbon coating shows thermal sustainability and retains superhydrophobicity up to ~300 °C. Furthermore, it demonstrates a low contact angle hysteresis of 0.7–1.2° accompanied by enhanced surface adhesion and mechanical durability under random water flows. In addition, the soot's deposition rate of ~1.5 μm/s reduces the exposure time of the substrate to heat and consequently minimizes the thermal effects, allowing the creation of superhydrophobic coatings on materials with low thermal stability (e.g. wood or polyethylene).

1. Introduction

Recently, the superhydrophobic materials have become very attractive within the scientific and engineering community due to their enhanced water repellent ability [1–6]. The principles of superhydrophobicity have been established independently by Wenzel [7] and Cassie and Baxter [8] in the context of textiles. However, the interest in this field started growing a few decades later provoked by systematic studies performed on natural superhydrophobic surfaces such as the leaves of Lotus, Garden peas, Hosta, Lupin or the hydrofuge of water striders. Since then, many researchers have begun to investigate the physical mechanism of superhydrophobicity, both theoretically and experimentally [9,10]. Their studies have revealed that two parameters are responsible for the superhydrophobic behavior of some surfaces, namely a low surface free energy in combination with high-aspect ratio surface roughness. When a solid surface has asperities that are hydrophobic, relatively tall and sufficiently close (i.e. much smaller than the capillary length k^{-1}), the water droplets cannot penetrate between them [4]. Moreover, because of the reduced number of contact points with the solid, the droplets become extremely mobile and easily roll across the surface. Such surfaces are called superhydrophobic and are characterized with a static contact angle greater than 150°, contact angle hysteresis less than 5°, and roll-off angle less than 10° [3]. These unique features of superhydrophobic surfaces determine their potential applicability in various fields of industry, including self-cleaning materials [11], green engineering [12], marine fouling [13], drag-reducing surfaces [14,15], anti-icing systems [16,17], and acoustic wave sensor devices [18,19].

In general, there are two ways to fabricate superhydrophobic surfaces (coatings): one is to amplify the effect of hydrophobicity by roughening a surface with a low surface free energy. The other is to modify hierarchically-patterned surface with materials possessing a low surface free energy [20]. The fabrication procedure could be based on wax solidification, colloidal particles, lithography techniques, vapor deposition, templating, phase separation, polymer

* Corresponding author. Tel.: +1 804 8273997.
E-mail address: rmohammadi@vcu.edu (R. Mohammadi).

http://dx.doi.org/10.1016/j.apsusc.2016.02.089
0169-4332/

reconformation, sublimation, plasma treatment, electro spinning, sol–gel processing, electrochemical methods, hydrothermal synthesis, layer-by-layer deposition, etching and one pot reactions [4,21]. These techniques are powerful, accurate and efficient, but involve multistep procedures and harsh conditions or require special reagents and equipment [22]. In addition, some of them are applicable only to small areas of flat surfaces or specific materials [22]. To circumvent these limitations, a simple method for superhydrophobization of solid surfaces based on the incomplete combustion of carbon nanoparticles (soot), contained in a rapeseed oil mixture [23] or in candle soot [24], has recently been developed. This approach is facile, inexpensive, reliable and non-destructive. Moreover, recently it has been demonstrated that the soot combustion can be manipulated by means of a polycarbonate chamber [25]. As a result, nanoscale carbon particles with photoluminescent and superhydrophobic properties could be derived. However, the superhydrophobic surfaces made of carbon soot are fragile, as the attraction forces between the individual nanoparticles are weak [24,26,27]. When droplets of water roll-off such a surface, most of the soot is peeled-off, collapsing the superhydrophobic properties of the surface. Enhanced structural robustness and durability of the carbon soot has previously been achieved by using various stabilizers such as silica shell [24], polydimethylsiloxane (PDMS) [28,29], epoxy resin [19,30], paraffin wax [26], silicon [27], TiO_2 [31], expanded polystyrene foam [32] or plasma polymerized hexamethyldisiloxane [33]. Nevertheless, the utilization of stabilizers reduces the simplicity of the fabrication process. In addition, the PDMS, epoxy resin and paraffin wax suffer from several disadvantages, e.g. weak adherence to gold coated surfaces [34], high sensitivity to temperature and humidity variations [35] or low melting point (the paraffin wax starts melting around 46 °C).

Therefore, here we present a novel method for the fabrication of inherently robust and durable carbon soot based superhydrophobic surfaces (coatings). In this study, the soot released during the incomplete combustion of a rapeseed oil mixture is stabilized by using a specially-designed cone-shaped aluminum chimney. The latter decreases the level of oxidizers during the process of combustion, allowing for the formation of a soot coating with low content of oxygen groups and increased fraction of sp^3 hybridized carbon. The proposed technique is reliable, extremely time-efficient (superhydrophobic carbon coatings can be achieved within 20–60 s) and does not require any additives, solvents, stabilizers or chemicals. Moreover, as shown in previous investigations, the pure carbon soot has an excellent anti-corrosion resistance and is suitable for large-scale preparation of superhydrophobic surfaces [23]. Furthermore, it can be deposited on almost any surfaces, even paper [26]. To the best of our knowledge, our method is the simplest technique for obtaining stable superhydrophobic carbon soot surfaces.

2. Experimental

2.1. Surface coating fabrication and wettability

A paper based wick was immersed in approximately 50 ml of rapeseed oil previously added to an evaporating glass dish. After ignition and subsequent occurrence of a black fume, a cone-shaped aluminum chimney was mounted over the wick. Afterwards, a few glass slides (75 mm × 25 mm), aluminum and copper substrates, as well as polyethylene pads and wood rods were exposed over the fume, which caused the formation of carbon soot films on the substrate surface. The dimensions of the chimney were designed to be as follows: height h = 13 cm, diameter d = 1.5–6 cm (top and bottom, respectively) and narrow 1.5 cm × 2.5 cm opening at the bottom side, used to supply air. These parameters were found to provide the best experimental conditions for manipulation of the combustion process. The total deposition time depends on the surface area, similarly as in ref. [23]. For comparison purposes, we also produced soot-coated surfaces without using a chimney, following exactly the same procedure detailed above. To examine the wettability of the surfaces we performed static contact angle (SCA) and contact angle hysteresis (CAH) measurements for droplets of water, by using a Drop Shape Analyzer (DSA 25E, Krüss Germany).

2.2. Characterization

The morphology, structure and surface roughness of the carbon soot coatings in both modified (with chimney) and conventional (without chimney) conditions were investigated through Scanning Electron Microscopy (SEM), X-Ray Diffraction (XRD) and Atomic Force Microscopy (AFM) analyses. The SEM experiments were carried out using a Hitachi SU-70 Field Emission Scanning Electron Microscope (FESEM). XRD was performed using a Panalytical X'Pert Pro diffractometer operating in Bragg-Brentano mode. The incident X-rays were produced with Cu Kα radiation (λ = 1.54 Å) from 5° to 60° of 2θ, with a scan step size of 0.03°, using a 2° anti-scatter slit, 1° fixed divergence slit and 15 mm mask. The surface roughness imaging was taken in a tapping mode using silicon cantilever of 85 μm length, reflective gold coating on the backside, nominal resonance frequency ca. 125 kHz and spring constant of 0.5 N/m. An area of 1 μm^2 was scanned at a rate of 0.5 Hz, with a resolution of 512 lines per scan direction. The chemical composition of the carbon soot coatings was investigated qualitatively by Energy Dispersive Spectroscopy (EDS) at 15 KeV using an EDAX detector of 10 mm^2 of active area. In addition, X-ray photoelectron spectra were collected with a ThemoFisher ESCALAB 250 X-ray photoelectron spectrometer (XPS) using a monochromated aluminum X-ray source. Survey and high-resolution spectra were recorded by 1 eV and 0.1 eV steps, respectively. The composition of the coatings was calculated from the survey spectra, while the chemical states were found from the high resolution spectra. CASAXPS 2.3.16 V was used to fit and analyze the XPS spectra along with the NIST standard Reference Database 20, Version 4.1.

2.3. Control experiments

To assess the robustness, durability, surface adhesion, stability and uniformity of the modified carbon coatings, a series of control experiments were carried out. For the robustness and durability testing, each type of substrate (see Section 2.1) was coated with carbon soot by the conventional and modified approach. Subsequently, all samples were immersed in de-ionized water and after drying their wettability was examined. The surface adhesion experiments were performed through ASTM D3359 Standard Method for Measuring Adhesion by Tape Test [36]. This technique covers experimental procedures for examining the adhesion of different coatings to metal substrates, by applying and removing a pressure-sensitive tape over special grid cuts made on the film's surface. Although the Tape Test is designed particularly for metal substrates, it can be successfully adapted to any type of substrate for qualitative assessment of adhesion. The temperature sustainability of the modified carbon soot was investigated by heating the substrate surface up to 400 °C for 30 min. After cooling to room temperature, the SCA and CAH of the samples were measured. Finally, the uniformity of the coatings at various substrates, deposition time and distances was evaluated, and the most favorable experimental conditions were determined. For the sake of completeness, each substrate (glass, aluminum, copper, etc.) was rinsed under tap water in order to evaluate the underwater stability of as prepared superhydrophobic surfaces.

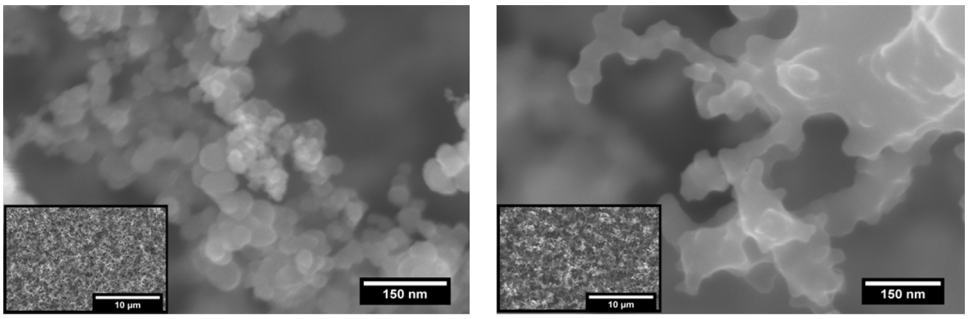

a) b)

Fig. 1. SEM image at low and high magnifications of (a) conventional and (b) modified carbon soot coatings.

3. Results and discussions

3.1. Morphology and elemental analysis of the modified carbon soot nanoparticles

Fig. 1 compares the surface morphology and structure of conventional and modified carbon soot coatings deposited on glass slides.

Regardless the deposition approach, both images reveal that the carbon soot precipitates on the substrates irregularly, forming elongated islands separated by micro-nanoscale pores. The conventional coating is characterized by spherical carbon nanoparticles with approximate size of 50 nm (as shown in Fig. 1a). Similar results are reported in refs. [23,24,26,30], where the soot is stabilized using various techniques. However, as shown in Fig. 1b), the particles in the modified carbon soot are much denser and fused, which could be the reason for their stability upon contact with water. This hypothesis is related to the chemical processes, which occur during the incomplete combustion of carbon nanoparticles. In general, the flames can be divided in two classes, namely premixed and diffusion flames. The premixed flames, known also as a Bunsen type flames, occur when the oxidizer is mixed with the fuel (in our case the rapeseed oil) before it reaches the flame front [37]. This creates a thin flame front, as all of the reactants are readily available, and due to the large quantity of oxygen the incomplete combustion of the fuel is low. On the other hand, the diffusion flames are characterized with an oxidizer, which is supplied to the fuel coincidently with the occurrence of combustion and reacts with it by diffusion [37]. Thus, such flames tend to burn slower and produce more soot compared to the premixed ones, due to the lower quantity of oxidizer.

In our case, a paper based wick is immersed in a rapeseed oil, which acts as a fuel and the oxidizer is the surrounding atmosphere oxygen. The ignition of the wick gives enough heat in the subsequent exothermic reaction to vaporize the fuel (oil), while the oxygen diffuses into the carbon molecules of the flame, thus sustaining a consistent and continuous combustion. However, mounting a cone-shaped aluminum chimney over the wick further reduces the level of oxygen in the combustion process. Moreover, due to the small diameter of the chimney's tip (see Section 2), the fume flow is converted from turbulent to laminar. Similar flow is observed when a candle is used to fabricate carbon soot coatings [24,26]. As a result, the ratio of chemical bonds in the soot could be altered, which may lead to dense and fused carbon nanoparticles. Such a speculation is partially confirmed by the cross-section SEM images of conventional and modified carbon soot coatings deposited on glass slides.

As seen from Fig. 2, at equal other conditions, the thickness of the modified carbon soot coating is approximately 70 μm, while of the conventional soot is around 14 μm. These experimental data clearly indicate that the reduction of oxygen increases the quantity of non-combusted material (carbon nanoparticles), which results in thicker carbon soot coatings.

In addition, the XRD analyses (not shown here) reveal that both coatings are largely amorphous. Nevertheless, the SEM and XRD cannot provide authentic explanation why the modified soot is stable upon water interactions. Moreover, these techniques do not elucidate how the reduction of oxygen affects the carbon soot formation and/or its chemical bonds. Therefore, after completing the SEM and XRD investigations, the chemical composition of the conventional and modified carbon soot was examined by EDS and XPS. The EDS measurements reveal that in both cases, the main component is carbon; however, the modified coating is characterized with higher concentration (see the supporting information). Furthermore, the atomic percentage of oxygen is reduced by a factor of 8, which accounts for the decrease in the level of oxidizer during the process of combustion, as well as for less interaction with the substrate composition. The modified coating also contains less silicon compared to the conventional one. Similarly, this is attributed to the lower interaction of the incident electron beam with the glass substrate, because of the denser and thicker carbon

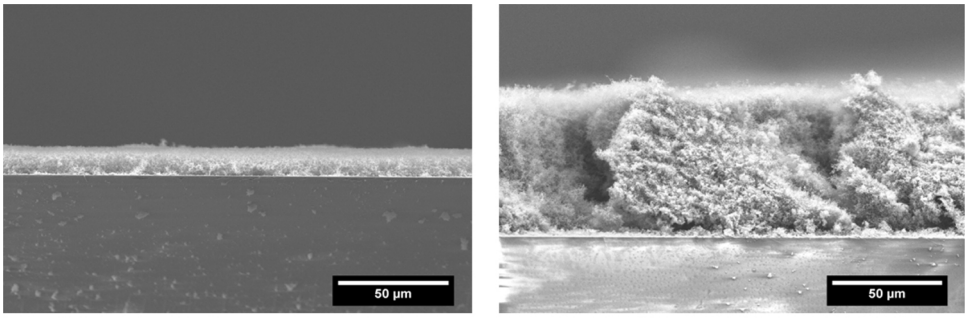

a) b)

Fig. 2. Cross-sectional SEM images of (a) conventional and (b) modified carbon soot coatings.

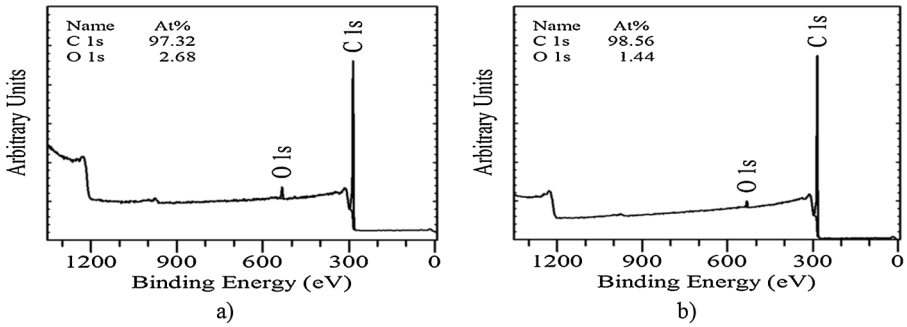

Fig. 3. XPS spectrum of (a) conventional and (b) modified carbon soot coatings.

soot coating. The appearance of other chemical components such as Na, Mg, Al, K and Ca is due to the chemical composition of the CapitolBrand M3504-E glass slides. Comparative experimental investigations were conducted by XPS analysis. Fig. 3 shows the survey scans of the conventional and modified soot samples.

The results are consistent with those from the EDS, indicating that the soot layers consist mainly of carbon. In addition to carbon, oxygen is the other element detected by the XPS, being 2.7 at.% and 1.4 at.% for the conventional and modified coatings, respectively. The surface sensitivity of the XPS technique provides information of the immediate surface of the layer without getting any signal from the substrate composition, as measured by the EDS. Although XPS is not capable to identify elemental hydrogen, this analysis was performed indirectly by doing high-resolution XPS to the C1s.

The high-resolution C1s photoelectron spectra of the conventional and modified carbon soot coatings are compared in Fig. 4. The deconvolution of the C1s regions in both cases is achieved with 5 peaks, corresponding to sp^2 hybridized carbon at 284.8 eV, sp^3 hybridized carbon at 285 eV, epoxy/hydroxyl groups (C–O–C/C–OH) at 286.5 eV, carbonyl group (C=O) at 288.5 eV and π–π^* satellite group at 291 eV. The sp^2/sp^3 ratios calculated from the XPS spectra are 1.17 and 0.91 for the conventional and modified carbon soot, respectively.

In addition, the π–π^* satellite peak in the modified version is less prominent in comparison with the conventional coating. These observations are in good agreement with the morphological features of both coatings (see Fig. 1) and can be explained by the mechanism of soot formation. According to it, the primary soot particle contains crystallites with a thickness up to 1.2 nm [38]. These crystallites are composed of multitude binary arrays of carbon atoms, described as platelets. Each array is in the form of hexagonal lattice, which is typical for the sp^2 hybridization. In the latter, a single carbon atom is bonded to another three carbon atoms forming a hexagonal matrix, which yields the spherical shape of the soot. Therefore, the nanospheres observed in Fig. 1a) are related to the occurrence of high sp^2 hybridized carbon [39,40]. Based on this, the reduction of sp^2/sp^3 ratio is the reason for the fused structure and mechanical durability of the modified carbon soot. This is due to the increased amount of sp^3 hybridized carbon, which leads to more pronounced tetrahedral (diamond-like) shape of the modified soot in comparison with the conventional one. In addition, the weak π bonds, typical for sp^2 hybridization, are replaced by much stronger σ bonds, which accounts for the increased mechanical durability of the soot. Furthermore, the carbon–oxygen functional groups show different ratios {(C–O–C, C–OH)/C=O}, about 2.5 and 1.9 for the conventional and modified carbon soot. In general, the non-polar nature of the carbon bonds makes these soot layers highly hydrophobic [41]. However, the presence of C–OH functional groups, related to the oxygen content, affects the formation of hydrogen bonds upon contact with water molecules [41,42]. In fact, due to the large amount of polar C–OH groups, some diesel engine soot and spark discharge model soot (GfG) are considered as hydrophilic [40]. In our case, the suppression of oxygen leads to reduced amount of C–OH groups, which are replaced by strong double carbon–oxygen bonds (C=O). As a result, the binding properties of the modified soot are enhanced [40] and its contact with water is reduced due to the decreased number of hydrophilic active sites (C–OH groups) [41].

3.2. Surface wettability and roughness

The surface wettability of several modified carbon soot coatings deposited on glass, aluminum, copper and polyethylene substrates, as well as wood rods, was determined through SCA and CAH measurements for droplets of water with 8 μl volume. All experimental data were recorded and processed on a personal computer via DSA4 computer software. For all types of carbon soot coated substrates, the SCA and CAH are in the range of 153–156° and 0.7–1.2°, respectively, thereby confirming superhydrophobicity with extreme droplet mobility [3–5]. Each surface was tested at different areas in five independent measurement cycles. The results show reproducibility with a highest deviation of ±1° and ±0.3°

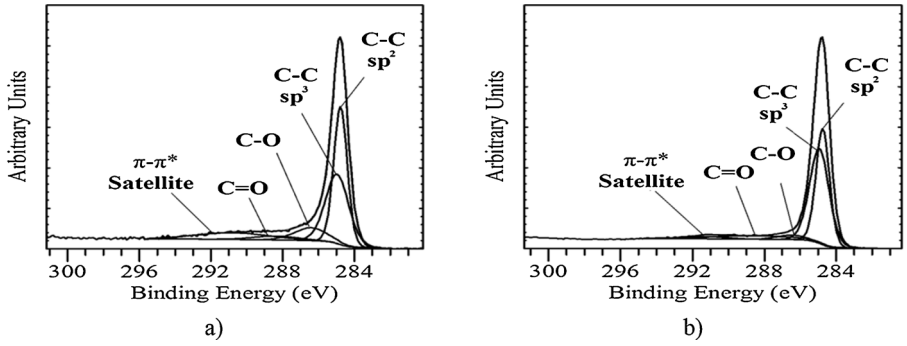

Fig. 4. C1s photoelectron core level of (a) conventional and (b) modified carbon soot coatings.

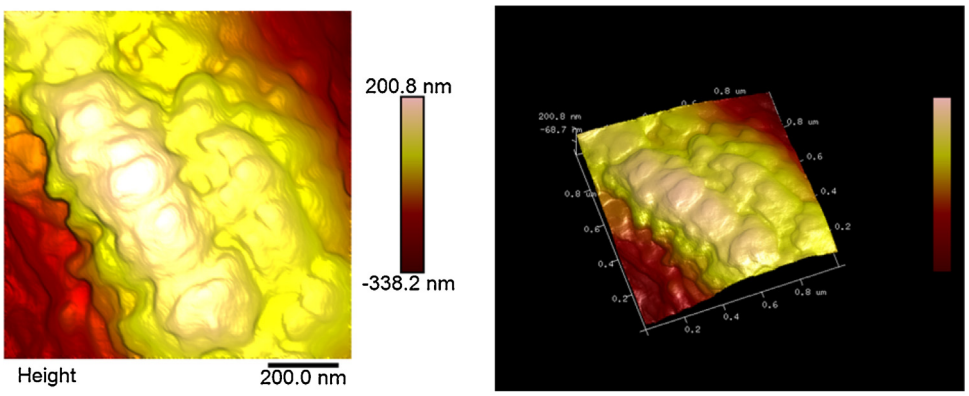

Fig. 5. (a) 2-D and (b) 3-D AFM images of a modified soot coated glass slide.

for the SCA and CAH, respectively. Furthermore, due to the soot's higher deposition rate, in comparison to the thermal effects on the materials from the heat of the flame [43], even substrates with low thermal sustainability (e.g. wood or polyethylene) can be coated with superhydrophobic carbon soot. To correlate the superhydrophobic behavior of as prepared coatings with their surface roughness and surface free energy, we performed AFM analyses followed by surface free energy calculations. Fig. 5 illustrates 2-D and 3-D AFM images of modified carbon soot deposited on a microscope glass slide.

The estimated root mean square roughness (R_{rms}) for the modified soot was found to be ~107 nm. Such a roughness value is consistent with previously reported AFM data for the conventional carbon soot, whose R_{rms} is ~130 nm [30,44]. These results indicate that regardless the chimney modification our carbon layer keeps its rough profile and along with the non-polar nature of the soot amplifies the effect of hydrophobicity. We have also calculated the surface energy of the modified coating by adapting the method described in ref. [45]. According to this method, the surface energy γ_{sv} of a solid is composed of a polar (γ_{sv}^{p}) and dispersion (γ_{sv}^{d}) component. The computation of the solid–vapor interfacial energy γ_{sv} is based on geometric and harmonic models using as reference liquids de-ionized water and diiodomethane (CH_2I_2) [45]. Both methods gave us relatively close values of γ_{sv}, namely 33.08 mN/m and 39.97 mN/m for the geometric and harmonic approach, respectively.

3.3. Robustness, durability, surface adhesion and temperature stability of the modified carbon soot

The conventional carbon coating exhibits high instability and fragility upon immersion in de-ionized water, regardless of the film thickness. The soot easily peels-off after contact with water. Similar effect is observed in all previous soot approaches, where prior to stabilization the chemical bonds between the carbon nanoparticles are weak [24,26,27,30]. In contrast, the modified soot layer possesses robustness and durability regardless the chosen substrate (glass, metal, plastic or wood) and film thickness, which proves its enhanced stability and clearly demonstrates the advantage of the proposed chimney method (see the supporting information). The contact angle measurements show a static contact angle of 153–156° and a contact angle hysteresis of 0.7–1.2°, which confirms the superhydrophobicity of these surfaces.

The surface adhesion test reveals that the conventional soot coating has a very weak adhesion to all substrates (glass, aluminum, copper, polyethylene and wood). The carbon nanoparticles are completely transferred on the scotch tape after its removal. This phenomenon is attributed to the weak interfacial forces at the soot–substrate interface and corresponds to adhesion class of 0B, where more than 65% of the coating's area is removed [36]. On the other hand, the chimney-modified carbon films are mechanically stable and after Tape Test, the removed soot is less than 5%, i.e. class of 4B (see the supporting information).

The thermal sustainability of the modified coatings was examined by heating carbon soot coated glass slides up to 400 °C with a step of 50 °C for 30 min. After cooling to room temperature, the static contact angle (SCA) and contact angle hysteresis (CAH) of the samples were measured. The experimental results are summarized in Fig. 6.

Up to 275 °C, the soot coated glass substrate shows high SCA and low CAH in the range of 155–156° and 0.1–0.4, respectively, thereby confirming temperature sustainability of the superhydrophobic coating. Upon increasing the temperature to 300 °C, the coating retains its superhydrophobic properties, but some part of the soot is peeled-off after rinsing under tap water. This temperature appears to be a threshold, above which the structure of the layer undergoes transformation. Such structural alteration occurs due to the increased mobility of carbon atoms, because of the high heating temperature [46]. In turn, the absorbed thermal energy ruptures the carbon bonds and the nanostructure is transformed into "onion-type", similar to what is observed after electron irradiation [46]. In other words, at 300 °C, the dense and fused carbon nanoparticles begin to convert into their conventional spherical shape, which leads to degraded stability of the soot. Further increase in temperature to 400 °C causes complete transformation of the structure and the coating is washed away with a water jet.

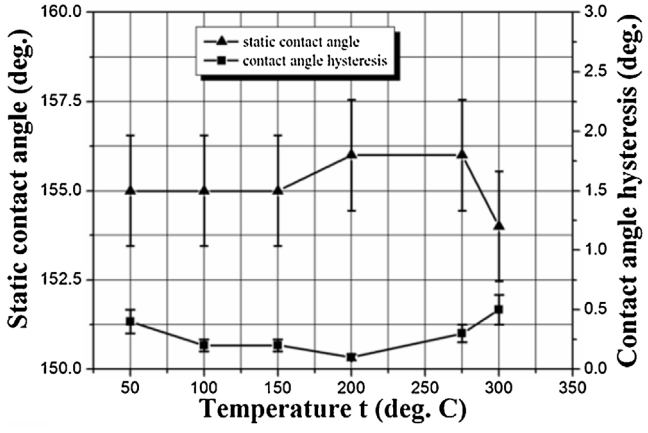

Fig. 6. Static contact angle and contact angle hysteresis at different temperatures.

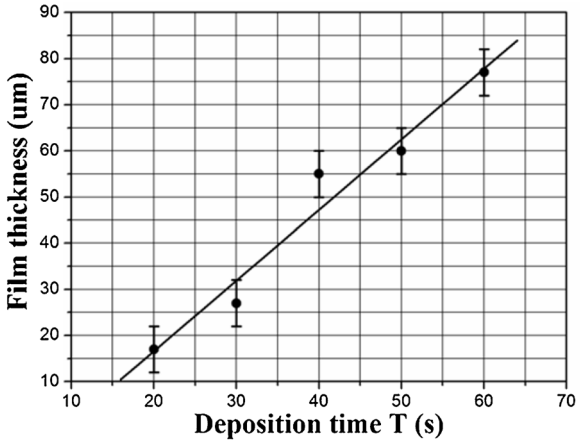

Fig. 7. Relation between the deposition time and the soot's thickness.

3.4. Thickness and uniformity of the modified carbon soot at various substrates, deposition time and distances

Fig. 7 illustrates the thickness of the carbon soot coating versus different deposition times.

As seen, increasing the deposition time from 20 s to 60 s causes a proportional linear increase in the film thickness. The maximum carbon soot thickness in this time-frame is approximately 77 ± 5 μm, while the deposition rate is ~1.5 μm/s. In comparison, the method described in ref. [23] allows the deposition of superhydrophobic carbon soot within 1–3 min. This is around three time's lower deposition rate compared to our technique, which is a clear indication for the improved efficiency of the chimney approach. On the other hand, the deposition distance is irrelevant to the coating's thickness, but affects the stability and uniformity of the modified carbon soot. Each type of substrate was exposed to the carbon fume for 40 s, while the distance between the samples and the chimney was varied in the range of 0–9 cm. It was found that stable, uniform, and homogeneous superhydrophobic coatings can be achieved only if the soot deposition is conducted within 3–7 cm above the chimney's tip. Outside this range, the carbon soot layer is non-uniform and its stability is degraded. For instance, the incomplete combustion of carbon nanoparticles is unstable at the region just above the chimney's tip (0–2 cm), because the temperature is at its maximum. On the other hand, too far from the tip (more than 7 cm), the temperature is low (below 100 °C) and the soot cannot be deposited successfully. For the favorable range of 3–7 cm, the substrate temperature deviates between 225 °C and 105 °C depending on the deposition time. Moreover, the mechanical durability of as prepared soot layers is independent on the film thickness (deposition time). In the entire thickness range, i.e. $17–77 \pm 5$ μm, the modified carbon soot is stable and does not peel-off upon water interactions. Finally, all samples including glass, aluminum, copper, polyethylene and wood, were rinsed under tap water. There were no visible damages in the integrity of the modified carbon soot coatings, showing enhanced mechanical durability of the soot under random water flows. In addition, an average SCA and CAH of 154° and 0.9°, respectively, confirmed the superhydrophobicity of surfaces.

4. Conclusions

This work presented an efficient method for the fabrication of robust and stable superhydrophobic carbon soot coatings. The inherently fragile conventional carbon nanoparticles were modified and stabilized without utilization of any additional reagents, chemicals or stabilizers. The proposed technique was based on reduction of the amount of oxygen during the incomplete combustion of carbon nanoparticles, contained in a rapeseed oil. This was achieved using a specially-designed cone-shaped aluminum chimney, whereby the chemical bonds in the soot were modified. In turn, the fractal-like network of the soot was converted into dense and fused carbon chains. Moreover, the modified carbon coating showed enhanced durability under random water flows and improved surface adhesion compared to the conventional soot layers. In addition, it demonstrated thermal sustainability up to 300 °C and a low contact angle hysteresis of 0.7–1.2°. Furthermore, due to the high deposition rate (~1.5 μm/s) of the modified soot, our method allowed superhydrophobization of substrates with low thermal sustainability. These results open a new venue in materials science for rapid fabrication of large-scale robust superhydrophobic surfaces with potential for a wide range of industrial applications.

Acknowledgments

The authors wish to gratefully acknowledge Mr. Zachary Soulier and Mr. Christian Fergusson for their assistance with the laboratory equipment. Services in support of the project were provided by the VCU Massey Cancer Center, supported in part with funding from NIH-NCI P30CA016059. Also, the startup support from Virginia Commonwealth University under grant 137422 is greatly acknowledged.

Appendix A. Supplementary data

Supplementary data associated with this article can be found, in the online version, at http://dx.doi.org/10.1016/j.apsusc.2016.02.089.

References

[1] W. Chen, A.Y. Fadeev, M.C. Hsieh, D. Öner, J. Youngblood, T.J. McCarthy, Ultrahydrophobic and ultralyophobic surfaces: some comments and examples, Langmuir 15 (1999) 3395–3399.
[2] D. Quere, Wetting and roughness, Annu. Rev. Mater. Res. 38 (2008) 71–79.
[3] P. Roach, N.J. Shirtcliffe, M.I. Newton, Progress in superhydrophobic surface development, Soft Matter 4 (2008) 224–240.
[4] N.J. Shirtcliffe, G. McHale, S. Atherton, M.I. Newton, An introduction to superhydrophobicity, Adv. Colloid Interface Sci. 161 (2010) 124–138.
[5] J.T. Simpson, S.R. Hunter, T. Aytug, Superhydrophobic materials and coatings: a review, Rep. Prog. Phys. 78 (2015) 086501.
[6] R. Mohammadi, J. Wassink, A. Amirfazli, Effect of surfactants on wetting of super-hydrophobic surfaces, Langmuir 20 (2004) 9657–9662.
[7] R.N. Wenzel, Resistance of solid surfaces to wetting by water, Ind. Eng. Chem. 28 (1936) 988–994.
[8] A.B.D. Cassie, S. Baxter, Wettability of porous surfaces, Trans. Faraday Soc. 40 (1944) 546.
[9] T. Onda, S. Shubuichi, N. Satoh, K. Tsujii, Super-water-repellent fractal surfaces, Langmuir 12 (1996) 2125–2127.
[10] W. Barthlott, C. Neinhuis, The purity of sacred lotus or escape from contamination in biological surfaces, Planta 202 (1997) 1–8.
[11] Y. Zhao, N. Wang, Electrospun superhydrophobic self-cleaning materials, in: Electrospun Nanofibers for Energy and Environmental Applications, Springer, Berlin, 2014, pp. 449–472, chapter 18.
[12] M. Nosonovsky, B. Bhushan, Superhydrophobic surfaces and emerging applications: non adhesion, energy, green engineering, Curr. Opin. Colloid Interface Sci. 14 (2009) 270–280.
[13] J. Genzer, K. Efimenko, Recent developments in superhydrophobic surfaces and their relevance to marine fouling: a review, Biofouling 22 (2006) 339–360.
[14] G. McHale, M.I. Newton, N.J. Shirtcliffe, Immersed superhydrophobic surfaces: gas exchange, slip and drag reduction properties, Soft Matter 6 (2010) 714–719.
[15] J.P. Rothstein, Slip on superhydrophobic surfaces, Annu. Rev. Fluid Mech. 42 (2010) 89–109.
[16] S. Farhadi, M. Farzaneh, S.A. Kulinich, Anti-icing performance of superhydrophobic surfaces, Appl. Surf. Sci. 257 (2011) 6264–6269.
[17] L. Cao, A.K. Jones, V.K. Sikka, J. Wu, D. Gao, Anti-icing superhydrophobic coatings, Langmuir 25 (2009) 12444–12448.
[18] P. Roach, G. McHale, C.R. Evans, N.J. Shirtcliffe, M.I. Newton, Decoupling of the liquid response of a superhydrophobic quartz crystal microbalance, Langmuir 23 (2007) 9823–9830.

[19] K.D. Esmeryan, G. McHale, C.L. Trabi, N.R. Geraldi, M.I. Newton, Manipulated wettability of a superhydrophobic quartz crystal microbalance through electrowetting, J. Phys. D: Appl. Phys. 46 (2013) 345307.
[20] C.H. Xue, S.T. Jia, J. Zhang, J.Z. Ma, Large-area fabrication of superhydrophobic surfaces for practical applications: an overview, Sci. Technol. Adv. Mater. 11 (2010) 033002.
[21] X. Zhang, F. Shi, J. Niu, Y. Jiang, Z. Wang, Superhydrophobic surfaces: from structural control to functional application, J. Mater. Chem. 18 (2008) 621–633.
[22] P. Levkin, F. Svec, J. Frechet, Porous polymer coatings: a versatile approach to superhydrophobic surfaces, Adv. Funct. Mater. 19 (2009) 1993–1998.
[23] M. Qu, J. He, B. Cao, Facile fabrication of large-scale stable superhydrophobic surfaces with carbon sphere films by burning rapeseed oil, Appl. Surf. Sci. 257 (2010) 6–9.
[24] X. Deng, L. Mammen, H.J. Butt, D. Volmer, Candle soot as a template for a transparent robust superamphiphobic coating, Science 335 (2012) 67–70.
[25] B.N. Sahoo, B. Kandasubramanian, Photoluminescent carbon soot particles derived from controlled combustion of camphor for superhydrophobic applications, RSC Adv. 4 (2014) 11331–11342.
[26] K. Seo, M. Kim, D.H. Kim, Candle-based process for creating a stable superhydrophobic surface, Carbon 68 (2014) 583–596.
[27] L. Shen, W. Wang, H. Ding, Q. Guo, Flame soot stably deposited on silicone coatings possess superhydrophobic surface, Appl. Surf. Sci. 284 (2013) 651–656.
[28] L. Yuan, J. Dai, X. Fan, T. Song, Y.T. Tao, K. Wang, Z. Xu, J. Zhang, X. Bai, P. Lu, J. Chen, J. Zhou, Z.L. Wang, Self-cleaning flexible infrared nanosensor based on carbon nanoparticles, ACSNano 5 (2011) 4007–4013.
[29] X. Liu, Y. Xu, Z. Chen, K. Ben, Z. Guan, Robust and antireflective superhydrophobic surfaces prepared by CVD of cured polydimethylsiloxane with candle soot as a template, RSC Adv. 5 (2015) 1315–1318.
[30] K.D. Esmeryan, Ts.A. Yordanov, L.G. Vergov, Z.G. Raicheva, E.I. Radeva, Humidity tolerant organic vapor detection using a superhydrophobic quartz crystal microbalance, IEEE Sens. J. 15 (2015) 6318–6325.
[31] S. Liu, M. Sakai, B. Liu, C. Terashima, K. Nakata, A. Fujishima, Facile synthesis of transparent superhydrophobic titania coating by using soot as a nanoprint template, RSC Adv. 3 (2013) 22825.
[32] B.N. Sahoo, B. Kandasubramanian, M. Sucheendran, Thermally triggered transition of superhydrophobic characteristics of micro- and nanotextured multiscale rough surfaces, J. Phys. Chem. C 119 (2015) 14201–14213.
[33] K.D. Esmeryan, E.I. Radeva, I.D. Avramov, Durable superhydrophobic carbon soot coatings for sensor applications, J. Phys. D: Appl. Phys. 49 (2016) 025309.
[34] J. Lotters, W. Olthuis, P. Veltink, P. Bergveld, The mechanical properties of the rubber elastic polymer polydimethylsiloxane for sensor applications, Micromech. Microeng. 7 (1997) 145–147.
[35] W. Brostow, N. Glass, Cure progress in epoxy systems: dependence on temperature and time, Mater. Res. Innov. 7 (2003) 125–132.
[36] ASTM Standard D3359-09, Standard Test Methods for Measuring Adhesion by Tape Test, in: ASTM International, 100 Barr Harbor Drive, PO Box C700, West Conshohocken, PA 19428-2959, United States (2009) 8.
[37] S.P. Burke, T.E.W. Schumann, Diffusion flames, Ind. Eng. Chem. 20 (1928) 998–1004.
[38] O.I. Smith, Fundamentals of soot formation in flames with application to diesel engine particulate emission, Prog. Energy Combust. Sci. 7 (1981) 275–291.
[39] G. Levi, O. Senneca, M. Causà, P. Salatino, P. Lacovig, S. Lizzit, Probing the chemical nature of surface oxides during coal char oxidation by high-resolution XPS, Carbon 90 (2015) 181–196.
[40] J.O. Muller, D.S. Su, U. Wild, R. Schlogl, Bulk and surface structural investigations of diesel engine soot and carbon black, Phys. Chem. Chem. Phys. 9 (2007) 4018–4025.
[41] O. Popovicheva, N.M. Persiantseva, N.K. Shonija, P. DeMott, K. Koehler, M. Petters, et al., Water interaction with hydrophobic and hydrophilic soot particles, Phys. Chem. Chem. Phys. 10 (2008) 2332–2344.
[42] L. Lupi, V. Molinero, Does hydrophilicity of carbon particles improve their ice nucleation ability? J. Phys. Chem. A 118 (2014) 7330–7337.
[43] A.E. Karatas, Ö.L. Gülder, Soot formation in high pressure laminar diffusion flames, Prog. Energy Combust. Sci. 38 (2012) 818–845.
[44] K.D. Esmeryan, V. Georgieva, L. Vergov, J. Lazarov, A superhydrophobic quartz crystal microbalance based chemical sensor for NO_2 detection, Bul. Chem. Commun. 47 (2015) 1039–1044.
[45] A. Sanger, A. Kumar, S. Chauhan, Y.K. Gautam, R. Chandra, Fast and reversible hydrogen sensing properties of Pd/Mg thin film modified by hydrophobic porous silicon substrate, Sens. Actuators B Chem. 213 (2015) 252–260.
[46] A.Ya. Vul, O.A. Shenderova, Carbon onions, in: Detonation Nanodiamonds: Science and Applications, CRC Press Taylor and Francis Group, 2013, pp. 9–12.

RSC Advances

PAPER

View Article Online
View Journal | View Issue

Cite this: *RSC Adv.*, 2016, **6**, 61620

Single-step flame synthesis of carbon nanoparticles with tunable structure and chemical reactivity†

Karekin D. Esmeryan,[ab] Carlos E. Castano,[ac] Ashton H. Bressler,[a] Christian P. Fergusson[a] and Reza Mohammadi*[a]

A novel method for the flame synthesis of carbon nanoparticles with controllable fraction of amorphous, graphitic-like and diamond-like phases is reported. The structure of nanoparticles was tailored using a conical chimney with an adjustable air-inlet opening. The opening was used to manipulate the combustion of an inflamed wick soaked in rapeseed oil, establishing three distinct combustion regimes at fully-open, half-open and fully-closed opening. Each regime led to the formation of carbon coatings with diverse structure and chemical reactivity through a facile, single-step process. In particular, the fully-closed opening suppressed most of the inlet air, causing an increased fuel/oxygen ratio and decreased flame temperature. In turn, the nucleation rate of soot nanoparticles was enhanced, triggering the precipitation of some of them as diamond-like carbon (DLC). Surface characterization analyses using Raman spectroscopy, X-ray photoelectron spectroscopy and transmission electron spectroscopy confirmed this hypothesis, indicating a short-range ordered nanocrystalline structure and ~80% sp^3 bonds in the coatings deposited at fully-closed opening. Furthermore, three groups of 5 MHz Quartz Crystal Microbalances (QCMs) coated with soot and DLC, corresponding to each of the three combustion regimes, showed different frequency responses to aqueous ethanol and isopropanol solutions in the concentration range of 0–12.5 wt%. The DLC coated QCMs exhibited relatively constant frequency shift of ~2250 Hz regardless of the chemical, while the response of soot coated counterparts was influenced by the quantity of heteroatoms in the film. Our method can be applied in chemical sensing for the development of piezoresonance liquid sensors with tunable sensitivity.

Received 10th March 2016
Accepted 19th June 2016

DOI: 10.1039/c6ra06436a

www.rsc.org/advances

1. Introduction

Carbon is one of the most remarkable chemical elements, as it is capable of forming a variety of chemical bonds with itself and/or atoms of other elements.[1] Its physicochemical characteristics depend on the structural configuration of the atomic bonds (sp^1, sp^2 or sp^3) and due to these natural peculiarities, carbon can be found in different forms such as diamond, graphite, fullerenes and amorphous carbon.[2,3] The latter is a metastable phase considered as a mixture of highly disordered carbon atoms with different fractions of sp^3, sp^2 and even sp^1 bonding.[1] A major advantage of the amorphous carbon is the ability to exhibit different physicochemical properties by altering the ratio of sp^2/sp^3 bonds and the quantity of heteroatoms[2] (*e.g.* oxygen). For instance, amorphous carbon films that exhibit a short-range ordered nanocrystalline structure and significant sp^3 content, known also as diamond-like carbon (DLC), are characterized with enhanced density, wear resistance, chemical inertness and optical transparency.[4–8] On the other hand, the increased amount of sp^2 bonds can transform the coating into a graphite-like carbon with high porosity, leading to a large specific surface area and improved chemical reactivity.[9–11] Therefore, the amorphous carbon coatings have strong potential for a wide range of practical applications, including electrochemical energy storage,[12] active catalysts for the hydrolysis of cellulose,[13] chemical sensors,[14,15] photovoltaic solar cells[16] or artificial knee–hip bioimplants.[17,18]

For each particular application, the content of sp^2 and sp^3 bonds in the coating along with the quantity of heteroatoms can be adjusted to provide the desirable physicochemical characteristics.[2] The best way of implementing this concept is through direct activation,[19] carbonization of crosslinked polymers,[20] chemical vapor deposition,[21] pulsed laser deposition,[22] ion beam/magnetron sputtering[23,24] or glow discharge RF plasma treatment.[25] These techniques are efficient and accurate; however, each of them has specific disadvantages in terms of the deposition rate, film's quality and uniformity, as well as the necessity of expensive equipment (lasers, plasma reactors, chemical chambers, *etc.*). Furthermore, most of the aforementioned procedures require

[a]*Department of Mechanical and Nuclear Engineering, Virginia Commonwealth University, Richmond, VA, 23284, USA. E-mail: rmohammadi@vcu.edu*

[b]*Georgi Nadjakov Institute of Solid State Physics, 72, Tzarigradsko Chaussee Blvd., 1784 Sofia, Bulgaria*

[c]*Nanomaterials Core Characterization Facility, Department of Chemical and Life Science Engineering, Virginia Commonwealth University, Richmond, VA, 23284, USA*

† Electronic supplementary information (ESI) available. See DOI: 10.1039/c6ra06436a

precise control of the experimental conditions such as vacuum and pressure, which determines the need for specially-designed hermetically sealed chambers. In contrast, the deposition of amorphous carbon films through combustion flame synthesis at atmospheric pressure is a method of fascinating simplicity.[26–35] The flame ensures a chemically reactive environment capable of generating carbon nanostructures in a short and continuous single-step process.[36] Moreover, it has been demonstrated that candle flame consists of four major forms of carbon (diamond, graphite, fullerenes, amorphous carbon), which can be successfully identified using anodic aluminum oxide collectors.[30] Unfortunately, this approach has not yet been extensively used for industrial purposes, because of a few limiting factors. Firstly, to achieve desirable physicochemical properties of the flame-deposited carbon coatings, additional catalysts or chemical reagents may be required, which complicates the process.[34,37–39] Secondly, up to now, the formation of amorphous DLC from various flame configurations and fuel types has been observed only at high substrate temperatures (above 400 °C), which in turn can limit the applicability of the method to materials with low thermal stability.[27,28,32,40]

Here, we present an efficient single-step flame method for the deposition of carbon coatings, whose physicochemical characteristics can be easily manipulated using a conical chimney with an adjustable air-inlet opening. In this study, carbon nanostructures with superhydrophobic or diamond-like properties are derived during the incomplete combustion of rapeseed oil. This is achieved through a precise control of the amount of oxygen involved in the combustion, and subsequently the temperature of the flame, by changing the size of the opening. The major advantage of our approach is the opportunity to tune *in situ* the fraction of amorphous, graphitic-like and diamond-like phases, allowing for the deposition of carbon coatings with substantially different structure and chemical reactivity. Moreover, the proposed method is catalyst-free and does not require high substrate temperatures (see Section 3.1), which is of crucial importance for its wide practical applicability.

2. Experimental procedure

2.1. Synthesis of the carbon nanoparticles and experimental details

A custom-designed aluminum chimney with an adjustable air-inlet opening, illustrated in Fig. 1, was mounted over an inflamed paper wick soaked in rapeseed oil. The size of the opening was controlled through a circular cover with a diameter of $d = 6$ cm, which was wrapped around the chimney. This cover was used to tune the inlet oxygen flowing through the narrow 1.5 × 2.5 cm opening, available at the bottom of the chimney. Altering the position of the cover towards the opening allowed *in situ* manipulation of the combustion process and subsequent synthesis of carbon nanoparticles with different fraction of amorphous, graphitic-like or diamond-like phases.

Based on the experimental setup, three distinct combustion regimes were established when the opening was fully-open (1.5 × 2.5 cm), half-open (0.75 × 2.5 cm) and fully-closed. The latter cancelled most of the oxygen flow, but since the chimney was not completely sealed (upon closure, a small ~0.5 cm gap remains between the cover and chimney's bottom); the combustion remained continuous, as there was enough oxygen to make the process self-sustaining. After ignition of the fuel (rapeseed oil), square shaped 2.5 × 2.5 cm microscope glass slides (Fisher Scientific, USA), as well as gold electrode quartz crystal microbalances (QCMs) with a fundamental frequency of ~5 MHz (SRS, USA) were exposed over the chimney's tip at each regime of combustion, which caused deposition of carbon coatings with various physicochemical characteristics. The film deposition was carried out at burner-to-substrate distance of 7 cm with time duration ranging within 20–60 s, similarly as in our previous work.[35] The flame and substrate temperatures were determined using a TP3001 digital thermometer and Kintrex IRT0421 infrared thermal sensor, respectively. For that purpose, the probe of digital thermometer was placed in the flame, keeping similar distance from the burner (the chimney) such as during the film deposition. The flame temperature was recorded after reaching stable temperature reading, which was obtained for ~60 s. In addition, the substrate temperature at each combustion regime was measured through the infrared thermometer coincidently with the deposition process.

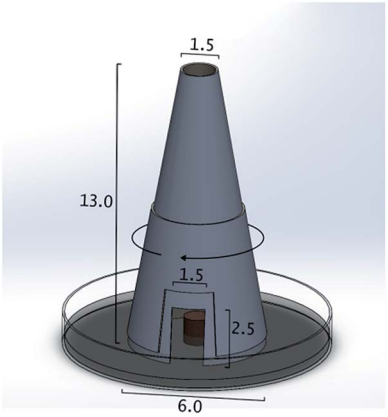

Fig. 1 Schematic representation of the conical chimney with adjustable opening used to synthesize the carbon nanoparticles. The units are given in centimeters.

2.2. Surface characterization

After the synthesis of particles and subsequent fabrication of the coatings, their morphology, structure, roughness and chemical composition were investigated using scanning electron microscopy (SEM), X-ray diffraction (XRD), atomic force microscopy (AFM), Raman spectroscopy, X-ray photoelectron spectroscopy (XPS) and transmission electron microscopy (TEM). The SEM experiments were performed using a Hitachi SU-70 Field Emission Scanning Electron Microscope and images were taken at low and high magnifications up to 150k. The XRD measurements were carried out with a Panalytical X'Pert Pro diffractometer operating in Bragg–Brentano mode. An incident X-ray beam was generated with Cu Kα radiation ($\lambda = 1.54$ Å) and the samples were scanned from 5° to 60° of 2θ, at 0.03° scan step size, 2° anti-scatter slit, 1° fixed divergence slit and 15 mm mask. AFM images were taken in

tapping mode in an area of 1 × 1 μm at a rate of 0.4 Hz with Bruker BioScope Catalyst. Raman spectra of the coatings, deposited at the three distinct regimes, were recorded from 500 to 2500 cm^{-1} with an acquisition time of 300 s in a Horiba LabRam HR Evolution Confocal Raman spectrometer, using a 20 mW/532 nm He–Ne laser excitation system. TEM was implemented by a Zeiss Libra 120 system operating at 120 kV with a point to point resolution of 0.34 nm. The high-resolution XPS data were collected with a Thermo Fisher ESCALAB 250 X-ray photoelectron spectrometer at a step of 0.1 eV.

2.3. Determination of the physical properties of carbon coatings and their thickness

The electrical resistivity (σ), apparent density (ρ), surface wettability and the thickness of as prepared coatings were determined in several experiments. Four point probe analysis was used for quantitative evaluation of the electrical resistivity of the carbon coatings.[41] For this purpose, an auto-mechanical stage with four equally spaced tungsten metal tips was moved in upward and downward direction. Simultaneously, a high impedance current source was used to supply current through the outer two metal tips, while a voltmeter was measuring the voltage across the two inner probes. The apparent density was defined as a ratio of the mass of the coatings, deposited on 2.5 × 2.5 cm glass slides, towards their volume (thickness). The latter was measured using an optical microscope Nikon eclipse LV100, equipped with a motorized stage ProScan II capable of providing precise focus control by moving the *Z*-axis in steps as small as 20 nm. Finally, the wettability of the samples was determined through static contact angle (SCA) and contact angle hysteresis (CAH) measurements for droplets of de-ionized water using a Drop Shape Analyzer (DSA 25E, Krüss Germany).

2.4. Proof-of-concept experiments

The hypothesis that the physicochemical performance of carbon coatings, including their chemical reactivity, depends on the ratio of sp^2/sp^3 bonds and the quantity of heteroatoms[2] was verified experimentally with nine QCM based chemical sensors. Initially, the QCMs with gold electrode structure, 1 inch diameter and a fundamental frequency of ~5 MHz were separated in three groups of three sensors. The first group devices was coated with carbon nanostructures through combustion flame synthesis at fully-open, the second at half-open and the third at fully-closed opening, respectively (see Section 2.1). For each combustion regime, the deposition time was appropriately selected in order to ensure as reproducible as possible film thicknesses from device to device. Subsequently, the QCMs were mounted one at a time in a quartz crystal holder connected to a sensor oscillator SRS25, used to ensure continuous crystal oscillations, and a QCM200 digital controller with a built-in frequency counter. The chemical reactivity of the coatings was investigated by measuring the frequency response of each individual sensor in air and after covering the sensing surface with organic solvents such as ethanol and isopropanol (99%, Sigma-Aldrich). These chemicals were dissolved in de-ionized water, leading to aqueous solutions in the concentration range of 0–12.5 wt%. By analyzing the differences in the frequency response between each group of sensors, it was possible to assess whether the reduction of oxygen affects the chemical reactivity of the coatings. The experiments were performed at constant room temperature in an open lab; therefore,

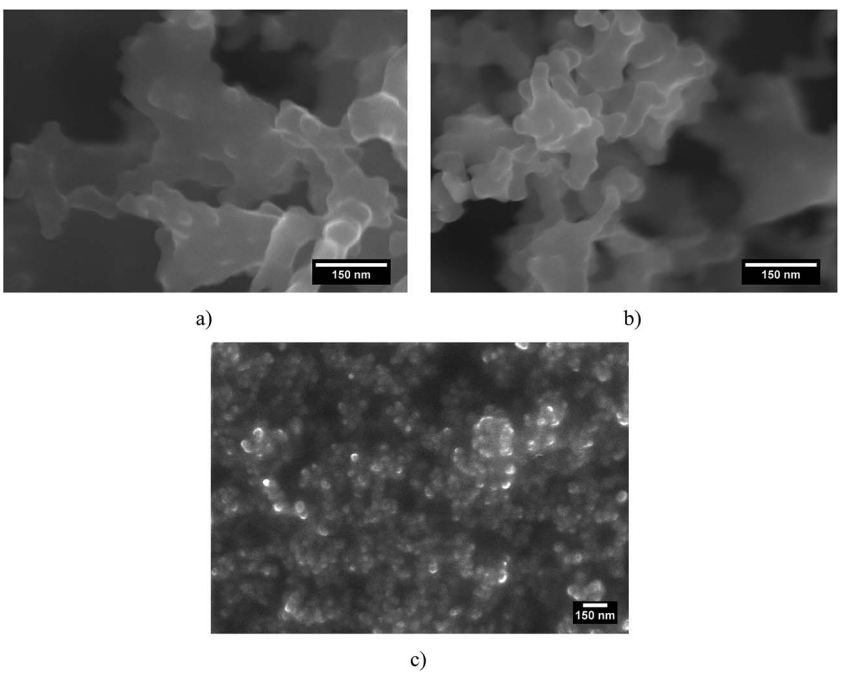

Fig. 2 SEM images of carbon coatings deposited at combustion regime with (a) fully-open, (b) half-open and (c) fully-closed opening.

any possibility for thermally-induced frequency shifts was avoided.[42]

3. Results and discussion

3.1. Morphological and structural analysis

Fig. 2 compares the structural and morphological peculiarities of the coatings deposited at three distinct regimes of combustion. The SEM images show that the first two regimes trigger the formation of elongated carbon nanoparticles assembled as islands, separated by micro- and nanoscale pores. Moreover, these particles are disordered, tightly bonded and fused, which corresponds to inherently robust and durable amorphous carbon soot with superhydrophobic properties.[35] In contrast, the image in Fig. 2c reveals a significantly different orientation, shape and size of the particles. They occur as grain clusters with an approximate size of 200 nm. A similar surface profile has previously been observed for diamond-like carbon (DLC), fabricated using ion beam[6] and RF plasma deposition,[43] although the graininess achieved with these methods is much more pronounced. The comparative analysis of our SEM results with those reported for ion beam[6] and RF plasma deposition[43] suggests that at the regime of fully-closed opening (Fig. 2c) the uncombusted polyaromatic hydrocarbons may have precipitated as amorphous DLC films. This hypothesis is supported by our XRD measurements (see the ESI†), which indicate a mainly amorphous structure of the fabricated coatings.

Since such a structural transition has not previously been reported and the reaction mechanism of soot formation in flames is not completely elucidated,[44,45] it is extremely difficult to provide an exact and comprehensive scientific interpretation of our observations. However, a fairly reasonable explanation of the soot-DLC transformation may come up from the detailed kinetic modeling of soot aggregate formation in laminar premixed flames.[46] According to this model, the soot particle morphology is strongly influenced by the interplay between soot's nucleation, aggregation and initial surface growth that depend on the equivalence fuel/oxygen ratio. In the nucleation region of the flame, the freshly nucleated particles collide, which leads to the formation of fractal aggregates. As the nucleation rate diminishes (at low equivalent ratios *i.e.* large air fraction) and the surface growth becomes prominent, the aggregated particles acquire a spherical shape.[46] In contrast, upon enhanced nucleation at relatively constant surface growth rate, the morphology of the clusters formed through collisions of the incipient particles is significantly altered. As a result, the degree of particles' overlap increases vastly, possibly inducing structural changes in the soot. Such a phenomenon is associated with the increased equivalence fuel/oxygen ratio (reduced oxygen content), which increases the fraction of uncombusted polyaromatic hydrocarbons and triggers more intensive nucleation.[46] In our approach, we manipulate the inlet oxygen flow, and thus the reaction temperature, by changing the size of the opening. At fully-open opening, the substrate temperature after 60 s exposure to the flame at burner-to-substrate distance of 7 cm is ~160 °C and decreases up to ~60 °C upon closing the opening (keeping the same exposure time and distance). Simultaneously, by passing from the first to third

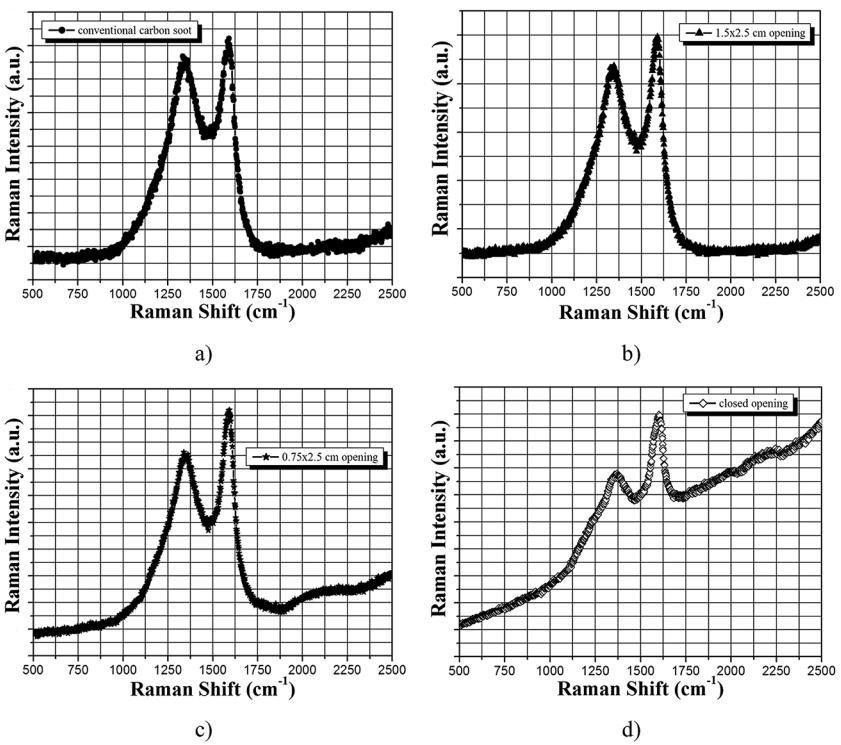

Fig. 3 Raman spectra of (a) conventional carbon soot (deposited without chimney) and after modification with chimney at (b) fully-open, (c) half-open and (d) fully-closed opening.

combustion regime the flame temperature decreases from ~275 °C to ~200 °C, respectively. This observation correlates well with the kinetic model of soot formation[46] and the fundamentals of combustion,[47] as the reduced oxygen content will result in an increased fuel/oxygen ratio and decreased heat production in the subsequent exothermic chemical reaction. Based on the above considerations, it is likely that at fully-closed opening the nucleation rate in the fume enhances, promoting the morphological changes in the soot *i.e.* its transformation to amorphous DLC.

3.2. Chemical state analyses

The SEM imaging was followed by Raman spectroscopy and XPS analyses, summarized in Fig. 3 and 4.

Carbon soot fabricated by the conventional (with no chimney) method has been included too in order to assess how each combustion regime (see Section 2.1) affects the chemical bonds in the coatings. According to Fig. 3, the Raman spectrum of amorphous carbon consists of two distinct bands. The first one at 1596 cm^{-1} corresponds to an ideal graphitic lattice vibration mode and is denoted as G-band, while the second one, situated at around 1360 cm^{-1}, is associated with the A_{1g} symmetry mode of disordered graphitic lattice located at the edges of the graphene layer and is called D-band.[34,48] Qualitative characterization of the sp^2/sp^3 fraction in the coatings can be implemented by analyzing the intensity changes of G- and D-peaks. As seen in Fig. 3a, the conventional carbon soot is characterized with almost equal intensity of both peaks and the I_D/I_G ratio is 0.94. This result correlates well with previously reported I_D/I_G values for amorphous black carbon.[34,48,49] The chimney modification leads to a gradual reduction of the D-peak's intensity, which is an indication of carbon coatings with an increased sp^3 content.[43] Moreover, at fully-closed opening (Fig. 3d), the I_D/I_G ratio is 0.81, corresponding to a coating with ~14% less defects compared to the conventional carbon soot. Fig. 4 represents the high-resolution XPS to the C1s for the coatings synthesized at fully-open, half-open and fully-closed opening of the chimney. The deconvolution of the C1s regions is achieved with several peaks corresponding to sp^2 hybrid form of carbon at 284.8 ± 0.4 eV, sp^3 hybridized carbon at 285 ± 0.1 eV, hydroxyl groups (C–O) at 286.5 ± 0.6 eV, carbonyl groups (C═O) at 288.9 ± 0.5 eV and π–π* satellite group at 291 ± 2 eV. Upon reducing the chimney's opening and its subsequent closure, the sp^2/sp^3 ratio in the coatings is altered significantly; from 1.27 at fully-open to 0.048 at fully-closed opening, corresponding to coatings with ~80% sp^3 content. Moreover, the nanostructures deposited at the third regime do not contain π–π* satellite peak associated with an electronic structure rearrangement of transition between the π bonding and π*

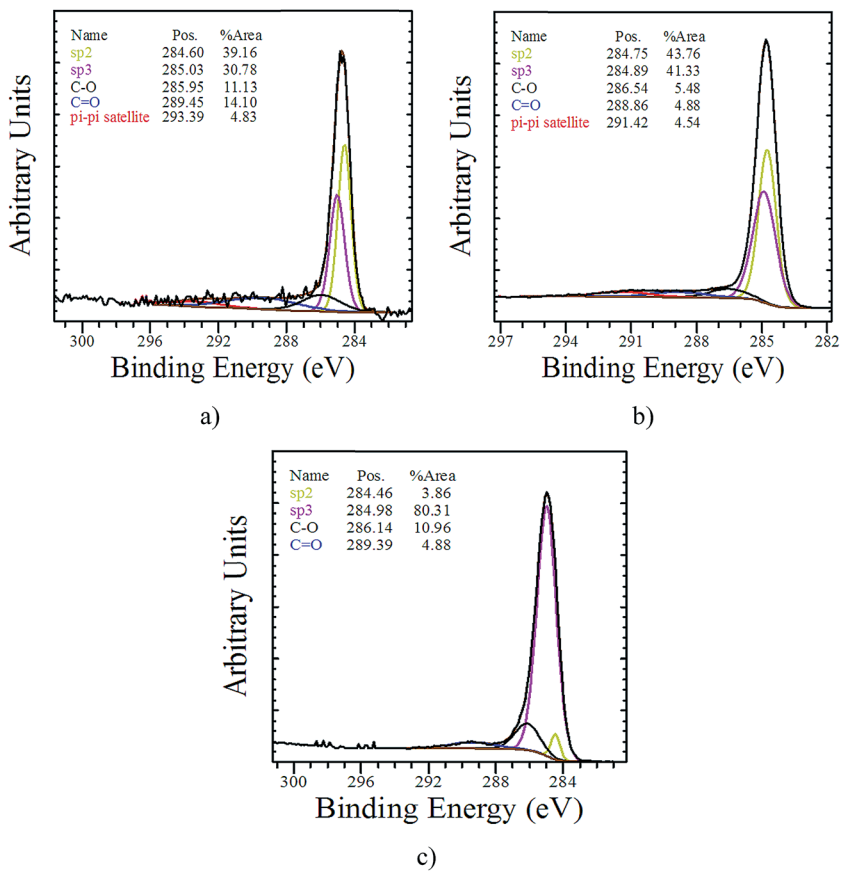

Fig. 4 C 1s photoelectron core level of carbon coatings deposited after modification with chimney at (a) fully-open, (b) half-open and (c) fully-closed opening.

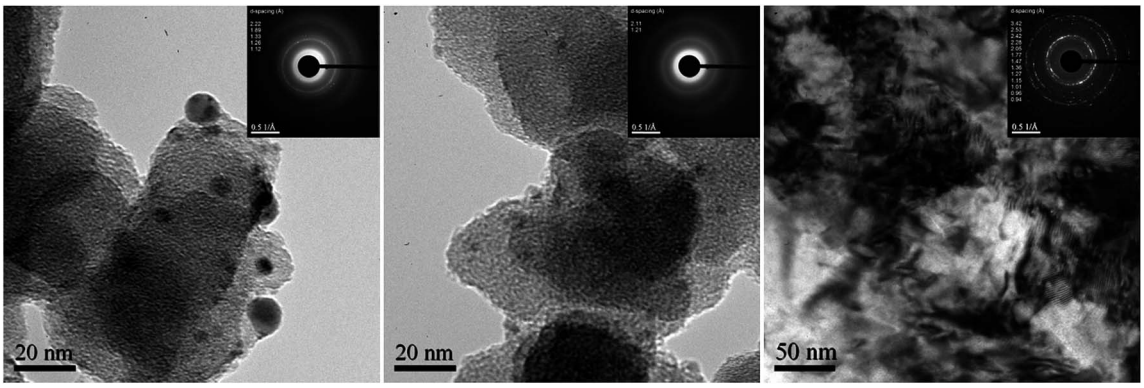

Fig. 5 HRTEM and SAD images of (a) conventional carbon soot (deposited without chimney) and after modification with chimney at (b) fully-open and (c) fully-closed opening.

antibonding states. Also, Fig. 4c shows a more symmetric shape of the C 1s compared to Fig. 4a and b, which is an additional implication that the electronic structure does not suffer rearrangement effects from sp^2 hybridized bonds. Furthermore, the oxygenated functional groups in the layers increase by a factor of 2 when switching from half-open to fully-closed opening. These observations are in good agreement with the scan survey of the coatings (see the ESI†).

Finally, the as prepared carbon coatings were examined through high-resolution transmission electron microscopy (HRTEM) and selected area electron diffraction (SAD), shown in Fig. 5.

The TEM images in Fig. 5 represent the morphological features of the coatings obtained with and without chimney. The conventional soot (without chimney) is characterized with a spherical-like morphology and some lattice fringes could be identified for the larger spheres (>20 nm). In addition, the *d*-spacing is not homogeneous along the structures, suggesting a short-range order. Smaller spheres do not present any order, indicating mostly amorphous phase. Also, the SAD pattern showed in Fig. 5a exhibits a few continuous rings and some diffused halos on the sample, which are consistent with the HRTEM image. Similarly, after modification with chimney at fully-open air-inlet opening, an onion-like shape of the particles is observed for most of the areas in the soot and the SAD pattern shows mainly two diffused halos corresponding to a short-range order (Fig. 5b). In this case, the two rings can be assigned to graphitic-like nanostructures.

In contrast, the TEM image in Fig. 5c illustrates more crystalline structure of the coating deposited at fully-closed air-inlet opening. Denser structures with large nanocrystals embedded in an amorphous phase are observed. This morphology differs from the sphere-like and the rings in the SAD pattern are well defined. The atomic *d*-spacings in the coating, synthesized at fully-closed opening, can be matched to both graphitic-like and diamond-like structures with less amorphous phase in overall. A summary of these measurements along with the STD *d*-spacing for diamond and graphite is presented in Table 1. Although graphitic-like structures are still present, the appearance of more sp^3 carbon bonds (see Fig. 4c) along with the evidence of nanocrystalline diamond formation (see Table 1) imply that the regime of fully-closed opening tends to form diamond-like carbon (DLC) structures.

3.3. Physical properties of the carbon coatings

After full characterization of the carbon nanostructures, their electrical resistivity (σ), apparent density (ρ), surface wettability and thickness were defined experimentally. The coatings synthesized at fully-closed opening showed an electrical resistivity of $\sigma = 3.6 \times 10^5$ Ω cm, which is two orders of magnitude higher compared to the values for the conventional soot ($\sigma = 1$–1.2×10^3). Furthermore, the apparent density of the latter is calculated to be $\rho \sim 0.04$ g cm^{-3}, similar to the data reported for superamphiphobic layers based on carbon soot.[50] In

Table 1 Comparison between the *d*-spacing (Å) calculated from SAD patterns for conventional soot and after modification with chimney at fully-open and fully-closed opening, and STD *d*-spacings for diamond and graphite

d-Spacing measured (Å)			*d*-Spacing for some C allotropes	
Conventional carbon soot	Fully-open opening	Fully-closed opening	Diamond	Graphite
		3.42		**3.4**
		2.53		
		2.42		
2.22		2.28		
	2.11	**2.05**	**2.06**	**2.04**
1.89		**1.77**		**1.7**
		1.47		
1.33		1.36		
1.26		**1.27**	**1.26**	
1.12	1.21	**1.15**		**1.2**
		1.01	**1.07**	
		0.96	**0.98**	
		0.94		

comparison, the short-range ordered DLC nanostructures possess density of ~0.59 g cm^{-3}, indicating decreased porosity. Moreover, the third regime promotes hydrophilic behavior of the coatings determined by low SCA and high CAH of 70° and 20°, respectively. In contrast, the soot exhibits super-hydrophobicity with SCA and CAH being 155° and 0.5°, respectively. These values are another evidence for the observed soot-to-DLC transformation, since the sp^3-hybridized diamond-like carbon is hydrophilic in nature due to its high surface energy dominated by the covalent character of the sp^3 bonds.[51] In addition, all carbon coatings demonstrate linear relationship of their thickness towards the deposition time (see the ESI†). The DLC nanostructures have small thickness of ~10 μm, while the carbon soot coatings are characterized with much larger thickness of ~75–125 μm depending on the combustion regime (fully-open or half-open opening). This is attributed to the major differences in the film deposition rate by switching from 1^{st} to 3^{rd} combustion regime. At fully-open opening, the deposition rate is ~1.5 μm s^{-1} and increases up to 2 μm s^{-1} at the second regime, which accounts for the reduced oxygen content that degrades the efficiency of combustion and produces more soot.[47] On the other hand, at fully-closed opening the deposition rate is only about 0.25 μm s^{-1}, meaning that at this stage the combustion process is significantly altered, as it is confirmed by the surface characterization analyses.

3.4. Chemical reactivity assessment

The chemical reactivity of the carbon coatings was assessed through the changes in sensor response of three QCM groups, prior to and after immersion in aqueous ethanol and isopropanol solutions. The choice of these chemicals is related to their practical relevance and harmful impact on the human health when ingested above a certain concentration.[52] Also, both compounds possess similar density, viscosity and surface tension; therefore, the expected differences in the sensor signal from group to group would be ascribed to the quantity of heteroatoms in the film rather than the physical properties of the liquids. Last but not least, as it is pointed in Section 2.4, the carbon nanostructures were deposited in a way ensuring approximately equal film thickness from device to device; thus minimizing the possibility for thickness (mass loading) induced sensitivity deviations that may compromise the validity of the comparisons.[53,54] For the first two regimes, the film thickness is ~40 ± 3 μm, while at fully-closed opening it is around 10 ± 1 μm. These values along with the density of carbon materials gave relatively similar mass loading expressed through frequency downshifts within 700–870 Hz. Based on the above considerations, the chemical reactivity of the conventional carbon soot is not considered in the research, since this material is inherently brittle and needs additional stabilization using various stabilizers.[35] Thus, the overall massloading on the sensor surface, caused by the stabilizers, would change the QCM's sensitivity, which would compromise the comparative analysis.[54]

Fig. 6 displays the liquid phase frequency response of each QCM group towards aqueous ethanol and isopropanol solutions in the concentration range of 0–12.5 wt%. The first major distinction in the chemical reactivity of the samples is identified upon immersion in de-ionized water (0 wt%). As seen, the QCMs coated with carbon soot (fully-open and half-open opening) decrease their resonance frequency with $\Delta f \sim$ 150–250 Hz, corresponding to three to five times lower frequency shift in comparison with the theoretical model for an uncoated QCM.[55] On the other hand, the dynamic resistance of these sensors (not shown here) remains relatively constant. Such resonance behavior is attributed to a phenomenon called "decoupling of the liquid phase sensor response". This effect occurs due to the strong reflection boundary at the solid–air interface, arisen from the "air plastron" of the super-hydrophobic carbon soot, leading to lower amount of energy interacting with the liquid.[56]

Moreover, as evident from Fig. 6, the quantity of heteroatoms in the soot coatings is crucial for their chemical reactivity. The nanostructures fabricated at the first combustion regime have twice more polar functional groups (C–OH) compared to those at the second regime (see Fig. 4). Thus, the first group QCMs exhibits higher sensor response to de-ionized water, as more oxygen atoms available on the sensing surface, more hydrogen bonds would be formed (see Fig. 6a and b). Such a process will increase the overall mass loading on the surface, which will result in additional frequency downshift, according to the Sauerbrey equation.[57] In addition, the sensors coated with DLC

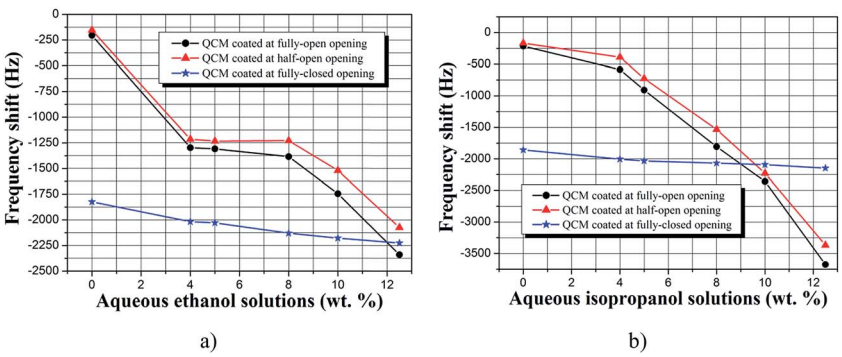

Fig. 6 Frequency response of each sensor group to aqueous solutions of (a) ethanol and (b) isopropanol in the concentration range of 0–12.5 wt%.

Table 2 Sensitivity and detection limit of each QCM group towards aqueous ethanol and isopropanol solutions

QCM group	Target analyte	ΔC (mg mL^{-1})	Δf (Hz)	$\Delta f/\Delta C$ (Hz mg^{-1} mL^{-1})	Detection limit (mg mL^{-1} s^{-1})
1	Ethanol	121	2135	17.6	0.85
2		121	1920	15.9	0.94
3		121	401	3.3	4.5
1	Isopropanol	121	3462	28.6	0.52
2		121	3201	26.5	0.57
3		121	292	2.4	6.25

decrease their resonance frequency with more than 1800 Hz after immersion in de-ionized water. This observation correlates well with the increased amount of oxygenated functional groups in the DLC nanostructures. As shown by the XPS analysis, the C–O content in the coatings increases by a factor of two upon passing from half-open to fully-closed opening of the chimney.

The second difference in the chemical performance of the coatings is expressed through the overall resonance behavior of the sensors. For instance, the soot coated QCMs (the first two regimes) demonstrate a non-linear frequency shift when the ethanol concentration increases from 0 to 12.5 wt%. Moreover, there is a large 1.3 kHz step change at 4 wt% followed by a relatively constant sensor signal up to 8 wt%. In comparison, the step change to isopropanol is only 400 Hz and further increase in its concentration causes a proportional quasilinear frequency response. Last but not least, regardless of the chosen chemical, the coatings synthesized at half-open opening exhibit weaker chemical reactivity compared to those deposited at fully-open opening. These results imply that the main chemical reaction is of oxygen–hydrogen type; therefore the coatings with less heteroatoms (oxygen) induce lower sensor signal. Also, isopropanol has more hydrogen molecules compared to ethanol, leading to higher sensitivity of the QCM. As seen, the coatings deposited at the first combustion regime exhibit ~1.6 times higher sensitivity to isopropanol in comparison with that to ethanol ($\Delta f_{C_2H_5OH} \sim 2350$ Hz while $\Delta f_{C_3H_8O} \sim 3750$ Hz). Similar trend is observed for the layers precipitated at the second regime (see Fig. 6). Furthermore, the concentration of 12.5 wt% appears to be a threshold, at which the soot loses superhydrophobicity and the resonance frequency does not recover its initial value (baseline). This effect is associated with a wetting state transition from the suspended Cassie–Baxter to the "sticky" Wenzel state due to a chemical and structural modification of the surface caused by ethanol and isopropanol[58] (see also the ESI†). However, the carbon soot could restore its water repellency by additional hydrophobic chemical treatment, which makes this material appropriate for multiple usages in QCM based gas or liquid sensors.[14,15,58]

In complete contrast, the DLC coated QCMs recover their resonance frequency with negligible deviations from the baseline within ±1 Hz and demonstrate relatively constant sensitivity regardless of the chosen chemical. Such behavior is expected since the DLC coatings are chemically inert, meaning that their surface structure remains unaltered upon contact with 12.5 wt% of ethanol or isopropanol. Moreover, this material is smooth on a nanometric scale, which reduces the number of active adsorption sites interacting with the liquid. The root mean square roughness (R_{rms}) estimated through AFM is $R_{rms} =$ 37 nm, indicating ~3–3.5 times smoother surface profile compared to the carbon soot[14,15,35] (see the ESI†). Although DLC is characterized with an increased quantity of oxygenated functional groups, the total number of active sites is reduced. Therefore, the quantity of hydrogen molecules interacting with the layer would be the same despite of the molecular weight of the chemicals (ethanol or isopropanol).

For the sake of completeness, we determined the detection limit of the sensors and the results are summarized in Table 2.

The sensitivity is defined as the frequency change Δf towards the target analyte concentration change ΔC and along with the sensor's short-term stability determines its detection limit.[59] In this study, during the liquid-phase measurements, the resonance frequency was stabilized within ±1–5 Hz s^{-1}. Therefore, the noise level was estimated at its maximum of ±5 Hz s^{-1}, while the signal-to-noise ratio was 3 : 1. Since the capacity of the quartz crystal holder is approximately 1 mL, 12.5 wt% of ethanol and isopropanol are corresponding to ~121 mg mL^{-1}. As evident from Table 2, the soot coated 5 MHz QCMs yield detection limit to ethanol up to 850 μg mL^{-1}, which is ~2 times higher resolution in comparison to their uncoated QCM counterparts.[58] Although our sensors do not provide resolution of ng mL^{-1} or pg mL^{-1}, further optimization of the signal-to-noise ratio would provide lower detection limit.[59]

4. Conclusions

In this paper, we described a novel and efficient single-step flame method for deposition of carbon coatings with substantially different physical and chemical characteristics. This was achieved using a conical chimney with an adjustable air-inlet opening, mounted over an ignited wick immersed in rapeseed oil. The opening was used for *in situ* manipulation of the combustion process and subsequent fabrication of nanostructures with different content of amorphous, graphitic-like and diamond-like phases. The SEM and TEM analyses revealed the formation of coatings with distinct morphology; from tightly connected and fused nanoparticles, to grain clusters with approximate size of 200 nm and short-ordered nanocrystalline diamond structure. Such a structural diversity was associated with soot-to-DLC transformation triggered by the

increase of the equivalence fuel/oxygen ratio. In addition, the Raman Spectroscopy and XPS showed that the DLC coatings are characterized with low D-band intensity and ~80% of sp^3 bonds. Furthermore, these layers were found to possess hydrophilicity, whereas their soot counterparts exhibited superhydrophobicity with SCA and CAH being 155° and 0.5°, respectively. Also, the coatings deposited at fully-closed opening were thinner, denser and less conductive compared to the soot. Finally, major differences in the chemical reactivity of as prepared nanostructures were observed by analyzing the frequency response of three groups of 5 MHz QCMs, upon immersion in aqueous ethanol and isopropanol solutions. The frequency shift of the soot coated sensors was strongly influenced by the presence of polar C–OH groups, as well as the molecular weight of the chemicals. In contrast, the DLC coated QCMs exhibited relatively constant sensor signal regardless of the analyte, which was attributed to their smooth surface and reduced amount of active adsorption sites. Our investigations are prerequisite for rapid and inexpensive fabrication of carbon coatings with custom physicochemical properties.

Acknowledgements

The authors wish to gratefully acknowledge the research group of Prof. Hadis Morkoc at the VCU Department of Electrical and Computer Engineering for implementing the four point probe analysis. Services in support of the project were provided by the VCU Massey Cancer Center, supported in part with funding from NIH-NCI P30CA016059. Also, the startup support from Virginia Commonwealth University under grant 137422 is greatly acknowledged.

References

1 D. R. McKenzie, *Rep. Prog. Phys.*, 1996, **59**, 1611–1664.
2 J. A. Menendez-Diaz and I. Martin-Gullon, *Activated carbon surfaces in environmental remediation*, ed. T. J. Bandosz, Elsevier, 2006, pp. 1–48, ch. 1.
3 J. C. Anqus and C. C. Hayman, *Science*, 1988, **241**, 913–921.
4 M. Chhowalla, J. Robertson, C. W. Chen, S. R. P. Silva, C. A. Davis, G. A. J. Amaratunga and W. I. Milne, *J. Appl. Phys.*, 1997, **81**, 139–145.
5 J. Robertson, *Mater. Sci. Eng., R*, 2002, **37**, 129–281.
6 P. K. Chu and L. Li, *Mater. Chem. Phys.*, 2006, **96**, 253–277.
7 C. R. Lin, H. M. Chang and C. K. Chang, *Int. J. Photoenergy*, 2013, **2013**, 612163.
8 N. Dwivedi, S. Kumar, J. D. Carey, R. K. Tripathi, H. K. Malik and M. K. Dalai, *ACS Appl. Mater. Interfaces*, 2013, **5**, 2725–2732.
9 D. Liu, P. Yuan, D. Tan, H. Liu, M. Fan, A. Yuan, J. Zhu and H. He, *Langmuir*, 2010, **26**, 18624–18627.
10 F. Xu, Z. Tang, S. Huang, L. Chen, Y. Liang, W. Mai, H. Zhong, R. Fu and D. Wu, *Nat. Commun.*, 2015, **6**, 7221.
11 J. Huang, J. Wang, C. Wang, H. Zhang, C. Lu and J. Wang, *Chem. Mater.*, 2015, **27**, 2107–2113.
12 D. S. Su and R. Schlogl, *ChemSusChem*, 2010, **3**, 136–168.
13 S. Suganuma, K. Nakajima, M. Kitano, D. Yamaguchi, H. Kato, S. Hayashi and M. Hara, *J. Am. Chem. Soc.*, 2008, **130**, 12787–12793.
14 K. D. Esmeryan, T. A. Yordanov, L. G. Vergov, Z. G. Raicheva and E. I. Radeva, *IEEE Sens. J.*, 2015, **15**, 6318–6325.
15 K. D. Esmeryan, V. Georgieva, L. Vergov and J. Lazarov, *Bulg. Chem. Commun.*, 2015, **47**, 1039–1044.
16 H. Zhu, J. Wei, K. Wang and D. Wu, *Sol. Energy Mater. Sol. Cells*, 2009, **93**, 1461–1470.
17 R. Hauert, K. Thorwarth and G. Thorwarth, *Surf. Coat. Technol.*, 2013, **223**, 119–130.
18 C. A. Love, R. B. Cook, T. J. Harvey, P. A. Dearnley and R. J. K. Wood, *Tribol. Int.*, 2013, **63**, 141–150.
19 L. Wei, M. Sevilla, A. B. Fuertes, R. Mokaya and G. Yushin, *Adv. Funct. Mater.*, 2012, **22**, 827–834.
20 Z. H. Li, D. C. Wu, Y. R. Liang and R. W. Fu, *J. Am. Chem. Soc.*, 2014, **136**, 4805–4808.
21 M. Bojiang and Y. Qingxian, *Appl. Surf. Sci.*, 2012, **258**, 4750–4755.
22 G. Matenoglou, G. A. Evangelakis, C. Kosmidis, S. Foulias, D. Papadimitriou and P. Patsalas, *Appl. Surf. Sci.*, 2007, **253**, 8155–8159.
23 A. Ibenskas, A. Galdikas, S. Meskinis, M. Andrulevicius and S. Tamulevicius, *Diamond Relat. Mater.*, 2011, **20**, 693–702.
24 O. Durand-Drouhin, M. Benlahsen, M. Clin and R. Bouzerar, *Appl. Surf. Sci.*, 2004, **223**, 269–274.
25 K. D. Esmeryan, E. I. Radeva and I. D. Avramov, *J. Phys. D: Appl. Phys.*, 2016, **49**, 025309.
26 W. A. Carrington, L. M. Hanssen, K. A. Snail, D. B. Oakes and J. E. Butler, *Metall. Trans. A*, 1989, **20**, 1282–1284.
27 L. M. Hanssen, K. A. Snail, W. A. Carrington, J. E. Butler, S. Kellogg and D. B. Oakes, *Thin Solid Films*, 1991, **196**, 271–281.
28 I. Doi, M. S. Haga and Y. E. Nagai, *Diamond Relat. Mater.*, 1999, **8**, 1682–1685.
29 M. Qu, J. He and B. Cao, *Appl. Surf. Sci.*, 2010, **257**, 6–9.
30 Z. Su, W. Zhou and Y. Zhang, *Chem. Commun.*, 2011, **47**, 4700–4702.
31 X. Deng, L. Mammen, H. J. Butt and D. Volmer, *Science*, 2012, **335**, 67–70.
32 H. M. Zhu, S. M. Lei and T. C. Kuang, *Adv. Mater. Res.*, 2013, **750–752**, 2100–2103.
33 K. Seo, M. Kim and D. H. Kim, *Carbon*, 2014, **68**, 583–596.
34 B. N. Sahoo and B. Kandasubramanian, *RSC Adv.*, 2014, **4**, 11331–11342.
35 K. D. Esmeryan, C. E. Castano, A. H. Bressler, M. Abolghasemibizaki and R. Mohammadi, *Appl. Surf. Sci.*, 2016, **369**, 341–347.
36 W. M. Merchan, A. V. Saveliev, L. Kennedy and W. C. Jimenez, *Prog. Energy Combust. Sci.*, 2010, **36**, 696–727.
37 K. Saito, A. S. Gordon, F. A. Williams and W. F. A. Stickle, *Combust. Sci. Technol.*, 1991, **80**, 103–119.
38 R. L. Vander Wal, L. J. Hall and G. M. Berger, *J. Phys. Chem. B*, 2002, **106**, 13122–13132.
39 R. L. Vander Wal, *Combust. Flame*, 2002, **130**, 37–47.
40 H. Zhu, T. Kuang, B. Zhu, S. Lei, Z. Liu and S. P. Ringer, *Nanoscale Res. Lett.*, 2011, **6**, 331.

41 A. P. Schuetze, W. Lewis, C. Brown and W. J. Geerts, *Am. J. Phys.*, 2004, **72**, 149–153.
42 K. D. Esmeryan, I. D. Avramov and E. I. Radeva, *Sens. Actuators, B*, 2015, **216**, 240–246.
43 V. S. Yadav, D. K. Sahu, M. Singh and K. Kumar, *Proc.–World Congr. Eng. Comput. Sci.*, 2009, **1**, 78–81.
44 O. I. Smith, *Prog. Energy Combust. Sci.*, 1981, **7**, 275–291.
45 M. Frenklach, *Phys. Chem. Chem. Phys.*, 2002, **4**, 2028–2037.
46 M. Balthasar and M. Frenklach, *Combust. Flame*, 2005, **140**, 130–145.
47 S. P. Burke and T. E. W. Schumann, *Ind. Eng. Chem.*, 1928, **20**, 998–1004.
48 A. Sadezky, H. Muckenhuber, H. Grothe, R. Niessner and U. Pöschl, *Carbon*, 2005, **43**, 1731–1742.
49 Y. Gao, Y. S. Zhou, W. Xiong, M. Wang, L. Fan, H. Rabiee-Golgir, L. Jiang, W. Hou, X. Huang, L. Jiang, J. F. Silvain and Y. F. Lu, *ACS Appl. Mater. Interfaces*, 2014, **6**, 5924–5929.
50 M. Paven, P. Papadopoulos, L. Mammen, X. Deng, H. Sachdev, D. Vollmer and H. J. Butt, *Pure Appl. Chem.*, 2014, **86**, 87–96.
51 Y. Zhou, X. Song, E. Li, G. Li, S. Zhao and H. Yan, *Appl. Surf. Sci.*, 2006, **253**, 2690–2694.
52 D. Jammalamadaka and S. Raissi, *Am. J. Med. Sci.*, 2010, **339**, 276–281.
53 D. S. Ballantine Jr, S. J. Martin, A. J. Ricco, G. C. Frye, H. Wohltjen, R. M. White and E. T. Zellers, *Acoustic wave sensors: theory, design and physico-chemical applications*, Elsevier, 1st edn, 1997, pp. 222–230, ch. 5.
54 G. McHale, M. I. Newton and F. Martin, *J. Appl. Phys.*, 2003, **93**, 675–690.
55 K. K. Kanazawa and J. G. Gordon, *Anal. Chem.*, 1985, **57**, 1770–1772.
56 G. McHale, P. Roach, C. R. Evans, N. J. Shirtcliffe, S. J. Elliott and M. I. Newton, *Proc. IEEE Freq. Control Symp.*, 2008, 698–704.
57 Z. G. Sauerbrey, *Physics*, 1959, **155**, 206–222.
58 K. D. Esmeryan, G. McHale, C. L. Trabi, N. R. Geraldi and M. I. Newton, *J. Phys. D: Appl. Phys.*, 2013, **46**, 345307.
59 L. R. Pardo, J. F. Rodriguez, C. Gabrielli, H. Perrot and R. Brendel, *IEEE Sens. J.*, 2005, **5**, 1251–1257.